Atomic-level characterization of nano- and micro-structured porous materials by NMR : pushing the frontiers of sensitivity

Tuan Nghia Duong

UNIVERSITÉ GRENOBLE ALPES

THÈSE

Pour obtenir le grade de

DOCTEUR DE L'UNIVERSITÉ GRENOBLE ALPES

Spécialité : **Chimie Physique Moléculaire et Structurale**

Arrêté ministériel : 7 août 2006

Présentée par

Nghia Tuan DUONG

Thèse dirigée par **Olivier LAFON** et **Daniel LEE**
et **Gaël DE PAËPE**

préparée au sein du **Laboratoire de Résonance Magnétique**
dans **l'École Doctorale Chimie & Sciences du Vivant**

Dévelopment de la polarisation dynamique nucléaire à haut champ magnétique pour le caracterisation des matériaux nanostructurés

Thèse soutenue publiquement le **25 novembre 2015**
devant le jury composé de :

Pr Christian BONHOMME
Professeur, LCMCP, UPMC-Paris 6, Président
Dr Thibault CHAPENTIER
Ingénieur de Recherche, IRAMIS/NIMBE at CEA Saclay, Rapporteur
Dr Franck FAYON
Directeur de Recherche, CEMHTI-CNRS UPR 3079, Rapporteur
Dr Michel BARDET
Ingénieur de Recherche, INAC/SCIB at CEA Grenoble, Membre
Pr Olivier LAFON
Professeur, UCCS, Université Lille 1, Membre
Dr Daniel LEE
Ingénieur de Recherche, INAC/SCIB at CEA Grenoble, Membre
Dr Gaël DE PAËPE
Ingénieur de Recherche, INAC/SCIB at CEA Grenoble, Membre
Dr Hervé VEZIN
Directeur de Recherche, LASIR, Université Lille 1, Membre

ACKNOWLEDGEMENTS

Three years have been passed since I decided to pursuit my PhD at CEA Grenoble and CNRS Lille. During this tranquil and memorial period, I received lots of mentorship and assistance from my advisors, from colleagues, and my friends.

Firstly, I would like to express my sincere gratitude to my advisors, Dr. Daniel LEE, Dr. Gaël DE PAËPE, Dr. Michel BARDET, Prof. Olivier LAFON, and Dr. Hervé VEZIN, who have been going along with me during my PhD thesis. Their immense knowledge, valuable advices as well as great patience have helped me all the time in doing research and writing this thesis.

I also would like to thank Dr. Thibault CHARPENTIER, Dr. Franck FAYON, and Prof. Christian BONHOMME for accepting to become my jury members. It is obvious that their insightful comments would improve my manuscript quite a lot and aid me to widen not only my knowledge but also my research views from numerous perspectives.

My thanks go to TGIR-RMN organization, which provided me opportunities to work at the high-field (18.8 T) systems in Lille and Lyon. I thank all the members at this organization for their supports, especially Dr. Julien Trébosc for his guidance in programming pulse sequences and manipulating experiments. I had nice time studying from him during a month staying in Lille in 2013.

I thank all the members of the Laboratoire de Résonance Magnétique and the secretaries of the Service de Chimie Inorganique et Biologique for offering me such warm and nice environments.

My PhD duration could not be such interesting time without my colleagues and lab mates, who have been sharing my happiness as well as sadness. I not only learn much from fruitful discussions with them but also achieve much experience and advice, both in research and in life. Special thanks to Dr. Sabine HEDIGER, Dr. Ildefonso MARIN MONTESINOS, Dr.

Hiroki TAKAHASHI, Dr. Carlos FERNANDEZ DE ALBA, Dr. Frédéric MENTINK-VIGIER, Dr. Subhradip PAUL and Katharina MÄRKER. I had joy and lots of fun with them.

I would like to be grateful to all my Vietnamese friends in Grenoble, in Valence, and in Lille; we had great time together. Being far away from family, I consider my Vietnamese friends as my small family. *Cảm ơn cả nhà*!

Finally, I would like to thank my parents for their unconditional love and encouragement.

Atomic-level Characterization of Nano- and Micro-Structured Porous Materials by NMR: Pushing the Frontiers of Sensitivity

ABSTRACT

Solid-state NMR spectroscopy is a powerful analytical technique to characterize the atomic-level structure and dynamics of both ordered and disordered materials. However, its main limitation is the lack of sensitivity, particularly preventing studies on the surface of materials, an important region determining their chemical properties. It has been recently shown that Magic Angle Spinning Dynamic Nuclear Polarization (MAS-DNP) could overcome this difficulty. This technique can provide an enhancement of NMR sensitivity of many orders of magnitude. It is based on the partial microwave-driven transfer of the large intrinsic polarization of electron spins to nuclear spins, making impractical NMR experiments feasible. The aim of this work is to use this MAS-DNP technique to help gain new insights into the structure of certain materials. Such knowledge will facilitate the rational improvement of their properties. Two classes of materials are investigated. The first ones are siloxane-functionalized silica nanoparticles (NPs), which can be used to extend the working durability of fuel cells. Owing to the sensitivity enhancement achieved by MAS-DNP, the condensation network structure of siloxanes bound to the surface of silica NPs could be elucidated using ^{29}Si-^{29}Si homonuclear correlation NMR experiments. The second class of investigated systems encompasses two forms of aluminas, γ-alumina and mesoporous alumina. The former is widely used in industry as a catalyst, catalyst support, and adsorbent, whereas the latter is a promising material owing to its highly controlled porosity and its high surface accessibility. Nevertheless, their structures are still under heavy investigation since they do not form single crystals. Due to an improved comprehension of MAS-DNP performance, including optimized sample preparation, the obstacle of extremely low efficiency for surface-selective ^{27}Al NMR experiments is circumvented. Sophisticated two-dimensional NMR experiments are employed to provide selective insights into structures on the surface and a new experiment is proposed to study only the bulk of these materials. For achieving further information on the spatial proximities between different ^{27}Al sites, a thorough understanding of homonuclear dipolar recoupling pulse sequences for half-integer quadrupolar nuclei is required. In order to do this, Average Hamiltonian theory and numerical simulations are used to analyze the spin dynamics resulting from these pulse sequences, giving insights into their relative performances. Overall, it is shown that the use of MAS-DNP can be crucial for the characterization of state-of-the-art materials, highlighting the future importance of this technique.

Dévelopment de la polarisation dynamique nucléaire à haut champ magnétique pour le caracterisation des matériaux nanostructurés

RESUME

La spectroscopie de RMN des solides est une méthode de choix pour la caractérisation de la structure et de la dynamique à l'échelle atomique des matériaux ordonnés et désordonnés. Cependant, l'utilisation de cette technique est limitée par son manque de sensibilité qui empêche l'observation de la surface des matériaux, souvent responsable de leurs propriétés chimiques. Il a été récemment montré que la Polarisation Nucléaire Dynamique (DNP) dans les conditions de rotation à l'angle magique (MAS) permet de surmonter cette limitation. Cette technique permet d'augmenter la sensibilité de la RMN jusqu'à trois ordres de grandeur. Elle consiste à transférer la polarisation élevée des électrons non-appariés vers les noyaux grâce une irradiation micro-onde. L'objectif de cette thèse consiste à appliquer la MAS-DNP pour sonder la structure de matériaux nanostructurés inorganiques et hybrides. Ces nouvelles informations faciliteront l'amélioration raisonnée de leurs propriétés. Deux classes de matériaux ont été étudiées : des nanoparticules (NP) de silice fonctionnalisées avec des chaînes siloxane et deux formes d'alumine. Les NP de silice fonctionnalisées permettent d'accroître la durée de vie des piles à combustible. Grâce au gain en sensibilité offert par la DNP, il a été possible de sonder les connectivités et les proximités ^{29}Si-^{29}Si dans ces matériaux et ainsi d'élucider le mode de condensation des chaînes siloxane à la surface des NP de silice. La seconde classe de matériaux étudiés comprend deux formes d'alumine : l'alumine-γ et l'alumine mésoporeuse. La première est largement utilisée dans l'industrie comme catalyseur, support de catalyseur et adsorbant, tandis que la seconde est un matériau prometteur du fait de sa porosité contrôlée et de son accessibilité élevée. Néanmoins, la structure de ces alumines est toujours largement débattue car elles ne forment pas des monocristaux. Grâce à une meilleure compréhension des performances de la MAS-DNP, conduisant notamment à une optimisation de la préparation des échantillons, il a été possible de compenser la très faible efficacité des expériences ^{27}Al sélectives de la surface. La structure de la surface d'alumine a été sondée par des expériences RMN avancées à deux dimensions et une nouvelle expérience a été proposée pour l'observation sélective du cœur de l'alumine. Afin d'obtenir davantage d'informations sur les proximités ^{27}Al-^{27}Al, nous avons cherché à mieux comprendre les séquences de recouplage dipolaire homonucléaire pour des noyaux ^{27}Al. Pour ce faire, la dynamique de spin au cours de ces séquences a été analysée par la théorie de l'hamiltonien moyen et des simulations numériques. En résumé, au cours de cette thèse, nous avons montré comment la MAS-DNP ouvre de nouvelles perspectives pour l'étude des matériaux nanostructurés.

TABLE OF CONTENTS

Chapter I INTRODUCTION TO MAS-DNP

I.1. Solid-state Nuclear Magnetic Resonance: limitations and solutions

Solid-state (ss) Nuclear Magnetic Resonance (NMR) is widely used for the characterization of bio-molecules[1–5] and materials[6–10]. This technique provides deep insights into the local atomic-level structures, for example internuclear distances and spatial and angular constraints. More importantly, no long-range order is required and hence ssNMR is qualified for disordered, heterogeneous or amorphous materials that are difficult to characterize by diffraction techniques. Despite unique information gained, the disadvantage of NMR is the limited sensitivity. When NMR active nuclei (with spin $I \neq 0$) are subject to an external magnetic field, the small magnetic moment of these nuclei results in a small polarization between the energy levels. For spin $I = ½$, the polarization, P, between two spin states, α and β, is given by:

$$P = \frac{n_\alpha - n_\beta}{n_\alpha + n_\beta} = \tanh\left(\frac{\Delta E}{2k_B T}\right) = \tanh\left(\frac{\gamma \hbar B_0}{2k_B T}\right) \approx \frac{\gamma \hbar B_0}{2k_B T}, \quad \text{(I.1)}$$

where n_α and n_β correspond to the populations of the spin states α and β, respectively; ΔE is the energy difference between the two Zeeman energy levels; k_B is the Boltzmann distribution constant; and T is the absolute temperature; γ is the gyromagnetic ratio of the nucleus; $\hbar$ is the reduced Planck constant; B_0 is the external magnetic field. The simplification in Eq. I.1 is valid when $\Delta E/(k_B T) \ll 1$, i.e. T needs to be higher than 2 K for protons at 9.4 T. The Eq. I.1 can be generalized for any spin value[11].

A host of methods have been introduced to improve the NMR signal-to-noise (S/N) ratio, such as Magic Angle Spinning (MAS)[12] , whereby the sample is spun about an axis inclined by 54.736° with respect to the B_0 field. MAS partially averages out the anisotropic interactions, i.e. chemical shift anisotropy, dipolar couplings, and first-order quadrupolar interaction, thus

reducing the associated spectral line broadening. The integrated intensity of a NMR signal being identical with and without MAS means that MAS therefore can improve also the *S*/*N* ratio. The sensitivity of ssNMR can also be enhanced by Cross Polarization[13] (CP), which transfers the magnetization of highly abundant, high-γ nuclei, such as ^{1}H or ^{19}F, usually exhibiting short spin-lattice relaxation time constants (T_{1n}) to nuclei with lower γ, lower abundance or longer T_{1n} relaxation times, such as ^{13}C, ^{15}N, ^{29}Si or ^{31}P. Another method, which can improve the sensitivity, is the dipolar decoupling through radio frequency (rf) irradiation technique[14]. These rf pulse techniques average out heteronuclear and/or homonuclear dipolar interactions, and hence improve the spectral resolution and the sensitivity.

Besides the method developments, ssNMR also benefited from further advances in instrumentation. According to Eq. I.1, higher B_0 enhances the polarization. Therefore, high-homogeneity (giving high-resolution) NMR magnets have currently been built with B_0 magnitudes up to 23 T; yet higher fields are still demanded. Such high magnetic field improves the sensitivity provided the longitudinal relaxation times do not lengthen significantly at high field. Faster spinning frequency is another improvement (up to 110 kHz is now possible[15]) since it enables the better suppression of anisotropic interactions, which substantially enhances both the sensitivity and resolution of ssNMR. Fast spinning is notably required for nuclei subject to large anisotropic interactions, such as ^{1}H-^{1}H dipolar interactions or hyperfine couplings in paramagnetic solids.

Despite such remarkable progress, the application of ssNMR to numerous materials can still be extremely challenging for nuclei with low natural abundance and/or low γ ratio, such as ^{13}C, ^{15}N, and ^{29}Si.

Promising routes to overcome the intrinsic low sensitivity of NMR are the different hyperpolarization techniques, including the different methods of Dynamic Nuclear Polarization (DNP)[16], Chemical Induced Dynamic Nuclear Polarization (CIDNP)[17,18], Para-hydrogen induced polarization (PHIP)[19,20], and hyperpolarized ^{129}Xe NMR[21]. Among them, MAS-DNP is one of the most useful methods owing to wide applications ranging from biomolecules to nanomaterials coupled with the significant enhancement of sensitivity (up to three orders of magnitude). During my PhD, MAS-DNP has been used for the study of materials that are hard/impossible to fully investigate by the other spectroscopic techniques.

I.2. Brief history of Dynamic Nuclear Polarization

The original idea of DNP was predicted by Overhauser for metals in 1953. He proposed that the saturation of electron transitions could enhance the polarization of nuclei[22]. In the same year, this prediction was experimentally verified by Carver and Slichter[16]. Experimental results showed that the saturation of electron transitions provided 100-fold enhancement of a ^{7}Li signal. This phenomenon was named as the Overhauser effect. The details of these experiments are given in the caption of Figure I.1.

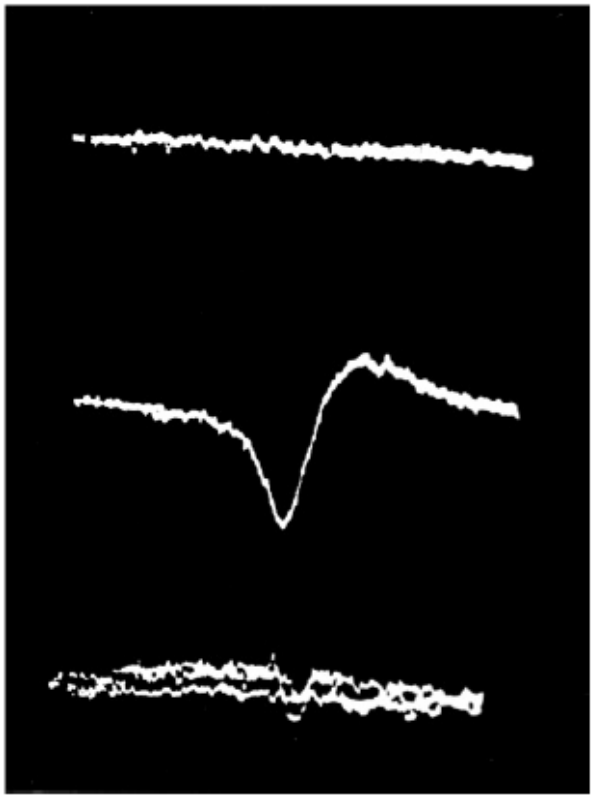

Figure I.1. The first demonstration of the Overhauser effect in metals. Experiments were performed under static conditions on lithium metal subject to an external magnetic field of 0.003 T. The top line is the NMR signal without microwave (μw) irradiation. The ^{7}Li resonance was masked by the electronic noise. The middle line is the ^{7}Li resonance, which was enhanced by the application of suitable microwave irradiation producing the Overhauser DNP effect. The bottom line is the ^{1}H resonance of a glycerin sample for comparison. Adapted from Ref. 16.

The Overhauser effect was not only proved for metals but also for liquids containing unpaired electrons by the work of Carver and Slichter on ^{23}Na metal dissolved in liquid ammonia (NH_3)[23].

Further development in the field was the introduction of the solid effect by Jeffries and coworkers[24,25]. They reported DNP-NMR experiments on solid dielectrics at low field (0.33 T).

The first MAS integration with DNP experiments were performed for the study of coal, polymers, and diamonds[26,27] by Wind, and Schaefer in the 1980s. The external magnetic field at that time was up to 1.5 T.

The main difficulty for high-field DNP was the lack of high frequency and high power electromagnetic irradiation for the saturation of electron transitions at high magnetic field. Recently, this issue has been solved by R. G. Griffin and R. J. Temkin at MIT[28,29]. They proposed the use of a gyrotron as the μw source for DNP-NMR at high magnetic field. Using such a device, substantial sensitivity enhancement has been achieved for biomolecules at high magnetic field[30–33].

I.3. DNP polarization transfer mechanism

It is known that the enhancement of sensitivity obtained from DNP was based on the transfer of polarization from unpaired electrons to neighboring nuclei. The DNP transfer in dielectric solids at 100 K can be described by three mechanisms: the Overhauser Effect (OE)[34], the Solid Effect (SE)[35], and the Cross Effect (CE)[35].

I.3.1. Overhauser Effect

The OE mechanism firstly was believed to exist only in conducting solids and liquids, but a recent article[34] showed that it can also be observed for non-conducting solids.

This effect was discussed in a system consisting of one nucleus (*I*) and one electron (*S*). Since both electrons and nuclei have spin number equal to ½, the proposed system is described by four energy levels (*see* Figure I.2).

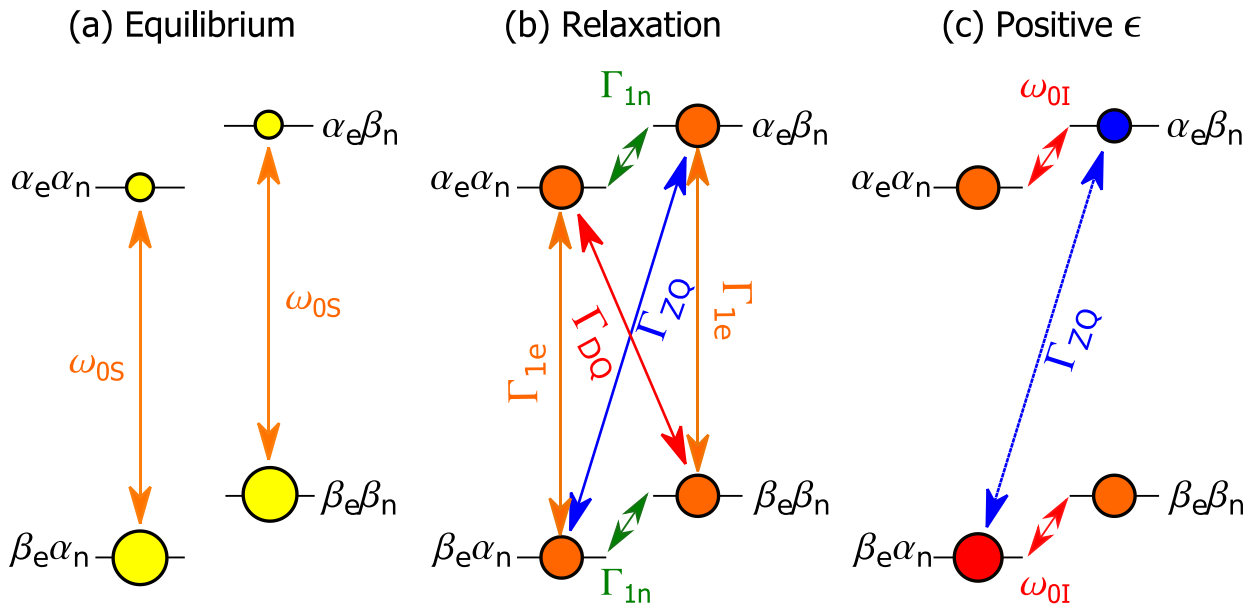

Figure I.2. Principle of the OE. The figure shows energy level diagrams of a system consisting of one electron and one proton in different cases: (a) the Boltzmann distribution of populations at thermal equilibrium, (b) the saturation of electron transitions after the application of μw irradiation at the Electron Paramagnetic Resonance (EPR) frequency (the possible relaxation pathways among spin states are shown as arrows); and (c) a situation where the zero quantum relaxation dominates leading to the re-distribution of populations between different energy levels, resulting in the positive enhancement.

The OE is a relaxation-based mechanism. Depending on the dominant relaxation pathway, (positive or negative) enhancement of NMR signals will be observed. In dielectric solids, positive OE was observed for polystyrene doped with 1,3-bisdiphenylene-2-phenylallyl (BDPA) and negative OE for perdeuterated BDPA (d_{21}-BDPA). This result indicates that, for such a sample, the cross-relaxation involved in the OE stems from the modulation of hyperfine interactions by the intra-molecular delocalization of the unpaired electrons in BDPA.

The OE involves the saturation of allowed electron single quantum (SQ) transitions, hence the power of μw irradiation required is low. Moreover, the OE enhancement is proportional to the magnetic field, which was ascribed to the faster cross-relaxation at higher field[34].

I.3.2. Solid Effect

The static case

In the secular approximation, the Hamiltonian of a system containing one unpaired electron and one nucleus is:

$$H_{SE} = \omega_{0S} S_z - \omega_{0I} I_z + A S_z I_z + B S_z I_x \,, \qquad \text{(I.2)}$$

where S and I denote the spin of the electron and the nucleus, respectively, ω_{0S} is the Larmor frequency of electron S, and ω_{0I} is the Larmor frequency of nucleus I. A is the coefficient of secular hyperfine coupling while B is the coefficient of the non-secular hyperfine interaction. The difference in sign of the Zeeman terms of nucleus I and electron S stems from the difference in sign of the γ ratio. The four-energy levels of such a system at thermal equilibrium and the four generated mixing states under double quantum (DQ) irradiation or zero quantum (ZQ) irradiation are shown in Figure I.3.

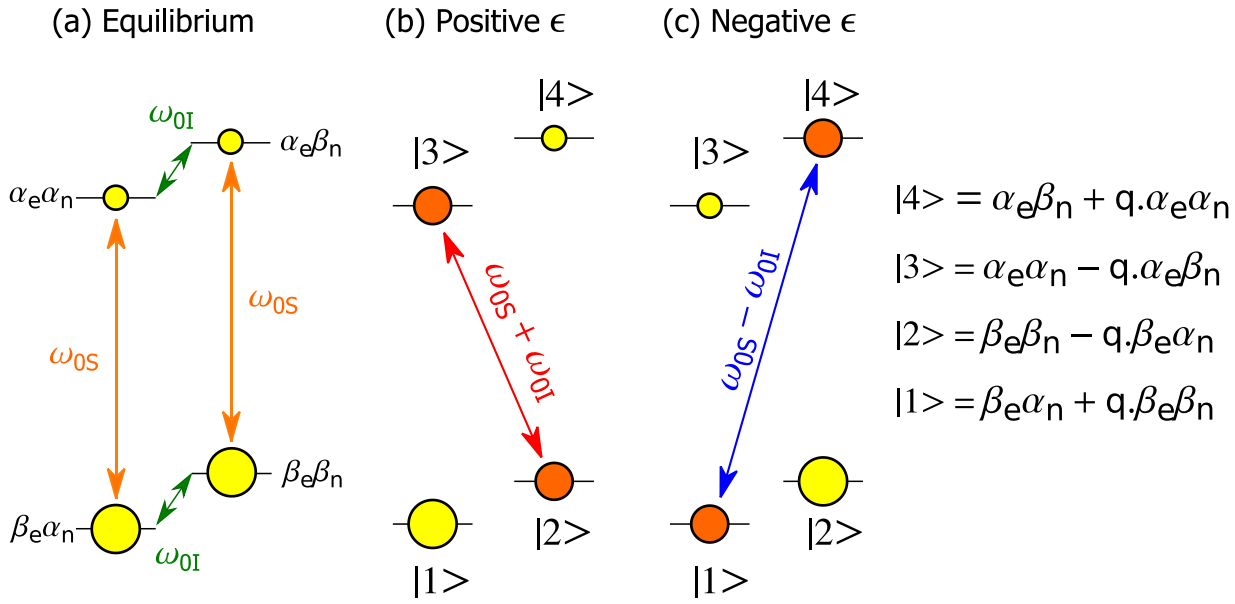

Figure I.3. Principle of the SE for a static sample. The figure shows the energy level diagram of a $\{e, n\}$ spin system. At thermal equilibrium, the populations at different energy levels follow the Boltzmann distribution (a). The subfigures show the population distribution after μw irradiation of the DQ (b) and ZQ transitions (c). These irradiations produce either positive or negative enhancements, respectively.

In contrast with the OE mechanism, if the μw irradiation excites the SQ transitions of the unpaired electrons, it does not enhance the nuclear polarization.

Nevertheless, the non-secular hyperfine interaction (S_zI_x term in Eq. I.2) allows the mixing of the states of the system, leading to the generation of new eigenstates, which are shown in Figure I.3 and hence the saturation of forbidden transitions, namely DQ or ZQ transitions are possible. Such saturation results in positive or negative enhancement. However, saturation of the forbidden transitions requires much larger μw power than that of the allowed transitions in the OE. Another practical difficulty of the SE is that the mixing coefficient ($q \approx \frac{B}{2\omega_{0I}}$) is small and inversely proportional to ω_{0I}. Thus the probability of either DQ or ZQ transitions is proportional

to ω_{0I}^{-2}. This means that SE efficiency scales inversely proportional to the square of the magnetic field, hence the SE mechanism is not efficient at high field.

It is worth mentioning that the EPR breadth Δ (inhomogeneous broadening due to the anisotropic *g*-tensor interaction) is required to be smaller than the Larmor frequency of nucleus, ω_{0I} otherwise the positive DNP enhancement would be overlapped with the negative, leading to the reduction of overall enhancement.

The application of MAS

The spin dynamics of this system changes between a static and MAS sample[36]. For the static case, the electron and nuclear resonance frequencies depend on the crystallite orientations owing to the anisotropic interactions, hence only a limited number of electron-nucleus pairs experience the DQ or ZQ transitions induced by the specific required frequency of the μw irradiation, while the others do not because the frequency matching condition is not met. With the application of spinning, the anisotropic interactions become time-dependent and the energy levels change during one rotational period. This means that every electron-nucleus pair will experience the SE mechanism, for a short duration of time. These cumulative periodic effects will contribute to the final SE-DNP enhancement.

I.3.3. Cross Effect

The static case

A simple system consisting of two coupled unpaired electrons and a single nucleus $\{e_a\text{-}e_b\text{-}n\}$ is used to describe the CE mechanism. The Hamiltonian, in the secular approximation, is expressed in Eq. I.3.

$$H_{CE} = \omega_{0Sa}S_{az} + \omega_{0Sb}S_{bz} - \omega_{0I}I_z + D_{ab}.\left(2S_{az}S_{bz} - S_{ax}S_{bx} - S_{ay}S_{by}\right) + (A_aS_{az} + A_bS_{bz})I_z + (B_aS_{az} + B_bS_{bz})I_x \,, \quad \text{(I.3)}$$

where ω_{0S_i} (i = a or b) and ω_{0I} denotes the Larmor frequencies of the unpaired electron i and the nucleus, respectively. D_{ab} is the dipolar coupling constant between electron a and b, A_i (i = a or b) are the coefficients for the secular hyperfine interactions of electron i with the nucleus, and B_i (i = a or b) are the coefficients for the non-secular parts of hyperfine interactions.

If the CE condition $|\omega_{0Sa} - \omega_{0Sb}| = \omega_{0I}$ is fulfilled, i.e. the energy levels $|\alpha_a\beta_b\alpha_n\rangle \leftrightarrow |\beta_a\alpha_b\beta_n\rangle$ and/or $|\beta_a\alpha_b\alpha_n\rangle \leftrightarrow |\alpha_a\beta_b\beta_n\rangle$ are degenerate, the μw irradiation at the resonance frequency of one electron would flip the polarization of that electron and create the polarization difference between the two electrons. Due to degeneracy, the three spins flip spontaneously, yielding an enhancement of nuclear polarization.

To satisfy the CE conditions, it is required that the Larmor frequency of the nucleus is smaller than the inhomogeneous breadth of the EPR linewidth ($\omega_{0I} < \Delta$) so that the sample contains pairs of unpaired electrons with a difference in EPR frequencies equal to ω_{0I}. Meanwhile, the homogeneous EPR linewidth (owing to the dipolar interaction between unpaired electrons) is required to be smaller than the Larmor frequency of the nucleus, i.e. $\delta < \omega_{0I}$.

Unlike the SE, the CE involves the excitation of allowed transitions between electron energy levels, hence much less power of μw irradiation is required. The anisotropic g-tensor interaction scales with the magnetic field. Hence, the CE matching condition is less probable at higher field and the CE efficiency is inversely proportional to the magnetic field. At higher fields, the CE mechanism is therefore less detrimentally affected than SE mechanism.

The application of MAS

The spin dynamics of the CE are significantly changed under MAS. Owing to the periodical modulation of different energy levels as well as the anisotropic coefficients under MAS, a new

approach was proposed to describe the CE under MAS[36,37] During a rotational period, four phenomena of energy-(anti-)level crossings can occur:

1. The dipolar anti-level crossing
2. The CE condition
3. The SQ saturation of electron transitions
4. The SE condition

Figure I.4 shows how these four types of anti-level crossing affect the eight energy levels and their populations.

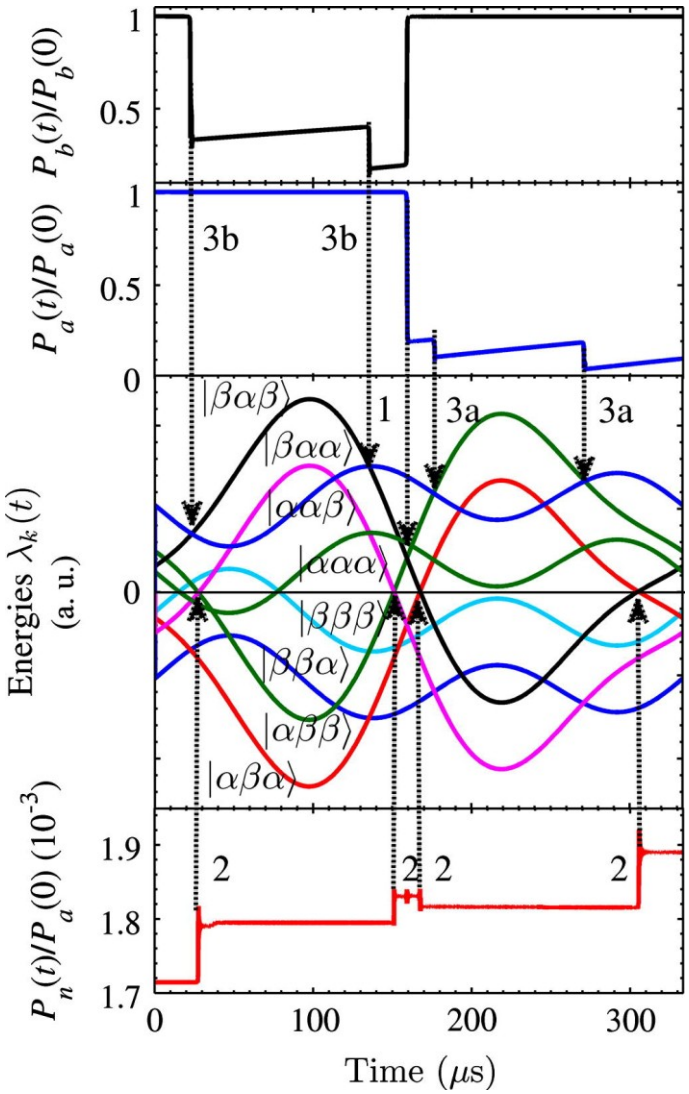

Figure I.4. Simulation of the evolutions of eight energy levels for a three-spin $\{e_b\text{-}e_a\text{-}n\}$ system with n being a proton in a single crystal (i.e. a single orientation with respect to the B_0 field). The evolution of the electron (P_a and P_b) and nuclear (P_n) polarizations are also displayed. The energy levels are labeled as $|e_a e_b n\rangle$. The notation of 1, 2, and 3a or 3b present the anti-level crossings phenomena described in the text. For sake of clarity, 3a and 3b means the single quantum excitation of electron a and b, respectively. The temperature was set at 100 K, the external magnetic field was equal to 9.4 T, the electron nutation frequency induced by the μw irradiation was 0.85 MHz, and the MAS frequency equal to 3 kHz. Adapted from Ref. 36.

In the MAS-CE mechanism, as shown in the Figure I.4, the different anti-level crossing phenomena are short events. The nuclear hyperpolarization is generated by short CE matching conditions following either μw irradiation at the resonance of one of the two electrons or the electron-electron dipolar exchange process. As at equilibrium the electron polarization is close to 1 (and the γ ratios of the electron and the proton have opposite signs), the spin states at the beginning of the rotor period are $|\beta_b\beta_a\alpha_n\rangle$ or $|\beta_b\beta_a\beta_n\rangle$. The first anti-level crossing in Figure I.4 is the degeneracy of $|\beta_b\beta_a\beta_n\rangle$ and $|\alpha_b\alpha_a\alpha_n\rangle$. Under on-resonance μw irradiation, the SQ transition of e_b electron occurs, i.e. $|\beta_b\beta_a\beta_n\rangle \rightarrow |\alpha_b\beta_a\beta_n\rangle$. The second anti-level crossing is a CE condition. Under this condition, the energy levels $|\alpha_b\beta_a\beta_n\rangle$ and $|\beta_b\alpha_a\alpha_n\rangle$ are degenerate and the transition $|\alpha_b\beta_a\beta_n\rangle \rightarrow |\beta_b\alpha_a\alpha_n\rangle$ occurs. Hence, the consecutive SQ transition of e_b electron and CE exchange deplete the β_n state to populate the α_n state. In other words, it increases the nuclear polarization. For this crystallite orientation, the same anti-level crossings occur during the first-half of the rotational period. In the middle of the rotational period, there is a dipolar anti-level crossing, which converts the $|\alpha_b\beta_a\beta_n\rangle$ state into $|\beta_b\alpha_a\beta_n\rangle$, i.e. exchanges the polarization of the unpaired electrons. Then, during the second half of the period, at the CE condition, the transition $|\beta_b\alpha_a\beta_n\rangle \rightarrow |\alpha_b\beta_a\alpha_n\rangle$ occurs, further increasing the nuclear polarization.

Figure I.4 was simulated for a single orientation. In a powder, the times at which the anti-level crossings occur, depend on the crystallite orientation. In fact, under MAS, all orientations of the polarizing agent, except for the special case in which the axis connecting the two electrons is parallel to the MAS axis, have probability of experiencing the CE mechanism, which is not always true for the static case. This cumulative periodic effect of generated nuclear hyperpolarization would contribute to the final large enhancement.

I.4. Polarizing agents and frozen glass-forming solvents

The choices of polarizing agents (sources of unpaired electrons) and their concentrations decide the dominant polarization transfer mechanism. As mentioned above, the SE enhancement strongly decreases at the higher magnetic field; hence this mechanism is not favorable for the current high-field DNP applications. The OE apparently scales favorably with the magnetic field [34], however at the moment it was only observed for BDPA, thus further study is required. Larger DNP enhancements at high field have been measured for the CE. In this work, we focus on nitroxide-based bi-radicals, where the CE mechanism is the dominant.

The BTnE series were the first biradicals introduced as DNP polarizing agents[38]. It was found out that with n equal to 2, for which the dipolar e-e coupling equals 22 MHz, corresponding to an e-e distance of ~12.8 Å[39], BT2E provides the maximal enhancement. However, this radical does not well dissolve in aqueous media, such as a mixture of glycerol and water. The reason why aqueous media is important since the early studies of DNP samples of interest were biomolecules, which are water-soluble materials. This led to the design of a new polarizing agent, 1-(TEMPO-4-oxy)-3-(TEMPO-4-amino) propan-2-ol, named TOTAPOL[39]; which provides large enhancement and is soluble in aqueous environment. Figure I.5 displays the build-up of NMR signal after nuclear saturation (using the experiment depicted in Figure I.5c) and the associated proton enhancement obtained on 2M ^{13}C-urea using TOTAPOL[35].

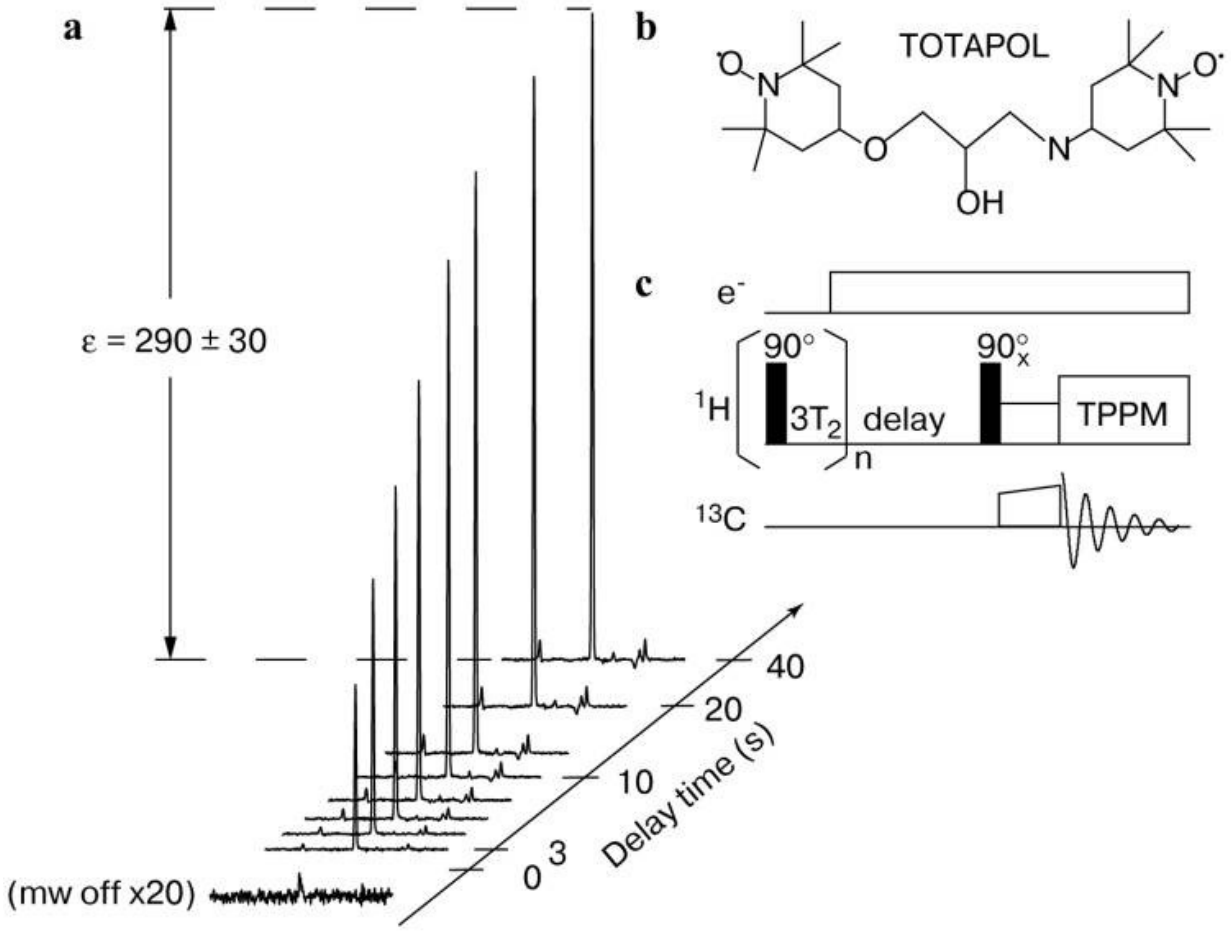

Figure I.5. (a) The build-up of the $^{1}H \rightarrow ^{13}C$ CPMAS signal of 2M ^{13}C-urea with 3 mM TOTAPOL in a frozen solution of $[^{2}H]_6$-DMSO/$^{2}H_2O$/H_2O (60/34/6 wt%) mixture as function of the μw irradiation time. (b) The structure of TOTAPOL, and (c) the $^{1}H \rightarrow ^{13}C$ CPMAS saturation-recovery pulse sequence. The experimental conditions are B_0 = 5 T, at a temperature of 90 K, and a MAS frequency of 7 kHz. Adapted from Ref. 35.

The solvent plays an important role in DNP experiments since it should ensure the uniform distribution of biradicals within/around the sample of interest and can act as a cryoprotectant. Without meeting these requirements, considerably smaller DNP enhancements were observed for biological samples[35]. For large and uniform signal enhancement, partial deuteration of mixture of glycerol and water solvents can be beneficial[40].

Despite efficient polarization transfer observed for TOTAPOL, higher enhancement could be obtained by designing the radicals to have a rigid structure, leading to longer electron relaxation times. The newly designed polarizing agent bis-TEMPO-bis-Ketal (bTbK), when dissolved in a mixture of perdeuterated dimethyl sulfoxide ([$^2H_6$]-DMSO), deuterated water (^2H_2O), and pure water (H_2O) (77/16/7 wt%, respectively) led to better enhancement compared to TOTAPOL under similar experimental conditions when determining the enhancement obtained from $^1H \rightarrow ^{13}C$ CP-MAS experiments performed on ^{13}C-urea[41]. One limitation of bTbK is that it is sparsely soluble in water; however a sensitivity enhancement of 18 was observed for an oriented membrane polypeptide system where bTbK was used as a polarizing agent[42].

Substantial improvement in the field of biradical design was achieved with the introduction of AMUPol[43]. This polarizing agent demonstrates much superior enhancement compared to TOTAPOL, namely 3.5 times and 4 times under identical experimental conditions at 9.4 T and 11.7 T, respectively[43], and it is highly soluble in aqueous solutions. Such interesting results root from the larger dipolar e-e coupling, namely >30 MHz[43] compared to ~20 MHz of TOTAPOL[39] and the longer electron relaxation times[44].

I.5. Sample preparation

In order to achieve maximal enhancement, sample preparation is one of the most important steps. The polarizing agents and the choices of solvents were discussed in Section I.4. In this part, three ways for efficient sample preparations are described.

I.5.1. Frozen solution

MAS-DNP experiments normally utilize frozen solutions doped with polarizing agents[30]. The aim of performing experiments at low temperature is to lengthen the nuclei relaxation times,

allowing efficient polarization transfer from electrons to neighboring nuclei. This approach has shown significant enhancement in sensitivity for various samples[31,32,45–47].

I.5.2. Incipient wetness impregnation

This approach has been widely used for the characterization of porous materials[48–50]. A polarizing agent is dissolved in a suitable DNP matrix (aqueous or organic solvents) and the porous material is impregnated with this solution, which fills the volume of the pores. Compared to conventional NMR experiments, the sample may be altered by the incorporation of radicals and also the frozen solvent within the pores.

I.5.3. Matrix free

This approach was successfully applied to various samples, from microcrystalline cellulose[51] to proteins[52]. It bases on direct or indirect binding affinity interactions between polarizing agents and the sample to keep a uniform distribution of the polarizing agents upon the removal of the solvent. Owing to the maximized effective analyte, a significant increase in signal-to-noise ratio is achieved.

I.6. MAS DNP-NMR instrumentation

The general scheme of the MAS-DNP system is shown in Figure I.6. The main components are numbered and referred in the caption of the figure.

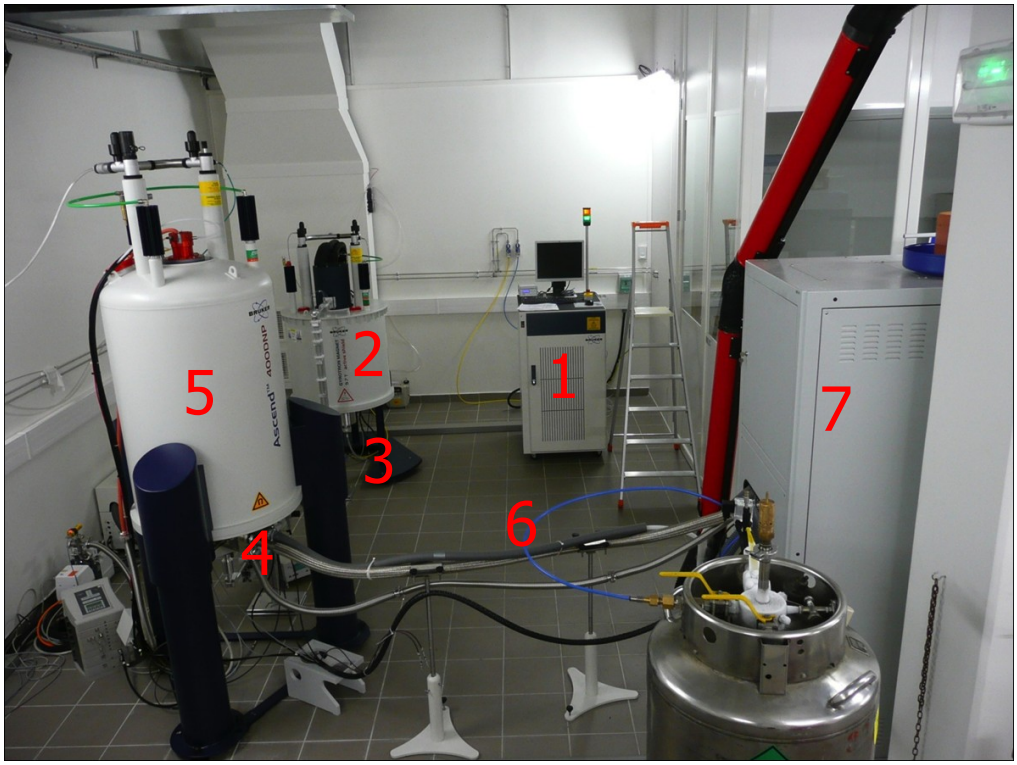

Figure I.6. A picture of the MAS DNP-NMR system in Grenoble. The components include: (1) the control system that monitors the gyrotron (2) where the μw irradiation is generated. This μw irradiation is then transferred through the transmission line (3) to the MAS DNP-NMR probe (4). This cryoprobe is mounted in the NMR magnet (5). The sample is contained in the probe and spun by a cold nitrogen gas flow (6) produced by the cooling cabinet (7).

As presented in Figure I.6, besides the NMR magnet (4), the MAS-DNP system requires several additional components. More details about the gyrotron, the wave-guide (transmission line), and the cryoprobe are given below.

Gyrotron

In the gyrotron, electron beams, emitted by an electron gun, are accelerated by an electric field and travel through a transverse magnetic field. This magnetic field induces a helical motion of these electrons at a specific frequency determined by the magnetic field. Then these electrons go

towards a resonant cavity, where the kinetic energies are converted to μw power. The μw irradiation leaves the gyrotron through a window while the electron beams hit a cooled collector.

Wave-guide

The μw irradiation is coupled to the wave-guide, whose aim is to transmit the irradiation to the probe with optimal delivery. Currently, owing to combination of low cost and efficiency in reducing power losses, rectangular- or circular-tube corrugated waveguides are used[40].

Cryoprobe

DNP experiments are preferably performed at low temperature since (i) the electron relaxation times are longer, which facilitates the saturation of the EPR transitions, (ii) the T_{1n} of ^{1}H nuclei are longer, which allows more electron-proton polarization transfer to occur and improves the efficiency of ^{1}H-^{1}H spin diffusion[35]. All these factors lead to larger enhancement. Hence, the MAS-DNP-NMR probe should be compatible with low temperature. One of the difficulties in designing such a probe is to keep it thermally isolated so that low temperature could be obtained and this cryogenic conditions do not damage the surrounding hardware, for example the shim stack.

As mentioned earlier, the DNP experiments require the use of high power and high frequency μw irradiation, thus the probe should be designed so that this irradiation could penetrate well into the samples. It was shown that perpendicular penetration of μw irradiation with respect to the rotor axis delivers better efficiency than a design with parallel irradiation[53].

I.7. Some recent DNP applications

Owing to the tremendous progress in both the design of polarizing agents and instrumentation, DNP has become an efficient technique enabling NMR experiments, which are impracticable under conventional ssNMR. Despite numerous recent applications[54–56], only two will be

recounted briefly here: studying the structure of catalytic mesoporous alumina (m-Al_2O_3)[57] and showing that ^{13}C-^{13}C correlations could be obtained for a protein at natural isotopic abundance.

I.7.1. DNP-enhanced NMR of mesoporous alumina surface

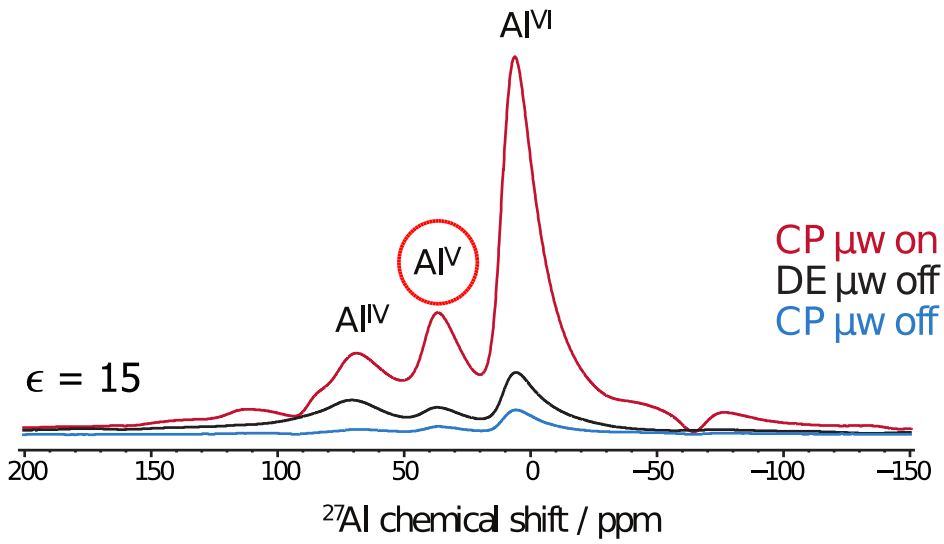

Figure I.7. One dimension (1D) ^{27}Al spectra of m-Al_2O_3 impregnated with 20 mM TOTAPOL in [^2H]$_6$-DMSO/^2H_2O/H_2O (78/14/8 wt%) mixture. The DNP-enhanced $^1H \rightarrow ^{27}Al$ CPMAS experiments were performed with μw (red line) and without μw (blue line) irradiation at a MAS frequency of 8 kHz and at a temperature of ~ 100 K and B_0 = 9.4 T. The black line presents the direct excitation ^{27}Al spectrum without μw irradiation under similar experimental conditions. Adapted from Ref. 50.

Lee et al.[50] have recently shown that the surface of m-Al_2O_3 impregnated with TOTAPOL solution can be selectively observed using $^1H \rightarrow ^{27}Al$ CPMAS experiments since ^1Hs are only located at the surface. Penta-coordinated (Al^V) sites were clearly observed, as shown in Figure I.7. A factor of 15 in sensitivity enhancement was achieved with DNP, leading to a substantial reduction in experimental acquisition time. This permitted a surface-selective 2D DQ-

SQ ^{27}Al-^{27}Al correlation experiment to be recorded within only 4 hours[50] using the $BR2_2^{1}$[58] recoupling sequence.

I.7.2 DNP-enhanced ^{13}C-^{13}C natural abundance correlations of proteins

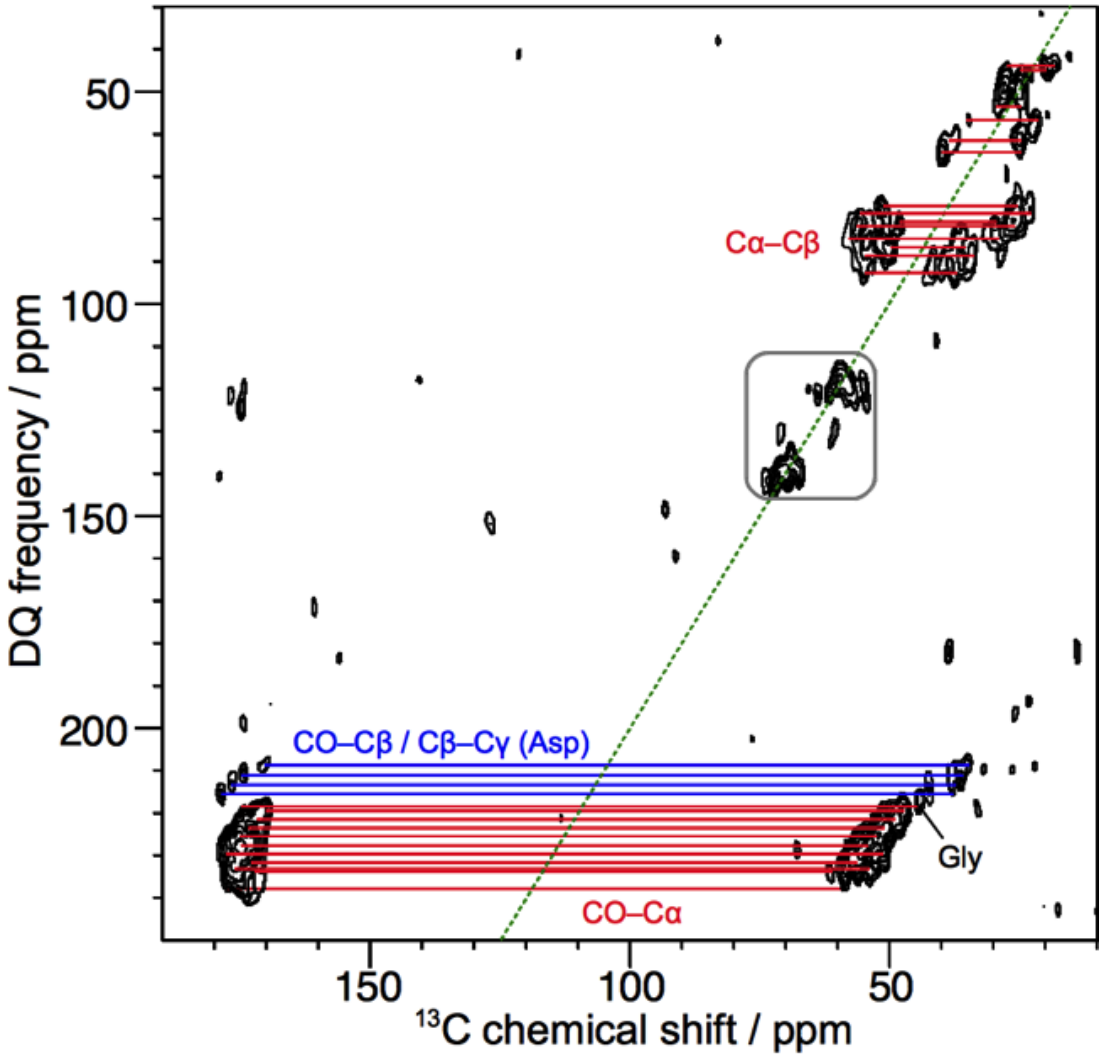

Figure I.8. A 2D DQ-SQ ^{13}C-^{13}C correlation spectrum of lysozyme at natural isotopic abundance was recorded at a MAS frequency of 10.5 kHz, sample temperature of ~ 100 K, and B_0 = 9.4 T. The homonuclear dipolar recoupling sequence used is SPC5[59] with a recoupling time of 1.52 ms. Adapted from Ref. 52.

Besides inorganic materials, DNP-NMR also opens new avenues for the study of biomolecules, by accelerating the acquisition of multi-dimensional NMR experiments. Takahashi et al. have notably shown using a matrix-free sample preparation that ^{13}C-^{13}C correlation 2D spectra at natural isotopic abundance can be recorded in 20 minutes instead of 4 days under conventional ssNMR with larger amount of sample[51]. Then, Takahashi et al. showed that this matrix-free sample preparation could be employed to study a much more complex system, namely the 14.3 kDa protein, lysozyme[52]. The 2D ^{13}C homonuclear correlation spectrum of this sample is reproduced in Figure I.8. These first examples highlight the potential power of MAS DNP-NMR.

I.8. Outline of PhD

Probing ^{29}Si – ^{29}Si connectivities and proximities using MAS-DNP

- Introduction
  - Silicon element and its chemical compounds
  - Limitation of ^{29}Si NMR spectroscopy and the solution
- Probing ^{29}Si - ^{29}Si connectivities and proximities
  - Through-bond correlation experiment
  - Through-space correlation experiment
- Numerical simulations on the transfer efficiency of through-space recoupling sequences
- Investigating the condensation networks of organosiloxanes on SiO_2 NPs

Probing quadrupolar nuclei using MAS-DNP

- Introduction
  - The importance of alumina
  - Quadrupolar nuclei and quadrupolar interactions
  - Effects of quadrupolar interactions on NMR spectra
  - The need of MAS-DNP
- Effects of sample preparations on NMR relaxation parameters
- The structure of the bulk and the surface of aluminas
  - *Primostrato* technique
  - *Bulk-filtered* technique
- Higher-resolution techniques
  - High-field DNP
  - *Primostrato* and *bulk-filtered* z-filtered 3QMAS
  - Recoupling sequence $BR2_2^1$

$BR2_2^1$ recoupling sequence

- A spin dynamics analysis of $BR2_2^1$ by the Average Hamiltonian theory
- Verification of the derived terms by simulations
- Experiments

Conclusion and Perspectives

Chapter II CONDENSATION NETWORK OF ORGANOSILOXANES ON SILICA NANOPARTICLES ELUCIDATED BY DNP-ENHANCED SOLID-STATE NMR

II.1. Silicon element

Silicon (Si) is the 14th element of the periodic table. It is placed in the same group, IVA, with other elements such as carbon (C), germanium (Ge), tin (Sn) and lead (Pb). It is profuse, and thus cheap, and has numerous applications in industry, especially in the alloy industry[60] and electronic devices. Naturally, there are three stable isotopes of silicon, including ^{28}Si, ^{29}Si, and ^{30}Si. The most abundant is ^{28}Si (accounting for about 92%, *see* Table II.1); however this isotope is NMR silent owing to having a spin number I equal to zero. Among these isotopes, only ^{29}Si has a non-zero spin number (I = ½) and is therefore a NMR-active nucleus. The sensitivity of ^{29}Si NMR is low owing to the low natural abundance of this isotope, its moderate gyromagnetic ratio, $\gamma(^{29}\text{Si})/\gamma(^{1}\text{H}) = 0.2$, and its very long T_1 relaxation times.

Table II.1. Natural abundance and spin dynamics of stable isotopes of silicon.

Isotope	^{28}Si	^{29}Si	^{30}Si
Natural abundance	92.21%	4.70%	3.09%
Spin number	0	½	0

II.2. Silicon materials

Silicon-containing materials include silicone polymers and silicate materials, such as silica (SiO_2), silicate glasses, clays or zeolites. It is estimated that silicate minerals account for 60 % of the Earth's crust[61]. Synthetic silica-based materials, such as mesoporous silica and mesoporous silica nanoparticles[62], are promising systems for drug delivery, sensors, photonics, and catalysts[63]

A better understanding of the structure of these silica-based materials is required for a rational improvement of their properties. This is not a trivial task since silica encompasses a broad range of compounds, from pure crystalline (quartz) to amorphous (silica gel, fumed silica, and silica glass) materials. For crystalline materials with long-range order, diffraction techniques are a suitable structural characterization method but this is not the case for amorphous systems, which lack long-range order. ssNMR is especially qualified for the characterization of such systems since this technique enables the investigation of both crystalline and amorphous silica-based compounds, providing valuable information on their atomic-scale structures.

II.3. Notation and Chemical shift standard

For the sake of clarity in studying the structure of silica-based materials, the notations of M, D, T, and Q units were introduced. These units are depicted in Figure II.1.

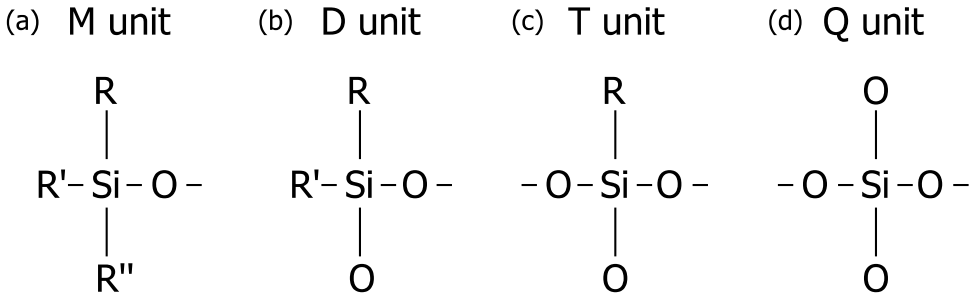

Figure II.1. Silica backbone nomenclature. (a) "M unit" where one oxygen attaches to the Si atom, (b) "D unit" where two oxygens atoms attach to the Si atom, (c) "T unit" where three oxygen atoms attach to the Si atom, and (d) "Q unit" where four oxygen atoms attach to the Si atom. R, R', and R'' are hydrocarbon linkers.

As shown in Figure II.1, depending on the number of O atoms attached to the Silicon, different building units are named[64]. To add greater detail, the X^n notation is used[65], where X

could be M; D, T, and Q building unit while the index n denotes the number of Si – O – Si connectivities.

Chemical shifts (δ) of nuclei are measured by comparison to a reference. For ^{29}Si NMR, the reference compound defined by IUPAC[66] is tetramethylsilane (TMS) with the chemical formula $(CH_3)_4Si$, whose $\delta(^{29}Si)$ is set to 0 ppm. In this work, we used $[O\mathbf{Si}O_{1.5}]_8[O\mathbf{Si}(CH_3)_3]_8$ (Q_8M_8) as a secondary reference. The ^{29}Si MAS ssNMR spectrum of this compound features six resonances; two peaks belong to the M group while the other four belong to the Q group. The chemical shift, $\delta(^{29}Si)$ of the most shielded resonance equals to -109.68 ppm relative to TMS.

II.4. Literature of ^{29}Si MAS-NMR on silica

Since the surface structures determine many chemical properties of silica compounds[61], a surface-selective technique is required. CP can be such a technique; however, the success of using this surface characterization bases on the assumption that all protons of samples reside on the surface, not in the bulk. A major limitation for the study of silica surfaces by $^1H\rightarrow^{29}Si$ CPMAS is the lack of sensitivity of conventional ssNMR.

In 1980, hydrated silica gel was studied by Maciel and co-workers[67]. In this work, the surface of these gels was studied by $^1H\rightarrow^{29}Si$ CPMAS[67] experiments and it was shown that the surfaces featured three Q unit sites: $(SiO)_2\mathbf{Si}(OH)_2$ (Q^2) units, corresponding to a peak at -89 ppm, $(SiO)_3\mathbf{Si}(OH)$ (Q^3) units at -99 ppm, and $(SiO)_4\mathbf{Si}$ (Q^4) units at -109 ppm[67]. In order to verify the assumption that the bulk is devoid of protons, hydrated silica gel was repeatedly subjected to proton exchange using ^2H_2O to remove the protons (^{1}Hs) and then $^1H\rightarrow^{29}Si$ CPMAS experiments were performed to probe whether the acquired spectra are different from that of the standard hydrated silica gel. Experiments on exchanged silica gel showed that for a room temperature exchange, the Q^2 sites are completely depleted; and at higher temperatures, Q^3 and

Q^4 sites were still visible but the intensities were considerably reduced[61]. It was estimated that approximately 91 to 97 % of silanol protons are exchangeable with ^2H_2O, the exact amount depends on the time and the temperature of the exchange[61].

The bulk of the material was investigated by direct excitation under MAS (DEMAS) ^{29}Si NMR; the spectrum of the bulk was dominated by Q^4 sites[67]. This result also indicates that for hydrated silica gels, the Si atoms located at the surface represent only a small fraction of all Si atoms.

The spin dynamics of different Q sites under CP experiments were also studied by plotting the CP efficiency versus the "contact time" of the dual CP pulses. From these curves, a mathematical analysis was used to derive a CP transfer rate, characterized by the rate constant T_{HSi}^{-1}; and the spin-lattice relaxation time in the rotating frame, characterized by $T_{1\rho}$[67]. It was found that T_{HSi}^{-1} of the -89 ppm peak is approximately twice in magnitude compared to that of the -99 ppm, which is then an order of magnitude larger than T_{HSi}^{-1} of the -109 ppm peak. Based on the proximities and number of protons, the assignment Q^2, Q^3, and Q^4 was consistent with the T_{HSi} rates[61].

Besides silica gel, these experimental approach protocols were also successfully applied to various silica-based systems, such as quartz crystal, fumed silica, silica glass[68], and derivatized silica[69] .

II.5. Limitation of ^{29}Si NMR and the solution

Although ssNMR has been extensively used for the characterization of silicate compounds[70–73], a major limitation for the use of this technique is its lack of sensitivity (*see* Section II.1). ^{29}Si NMR experiments usually last several hours or even days[74]. Various methods, such as $^1H \rightarrow ^{29}Si$ CP and Carr-Purcell-Meiboom-Gill (CPMG), have been introduced to improve the sensitivity of ^{29}Si

NMR[75]. Sensitivity enhancement of many orders of magnitude has recently been achieved using DNP at high field under MAS for mesoporous silica impregnated with solutions of nitroxide biradicals[45,49,76,77].

II.6. Probing ^{29}Si-^{29}Si connectivities and proximities

The building units of the silica-based materials and their relative proportions could be determined from one-dimensional (1D) ^{29}Si NMR spectra acquired using CPMAS or DEMAS experiments. However, two-dimensional (2D) homonuclear correlation spectra are required to probe connectivities and proximities between the different ^{29}Si local environments. Furthermore, the additional spectral dimension could allow a greater separation of the signals. In these 2D spectra, the individual isotropic $\delta_{iso}(^{29}Si)$ of each nucleus is shown for the direct dimension while the indirect dimension displays the $\delta_{iso}(^{29}Si)$ for the single quantum (SQ)-SQ experiments and the sum of $\delta_{iso}(^{29}Si)$ of the correlated sites for the double quantum (DQ)-SQ ones. These ^{29}Si 2D homonuclear correlation experiments provide information about (i) the connectivities between ^{29}Si sites when the ^{29}Si-^{29}Si coherence transfer relies on *J*-coupling and (ii) the spatial proximities when the transfer relies on the dipolar coupling. These two types of experiments are discussed below.

II.6.1. Through-bond correlation experiment

The INADEQUATE (Incredible Natural Abundance DoublE QUAntum Transfer Experiment) pulse sequence was first proposed by Bax and coworkers[78] to facilitate the assignment of spectral peaks and to probe the direct scalar proximities between homonuclei in liquid-state NMR spectroscopy. The spectra obtained from INADEQUATE selectively provide information on coupled nuclei, while preventing the observation of isolated ones. This sequence was then

adapted for ssNMR with the work of Nakai et al.[79] and Lesage et al.[80]. The pulse sequence of this "refocused" INADEQUATE is presented in Figure II.2.

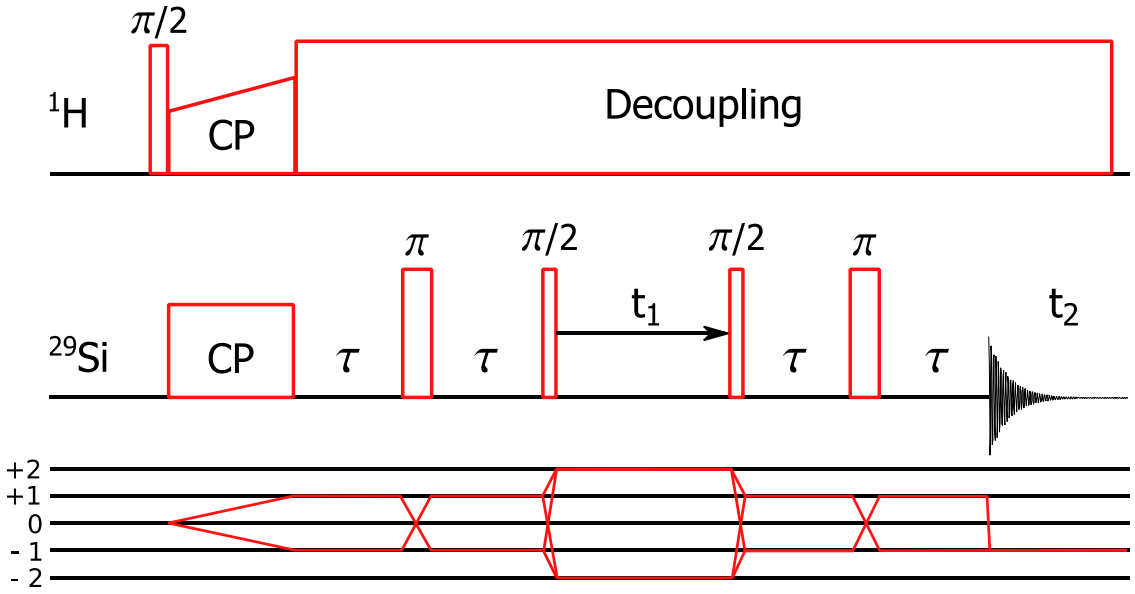

Figure II.2. The pulse sequence of 2D refocused INADEQUATE and its coherence transfer pathway diagram.

The pulse sequence starts with a CP block where magnetization from the proton bath is transferred to nearby ^{29}Si nuclei. During the following τ-π-τ period, this created transverse ^{29}Si magnetization is only subjected to the isotropic scalar (J) coupling since the homonuclear dipolar couplings are averaged by the MAS, the heteronuclear couplings are removed by the proton rf decoupling, while the chemical shifts are refocused by the spin-echo. The magnetization evolves under the J-coupling interaction into anti-phase coherence, which is then converted to DQ and ZQ coherences under the application of the following π/2 pulse. The DQ coherence only, selected by the phase cycling[79], evolves during the t_1 period. For the refocused INADEQUATE, the second π/2 pulse and τ-π-τ period are applied so that the DQ coherence is converted into in-phase SQ before acquisition. Since DQ and SQ terms are involved in the indirect and direct

dimensions, respectively; the obtained spectrum will present peaks as the sum of isotropic $\{\delta_i + \delta_j\}$ of coupled nuclei $\{i,j\}$ in the indirect dimension against the individual δ_i or δ_j in the direct dimension.

According to the product operator analysis of the pulse sequence[81], the spin-echo delay (τ) is set equal to $1/(4J)$ in order to maximize the observable signal for an isolated pair of ^{29}Si nuclei. In fact, for an isotropically unmodified Si-containing sample, owing to the low natural abundance of ^{29}Si, the majority of ^{29}Si nuclei have at most one single ^{29}Si nearest neighbor.

II.6.2. Through-space correlation experiment

MAS can provide sufficiently high-resolution spectra since it partially averages out anisotropic interactions, such as the chemical shift anisotropy (CSA) and dipolar coupling interactions. However, the latter interaction enables the investigation of spatial proximities of nuclei and the determination of their internuclear distance because the magnitude of the dipolar coupling is proportional to the inverse cubic distance between the spins, r^{-3}. A train of rf pulses (in this case defined as a "recoupling sequence") can be constructed to recover this dipolar coupling interaction.

A general pulse sequence scheme using a recoupling sequence is sketched in Figure II.3.

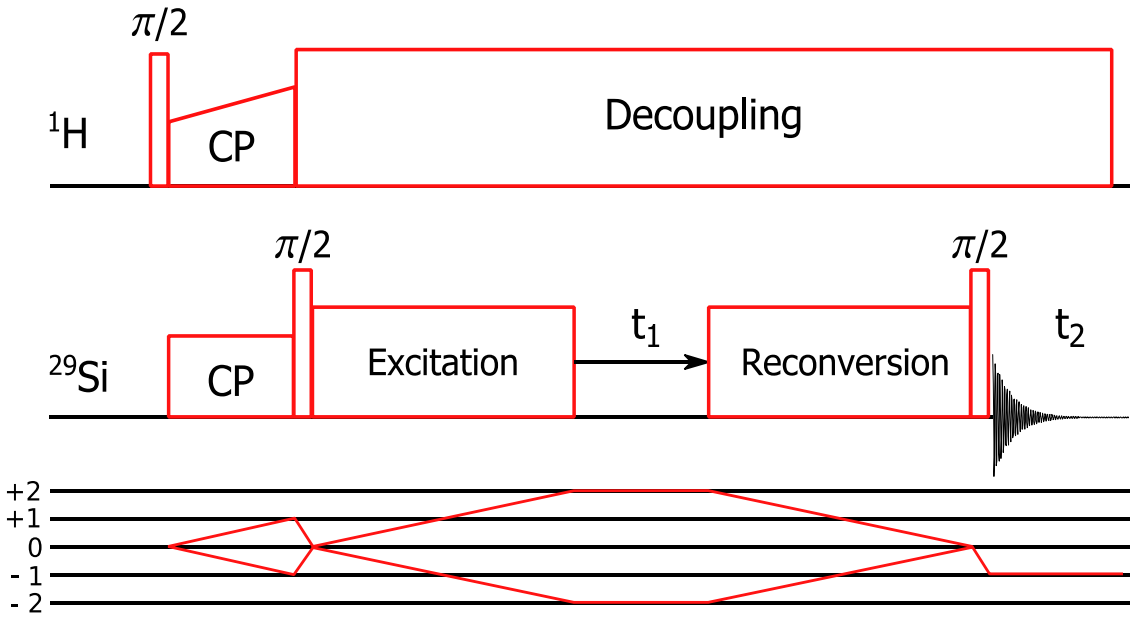

Figure II.3. A general pulse sequence for a DQ-SQ correlation experiment and its coherence transfer pathway.

Different recoupling sequences could be used for the excitation and reconversion periods in DQ-SQ through-space correlation experiments, such as POST-C7 (pC7)[82], SR26[83], S_3 and [S_3][84]. The details of these recoupling sequences are thoroughly described in the associated literature. Here, the experiment also starts with a CP block, aiming at selecting ^{29}Si nuclei in the vicinity of protons and increasing their sensitivity. The following π/2 pulse will flip the created transverse magnetization into the *z*-direction, and then the excitation block converts this longitudinal term (I_{1z}) into a DQ coherence term via the dipolar coupling to a second ^{29}Si nucleus. The DQ coherence evolves during the incremented t_1 period, and then the reconversion block will convert this DQ coherence back into I_{1z} and I_{2z}, and then the signal is detected with the application of a "reading" π/2 pulse, which rotates the longitudinal magnetization into observable transverse magnetization.

II.7. Siloxane-functionalized SiO_2 NPs

II.7.1. Applications in industry

Fuel cells have been considered as an advanced technology in the field of electricity since they can provide higher efficiency energy generation with no waste products such as SO_x, NO_x, CO_2 etc[85]. Proton exchange membranes are an integral part of a fuel cell, determining the lifetime of the whole system; thus tremendous efforts have been performed to make this membrane more durable and less costly[85]. Lengthening the membrane's durability requires a better understanding of the physical and chemical degradation mechanisms. Chemical degradation is often more detrimental. Such degradation involves the formation of hydroxyl and hydroperoxyl radicals[85] during the fuel cell process.

One of the solutions is the addition of sacrificial molecules, which can scavenge degradation species. For instance, polyethylsiloxane (PES) functionalized silica NPs is a model of a sacrificial system, which has been proposed for fuel cells[86].

In order to achieve the aim of lessening the effect of chemical degradation, careful sample preparation conditions are required, which is further described in the following section.

II.7.2. Sample Preparation

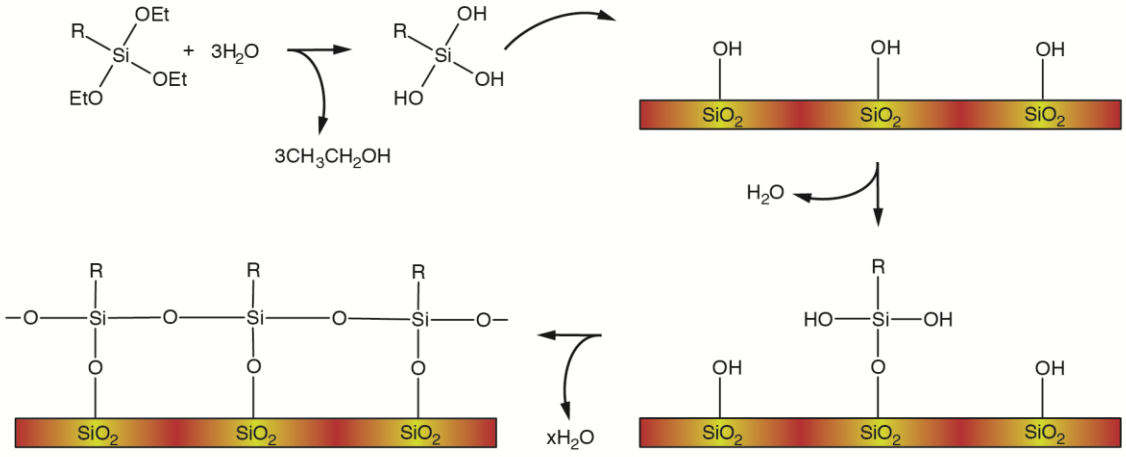

Figure II.4. A scheme for the hydrolysis of triethoxysilanes and then lateral self-condensation on the surface of silica NPs to form an ideal monolayer. Adapted from Ref. 86.

PES-functionalized silica NPs were prepared by the addition of colloidal silica NPs in water into a solution of ethyl triethoxysilanes in N-methyl-2-pyrrodine. The ideal product should be lateral condensation of PES to form a monolayer on the silica NPs surface as shown in Figure II.4, since this geometry will (i) maximize the probability of functionalizing groups accessing the degradation species, thus reducing their unfavorable effects on the membrane and (ii) avoid the elution of the functionalizing groups by the water produced during the fuel cell process.

Knowing the extent of self-condensation of alkylsiloxanes on the silica NPs produced from the specific reaction is significantly important for a rational improvement of the membrane durability; hence a thorough understanding of the surface structure of these sacrificial systems is required, for which the MAS-DNP technique is highly qualified to probe.

II.8. Numerical simulations

Before going into details of the experiments, numerical simulations were performed by SPINEVOLUTION (SPINEV) software[87] to select the most suitable recoupling sequence for structural characterization. The selection process bases on the results of two sets of simulations:

1. The transfer efficiency of recoupling sequences under different CSA interactions;
2. The contribution of further nuclei to desired short-distance correlations for different recoupling sequences.

A spin system for simulations was defined, consisting of two coupled ^{29}Si nuclei. The isotropic chemical shift, $\delta_{iso}(^{29}\text{Si})$, was set to 0 kHz for both, while the CSA parameter, $\delta_{aniso}(^{29}\text{Si})$, was varied. The internuclear distance was equal to 3.0 or 5.0 Å, corresponding to a dipolar coupling constant of ~ −170 Hz or ~ −40 Hz, respectively. Both ^{29}Si nuclei were subject to the dipolar interaction as well as the same CSA interaction. All simulations were performed at B_0 = 9.4 T and at a MAS frequency ($\omega_R/2\pi$) of 5 kHz for pC7 and SR26; and 13.889 kHz for S_3 and [S_3].

The starting operator is I_{1z} while the detection operator is I_{2z}. DQ coherence alone is selected in between the excitation and reconversion blocks. The powder averaging was accomplished using 3600 orientations (144 $\{\alpha_{MR},\beta_{MR}\}\times$25 γ_{MR}). The $\{\alpha_{MR},\beta_{MR},\gamma_{MR}\}$ are the Euler angles define the rotation from Molecular frame (M) to the Rotor frame (R) in MAS experiments. These$\{\alpha_{MR},\beta_{MR}\}$ pairs were selected according to the Zaremba – Conroy – Wolfsberg (ZCW)[88] algorithm.

The signal intensity of I_{1z} is normalized and the transfer efficiency is defined as the ratio of the acquired magnetization of I_{2z} through the DQ filter to this value.

II.8.1. Build-up curve simulations for recoupling sequences at different values of CSA

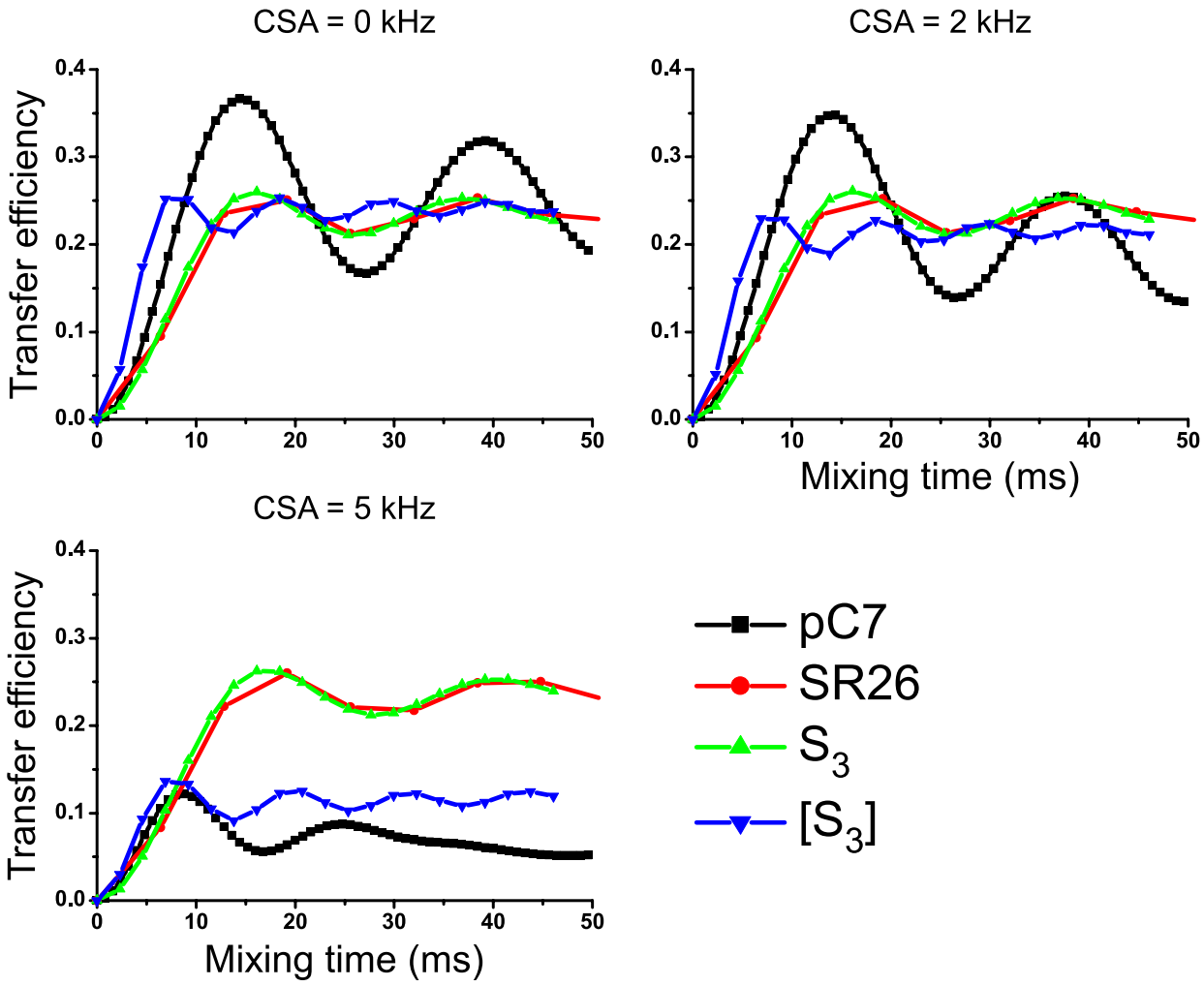

Figure II.5. Numerical simulations of transfer efficiencies of the diagonal peak (Δ_{iso} = 0) as a function of the mixing time (the sum of the lengthes of the excitation and reconversion blocks) for different recoupling sequences, simulated at different CSA values, namely $\delta_{aniso}(^{29}Si)$ = 0; 2; and 5 kHz for a ^{29}Si-^{29}Si system at B_0 = 9.4 T and $\omega_R/(2\pi)$ = 5 kHz for pC7 and SR26 or 13.889 kHz for S_3 and [S_3]. The spin system consists of two ^{29}Si nuclei, $d_{Si\text{-}Si}$ = 3.0 Å, corresponding to the dipolar coupling of ~ –170 Hz, and the δ_{iso} of both nuclei was 0 kHz. The rf-induced nutation

frequencies from the recoupling sequences were 35 kHz for pC7 (■), 32.5 kHz for SR26 (●), and ~ 7 kHz for both S_3 (▲), and [S_3] (▼).

At CSA = 0 kHz compared to 2 kHz, the build-up curves for all recoupling sequences do not significantly change, as shown in Figure II.5. In terms of transfer efficiency magnitude, the pC7 sequence provides the highest value since it is γ-encoded[89] while the others, which are non-γ-encoded, show rather similar intensities. However, at CSA = 5 kHz, while the transfer efficiencies of pC7 and [S_3] are considerably reduced, namely from 35 % to 15 % and from 25 % to 15 %, respectively, those of S_3 and SR26 remain constant. This indicates that S_3 and SR26 are more robust to a CSA interaction than pC7 and [S_3].

As shown later in a 1D $^{1}H \rightarrow ^{29}Si$ CPMAS experiment, $\omega_R/(2\pi)$ = 5 kHz could yield a high-resolution spectrum without the occurrence of any large spinning sidebands. This indicates that the CSA interaction of the PES-functionalized silica NPs is smaller than 5 kHz.

To determine an accurate internuclear distance, it is required that the recoupling sequence only probes the shortest internuclear distances. The aim of the next simulation is to study the contribution of longer distances at different values of CSA.

II.8.2. Build-up curve simulations of recoupling sequences for different ^{29}Si-^{29}Si bond lengths and different CSA values

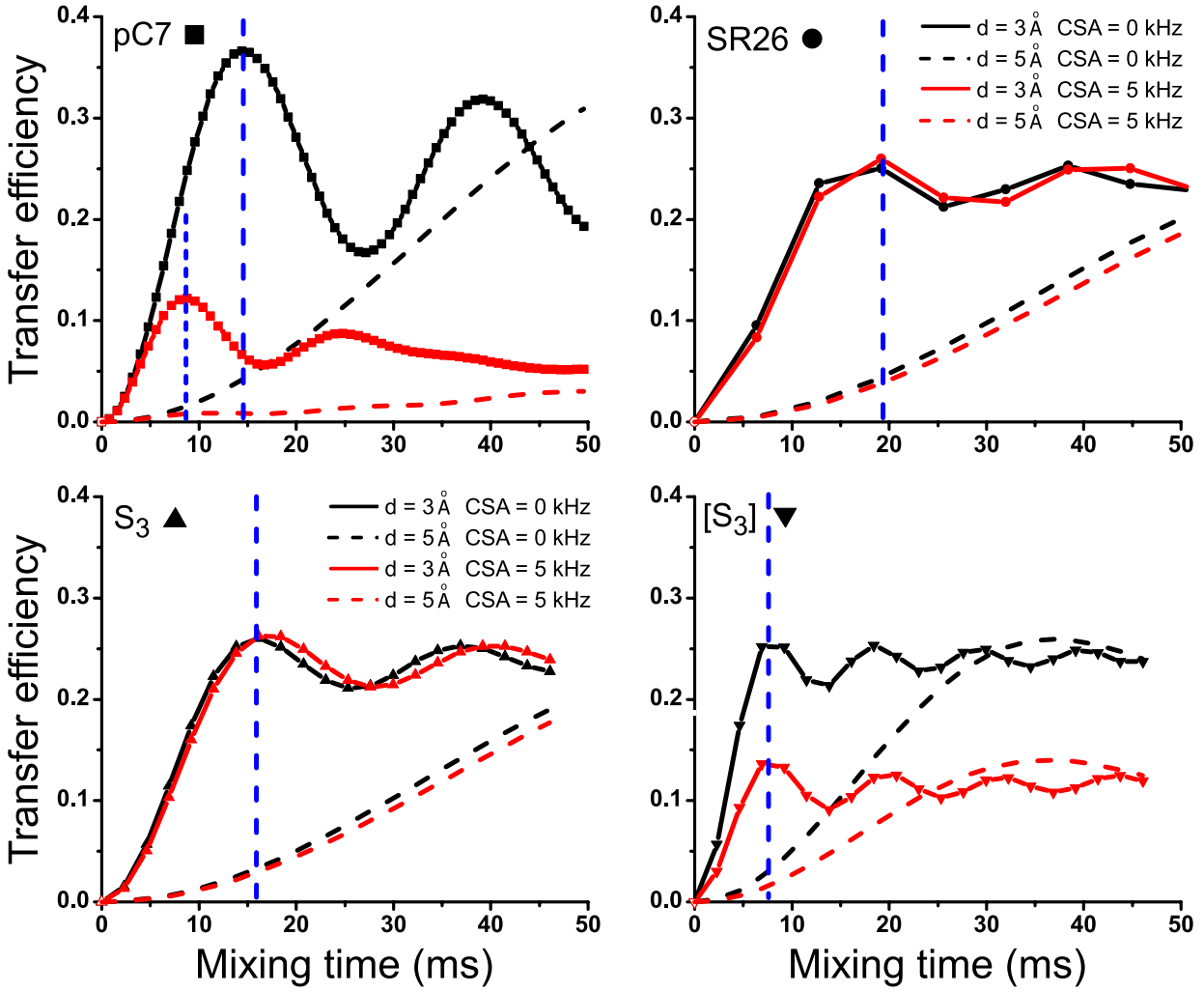

Figure II.6. Numerical simulations of transfer efficiencies of the diagonal peak (Δ_{iso} = 0) as a function of the mixing time for different recoupling sequences, simulated at different internuclear distances for a ^{29}Si-^{29}Si system at B_0 = 9.4 T and $\omega_R/(2\pi)$ = 5 kHz for pC7 and SR26 or 13.889 kHz for S_3 and [S_3]. The spin system consists of two ^{29}Si nuclei, $d_{Si\text{-}Si}$ = 3.0 (—) or 5 Å (---), corresponding to dipolar couplings of ~ –170 Hz and ~ –40 Hz, respectively. The rf-induced nutation frequencies from the recoupling sequences were 35 kHz for pC7 (■), 32.5 kHz

for SR26 (●), and ~ 7 kHz for both S_3 (▲), and [S_3] (▼). Simulations were performed using CSA values of 0 kHz (—) and 5 kHz (—). The vertical dashed blue lines show the optimum mixing time.

As shown in Figure II.6, the transfer efficiencies for the system with $d_{Si\text{-}Si}$ = 5.0 Å (longer correlation) were simulated and compared to those for the system with $d_{Si\text{-}Si}$ = 3.0 Å (short correlation) for different recoupling sequences.

Table II.2. The ratio of transfer efficiency between longer and shorter ^{29}Si – ^{29}Si correlations at different CSA values.

	pC7	SR26	S_3	[S_3]
CSA = 0 kHz	0.11	0.18	0.13	0.14
CSA = 5 kHz	0.05	0.16	0.13	0.12

As shown in Table II.2 in case of CSA = 0 kHz, the transfer efficiencies from the longer correlation is larger than 10 % compared to that of the shorter correlation for all recoupling sequences. Under such conditions, none of the recoupling sequences meets the requirement of selectively probing only short distance correlations.

At CSA = 5 kHz, pC7 differs from the other recoupling sequences in terms of contribution from the longer correlation. The simulations show that while SR26, S_3, and [S_3] provide similar build-up curves as in the case of CSA = 0 kHz, for pC7 the transfer efficiency of longer correlations is negligible compared to that of the shorter correlation. Therefore, it can be said that for a non-zero CSA, pC7 is the most suitable choice for internuclear distance determination.

II.9. Results and discussions

II.9.1. Experimental

For MAS-DNP experiments, PES-functionalized silica NPs were impregnated with 12 mM AMUPol[43] solution in [$^2H_6$]-DMSO/^2H_2O/H_2O (78/14/8 wt%) to form "DNP-ready" samples. The wet powder was put into a 3.2 mm outer-diameter sapphire rotor.

The DNP-NMR experiments were performed at 9.4 T on a Bruker BioSpin Avance III DNP-NMR spectrometer equipped with a triple resonance ^{1}H/X/Y 3.2 mm low temperature MAS probe and a 263 GHz gyrotron. The μw irradiation delivered by the gyrotron was transmitted through a corrugated waveguide, as described in Section I.6.1. The μw power delivered to the sample was a few Watts. The NMR spectra were acquired at a temperature of ~ 110 K. The sample was spun at $\omega_R/(2\pi)$ = 5 kHz.

The ^{1}H→^{29}Si CPMAS spectra of "DNP ready" samples were acquired with (μw on) and without (μw off) μw irradiation using an optimized CP contact time of 3 ms. During the CP process, the ^{1}H rf field frequency, ν_{rf}, was ramped linearly from 43 to 86 kHz, whereas the ^{29}Si ν_{rf} was constant and equal to ~ 60 kHz. The pC7 recoupling sequence and refocused INADEQUATE were used for acquiring the through-space and through-bond ^{29}Si homonuclear correlation experiments, respectively. For pC7, the total mixing time was 8 ms, meaning that 4 ms was used for the excitation and reconversion blocks. The spectral width in the indirect dimension was 17.5 kHz and the evolution time was 0.7 ms. The number of experimental transients (scans) acquired and summed for each t_1 increment was 448. During the recoupling mixing time, 130 kHz of CW Lee-Goldburg decoupling[2,90] was used, while during the indirect detection period, t_1, and the acquisition period, t_2, SPINAL-64[91] heteronuclear decoupling with

ν_{rf} of 100 kHz was used. The CW Lee-Goldburg decoupling is defined as an alignment of an effective field, created by the offset resonance and the ν_{rf}, at the MAS orientation. This decoupling sequence was shown to be the most favorable choice during symmetry-based recoupling sequences of low-to-moderate power since (i) it employs the higher rf field on protons and (ii) it avoids the ^{1}H-^{1}H interactions, which could destroy the desired information[92]. For refocused INADEQUATE, the τ delay was 14 ms, so the total *J*-evolution period was 56 ms. The spectral width in the indirect dimension was 17.5 kHz and the maximal evolution time was 0.4 ms. The number of scans was 768. During the whole sequence of refocused INADEQUATE, SPINAL-64[91] with ν_{rf} of 100 kHz was applied on the ^{1}H channel.

II.9.2. CPMAS experiment

^{1}H→^{29}Si CPMAS 1D spectra of PES-functionalized silica NPs are shown in Figure II.7.

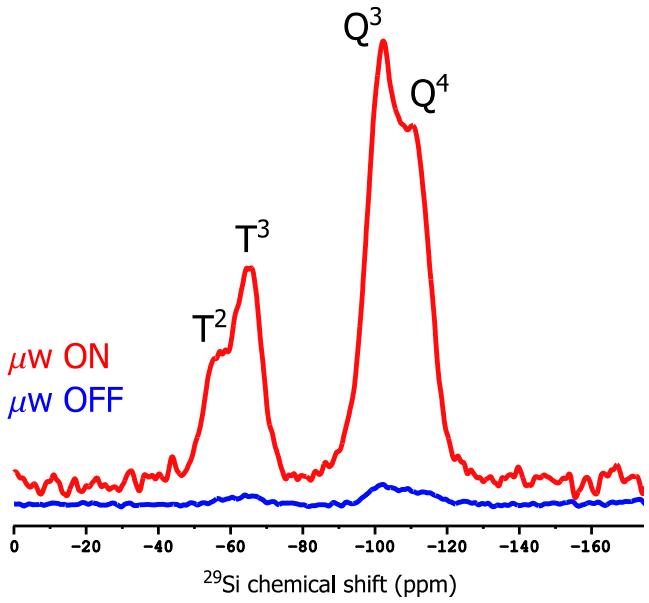

Figure II.7. ^{1}H→^{29}Si 1D CPMAS spectra of PES-functionalized silica NPs impregnated with 12 mM AMUPol solution in [$^{2}H_6$]-DMSO/$^{2}H_2O$/H_2O (78/14/8 wt%) performed at 9.4 T and $\omega_R/(2\pi)$ = 5 kHz, with (red) and without (blue) μw irradiation suitable for CE-DNP.

The DNP enhancement, $\varepsilon_{ON/OFF}$ ($^{1}H \rightarrow ^{29}Si$), was determined by comparing the signals of the CPMAS spectra recorded with and without applied μw irradiation. $\varepsilon_{ON/OFF}$ ($^{1}H \rightarrow ^{29}Si$) is 23 for the T sites ($\delta(^{29}Si)$ = -50 to -75 ppm), while it is 18 for the Q sites ($\delta(^{29}Si)$ = -90 to -115 ppm). The difference in enhancement between the T and Q sites possibly stems from the existence of buried silanol ^{1}Hs attached to Q sites in the bulk of the NPs[93]. These ^{1}Hs were either not hyperpolarized or polarized to a lesser extent compared to the surface ^{1}Hs owing to further distances to the electron sources or less efficient ^{1}H-^{1}H spin diffusion processes into the bulk, leading to the smaller $\varepsilon_{ON/OFF}$ ($^{1}H \rightarrow ^{29}Si$) for Q sites.

It was stated previously that the 1D experiment allows the investigation of which sites (T or Q building units) exist in the system, but such an experiment does not provide the structural information required on the geometry of the grafted PES on the surface of the silica NPs. Such information has been probed by 2D ^{29}Si - ^{29}Si correlation experiments.

II.9.3. 2D through-space and through-bond correlation experiments

The possibilities of bonded alkylsiloxane molecules on the surface of silica NPs are presented in Figure II.8.

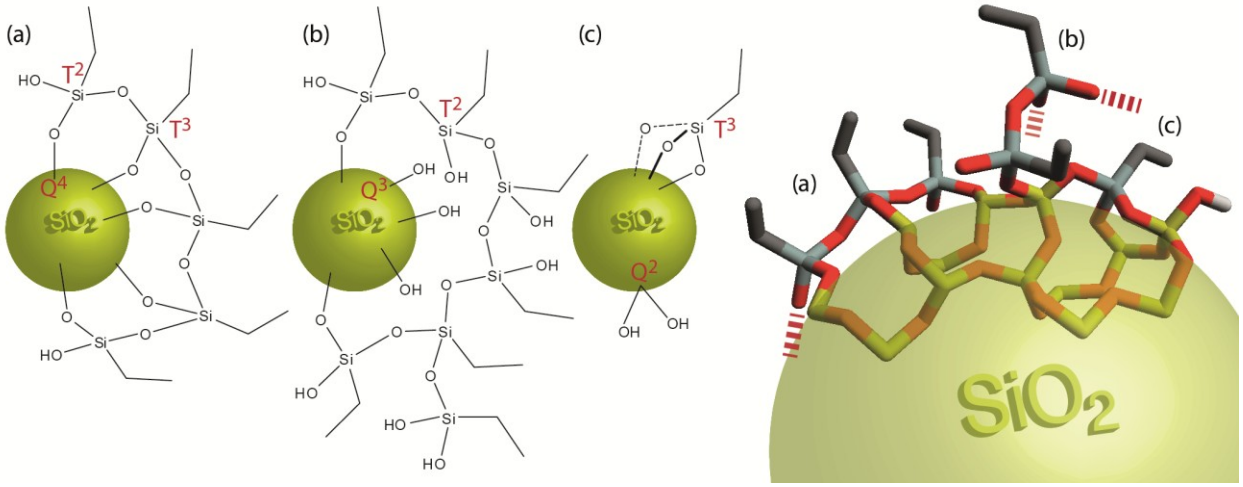

Figure II.8. The 2D scheme presents the possibilities of attaching organosiloxanes on the surface of the silica NPs: (a) laterally self-condensed (b) vertical core-shell oligomers above the surface and (c) discrete surface-bound monomers. The 3D scheme summarizes all the mentioned possibilities. The NPs Si, silane Si, O, C, and H atomic environments are presented as yellow, light grey, red, dark grey and white colors, respectively. Adapted from Ref. 86.

Owing to the enhancement gained (23 for T sites and 18 for Q sites), which corresponds to a substantial reduction in acquisition time, 2D correlation experiments become feasible in reasonable time. Figure II.9 shows such 2D through-space and through-bond ^{29}Si homonuclear correlation experiments.

Although in the simulations it was shown that the pC7 recoupling sequence only investigates the internuclear distances < 5 Å, the through-bond correlation experiment was still performed for confirmation of a direct connection between ^{29}Si nuclei. Since the $^{2}J^{\text{Si-O-Si}}$ coupling is in the range of 5-15 Hz[94], an order of magnitude smaller than the dipolar coupling, it thus requires longer time to reach maximum transfer efficiency. Owing to the longer required build-up time, the intensity of the 2D homonuclear through-bond experiment severely suffers from transverse relaxation (T_2'(^{29}Si)), which reduces the overall transfer efficiency, making the through-bond correlation experiment much less efficient than the through-space experiment.

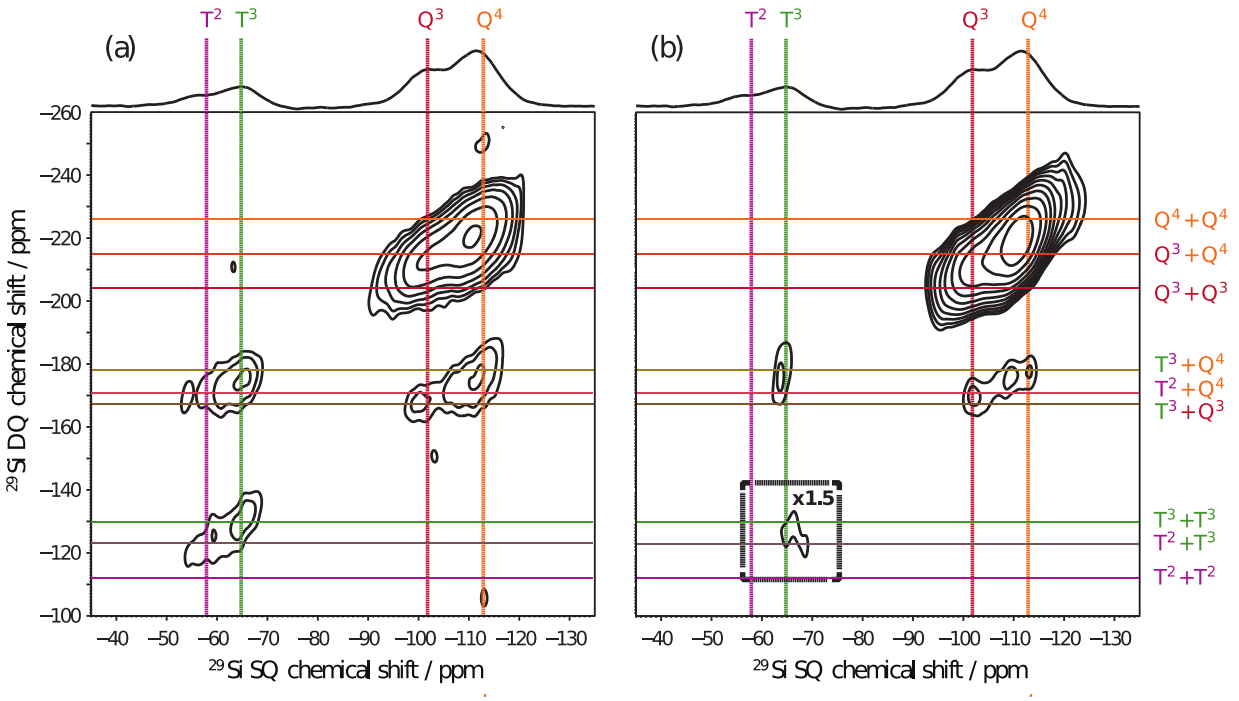

Figure II.9. 2D DNP-enhanced ssNMR ^{29}Si-^{29}Si (a) through-space and (b) through-bond correlation experiments on the PES-functionalized silica NPs. The details of these two experiments are given in Section II.9.1. Adapted from Ref. 86.

Regarding the surface of the silica NPs, selected via the use of CP, Q^4-Q^4, Q^4-Q^3, and Q^3-Q^3 correlations are clearly observed. The occurrence of Q^4-Q^4 and Q^4-Q^3 correlations could be expected since the bulk silica is mainly composed of Q^4 sites and the surface of Q^3 sites. However, the occurrence of Q^3-Q^3 correlations indicates that the condensation of functionalizing molecules does not take place on the whole of the surface of the silica NPs, leaving clusters of silanols.

For the alkylsiloxanes part, T^3-T^3, and T^3-T^2 correlations are observed while T^2-T^2 correlations are not. The T^2-T^2 correlations mean that two species attach to each other to form a surface dimer and no more alkylsiloxane species could be added to this dimer or, in other words, the condensation ends at this point. The T^2 sites play a role of ending a chain. The observation of

T^3-T^3 and T^3-T^2 correlations means that alkylsiloxanes self-condense and bond to each other. While T^3 sites are able to lengthen the chains of T^3-T^3 connections, the T^2 sites end these chains. The question raised here is whether the self-condensation happens on the surface (lateral condensation) or away from the surface (vertical condensation).

For alkylsiloxanes grafted on the silica NPs' surface, T^3-Q^4, T^2-Q^4, and T^3-Q^3 correlations are clearly observed. These observations show that the functionalizing molecules bind to the surface. Comparing the intensities of the peaks of T^3-Q^4 and T^3-T^3 correlations rationalizes how functionalizing molecules condense on the surface of the silica NPs. Three cases could possibly happen.

1. The intensities of T^3-Q^4 and T^3-T^3 correlations are similar. This means that T^3 sites bind to the surface and favor lateral condensation instead of the vertical condensation, as shown in Figure II.8a.

2. The intensities of T^3-T^3 correlations are larger than those of T^3-Q^4 correlations. This means that T^3-T^3 connections favor vertical condensation away from the surface of the silica NPs, as illustrated in Figure II.8b.

3. The intensities of T^3-T^3 correlations are smaller than those of T^3-Q^4 correlations. This implies that the majority of T^3 sites exist as the monomers and these monomers are more favorably attached on the surface than self-condensed with other T^3 sites, as displayed in Figure II.8c.

Extraction of cross-sections (slices) through T^3-Q^4, and T^3-T^3 correlation peaks from the 2D homonuclear correlation experiments, shown in Figure II.10a, enables the confirmation of the most feasible possibility of condensing alkylsiloxanes on the surface of silica NPs.

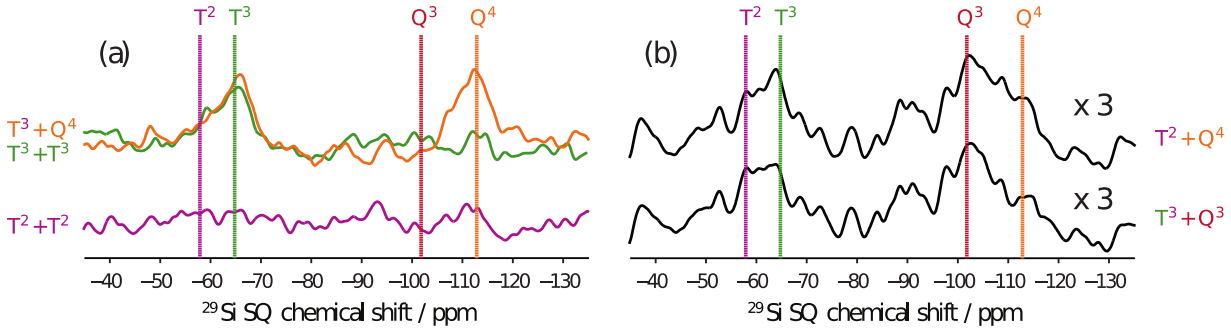

Figure II.10. Various cross sections extracted from the indirect dimension of the 2D ^{29}Si-^{29}Si (a) through-space and (b) through-bond. Adapted from Ref. 86.

The similarities in intensities of T^3-T^3 and T^3-Q^4 correlations are notably observed in Figure II.10a. Therefore, the results indicate that alkylsiloxane molecules favor lateral condensation on the surface of the silica NPs for this reaction procedure. It is noteworthy to mention that the intensities of T^3-T^3 correlations are slightly less than those of T^3-Q^4 correlations, which could be expected since T^3-T^3 correlation peaks will suffer more from signal decaying effects than T^3-Q^4 peaks. These results are all corroborated in the 2D homonuclear through-bond correlation spectrum shown in Figure II.9b. The effect of signal decaying was also clearly observed for the other correlation peaks such as T^2-Q^4 and T^3-Q^3 when comparing spectra of Figure II.9a and Figure II.9b. For the sake of clarity, the cross-sections of these aforementioned correlation peaks are extracted and illustrated in Figure II.10b, where their signal intensities are slightly above the detectable limit.

With all the information gained, it is concluded that alkylsiloxanes favor lateral condensation to form partial monolayers on the surface of silica NPs; the condensation experiments do not cover the whole surface of the silica NPs owing to the occurrence of clusters of silanols.

Further structural information could be extracted from build-up curves resulting from varying the mixing time during the 2D homonuclear correlation experiments.

For the pC7 build-up curve experiment, SPINEV software[87] was used to fit the integrated intensity of the Q^3 and Q^4 sites and provided for those sites a CSA value of ~ 4.8 ± 0.1 kHz and an average distance between Q sites equal to 3.15 ± 0.05 Å. The fitting between the simulated and experimental results is shown in Figure II.11a.

The refocused INADEQUATE build-up curve was obtained by incrementing the τ delay (instead of t_1, which was kept constant at 0.3 μs). Since this experiment uses spin-echo blocks, the observable intensities are affected by T_2' relaxation as well as the *J*-coupling interaction. For the analysis of the results, this relaxation time constant must be taken into account. T_2' values are measured to be 4.4 ± 1.3 and 43.0 ± 4.0 ms for Q sites, whose relative contributions are 23, and 77 %, respectively. The arise of the fast (T_2'(a)) and the slow (T_2'(b)) decaying components are possibly explained by the proximity of ^{29}Si nuclei to the paramagnetic polarizing agent molecules. The intensities of Q sites are then given by:

$$sin^2(2\pi J\tau).(0.23.e^{-\frac{4\tau}{T_2'(a)}} + 0.77.e^{-\frac{4\tau}{T_2'(b)}})$$

The fit of the experimental data to this analytical expression, as shown in Figure II.11b, yields a ${}^2J^{Si-O-Si}$ coupling magnitude of ~ 11.0 ± 1.0 Hz. This value is within the range of 5 – 15 Hz[94], hence it is in full agreement with the literature.

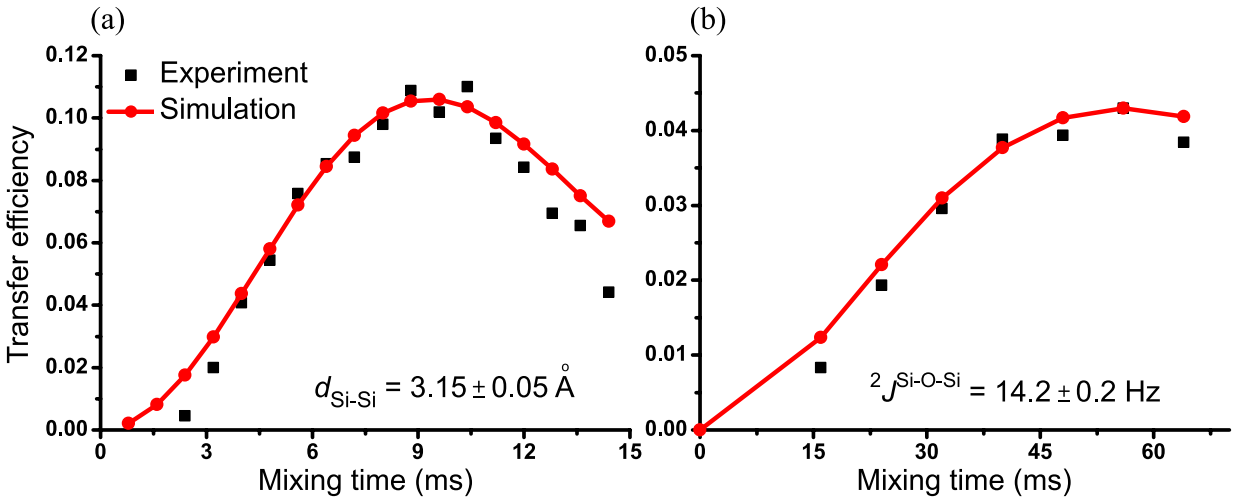

Figure II.11. Determination of (a) the internuclear distance and (b) the *J*-coupling magnitude of homonuclear-coupled ^{29}Si nuclei taken from comparing simulated (red) with experimental (black) data. Both simulations and experiments were carried out at B_0 = 9.4 T and $\omega_R/(2\pi)$ = 5 kHz. For the simulations, the spin system consists of an isolated pair of ^{29}Si nuclei.

The extracted internuclear distance and *J*-coupling interaction values could modify and/or minimize the possibilities of the structures predicted from DFT calculations as they apply more constraints to the structural models. The better understanding of the structure leads to the improvements in the design of sacrificial molecules for the membrane, thus enhancing the longevity of the fuel cell system.

II.10. Conclusions

Since siloxane-functionalized silica NPs are systems aiming at reducing the formation of degrading species, the information on the extent of surface condensation of these functionalizing groups on silica NPs is highly desired. It has been shown that MAS-DNP could overcome the sensitivity limitation of ^{29}Si NMR and facilitate the acquisition of previously impractical 2D ^{29}Si homonuclear correlation experiments. The collected data showed that at the current experimental

conditions, lateral condensation of the functionalizing groups is dominant owing to no significant evidence for vertical condensation of siloxanes away from the surface and/or discrete surface bound monomers. The results also showed that the reaction procedure did not provide ideal monolayer condensation since there were clusters of silanols left. Not only the condensation networks were elucidated but also structural parameters, namely the inter-nuclear distance of 3.15 ± 0.05 Å and the *J*-coupling magnitude of 11.0 ± 1.0 Hz. These two values could be used as constraints applied to DFT calculations, which will further help to refine theoretical model structures. A better understanding of the structure allows the optimization of the grafting of the functionalizing groups to the surface of silica NPs and hence of the durability of fuel cells.

Chapter III ATOMIC-LEVEL CHARACTERIZATION OF THE STRUCTURES OF ALUMINAS USING DNP-ENHANCED SOLID-STATE NMR

III.1. The importance of alumina

Aluminas (Al_2O_3) are a class of materials industrially produced on the scale of multimillions of tons per year. Depending on the annealing temperature of the hydrated aluminium oxide source, different polymorphs can be accessed. Dehydration of bohemite (AlOOH), for instance, affords ultimately the crystalline form α-Al_2O_3, also known as corundum.

Other forms of alumina with higher specific surface area have been developed for catalysis-related applications. These forms include γ-alumina and mesoporous alumina. γ-alumina (γ-Al_2O_3) is employed for several industrial processes as an adsorbent, a catalyst, and catalyst support owing to its large surface area (300 $m^2.g^{-1}$) and its acid/base characteristics[95]. For instance, γ-Al_2O_3 is used as a catalyst for the dehydration of alcohols to olefins and in the Claus process, in which sulfur is produced from H_2S[47]. Another promising alumina with high specific surface area is m-Al_2O_3[57,96]. This synthetic material contains highly ordered mesopores with uniform size. For instance, this material was used as a catalyst support in biodiesel production and hydrodesulfurization processes[50].

Despite being widely used, the structures of these materials are still not well understood since they do not form single crystals. For atomic-scale characterization of such systems, ssNMR is a suitable method but it suffers from its intrinsic low sensitivity, preventing the detection of surface sites, which are of catalytic interest. This issue is worse for quadrupolar nuclei, such as ^{27}Al and ^{17}O, since the intricate spin dynamics of these isotopes in the presence of rf field results in low efficiency for NMR experiments. The next section briefly

presents ssNMR of quadrupolar nuclei and explains how the quadrupolar interaction can decrease the resulting sensitivity.

III.2. Quadrupolar nuclei and their NMR spectra

Unlike spin-1/2 isotopes, quadrupolar nuclei ($I > ½$) exhibit a non-spherical electrical charge distribution. Hence, besides the magnetic interaction between the magnetic moment and the external magnetic field, quadrupolar nuclei are subject to an electric interaction, the quadrupolar interaction, between the nuclear electric quadrupolar moment, eQ, and the electric field gradient (EFG).

The quadrupolar interaction is defined by the quadrupolar coupling constant, C_Q, and the asymmetry parameter, η_Q:

$$C_Q = \frac{eQ.V_{ZZ}}{h} \qquad \text{and} \qquad \eta_Q = \frac{V_{XX} - V_{YY}}{V_{ZZ}},$$

where V_{ii} ($i = X$, Y, or Z) are the principal components of the EFG tensor, and h is the Planck constant.

In terms of magnitude, the quadrupolar interaction could be of the order of MHz; thus except the Zeeman interaction, it dominates the other interactions, such as rf field, chemical shift, and dipolar coupling. In NMR, the quadrupolar interaction can usually be described as a perturbation of the Zeeman interaction up to the second-order term.

The first-order term of the quadrupolar interaction is independent of the external magnetic field. It shifts the spin part of the $-m$ and $+m$ states by the same energy. Hence, it does not affect the central transition (CT) between energy levels m = -½ and +½ but affects the satellite transitions (ST) between energy levels m and $m \pm 1$ ($m \neq ½$). The spatial dependence of

the first-order quadrupolar interaction is similar to that of the CSA and dipolar coupling interactions. Thus this term can be averaged out by MAS.

The major difficulty for acquiring the high-resolution NMR spectrum of quadrupolar nuclei arises from the second-order quadrupolar interaction, whose frequency ($\eta_Q = 0$) could be written as:

$$\omega_Q^{(2)} \sim \frac{(\omega_Q^{PAS})^2}{\omega_L}[A + B.P_2(cos\beta_{RL}) + C.P_4(cos\beta_{RL})] \qquad \text{where } \omega_Q^{PAS} = \frac{3\pi C_Q}{2I(I-1)},$$

where ω_L is the Larmor frequency of nuclei of interest, and $P_k(cos\beta_{RL})$ is the k^{th}-order Legendre polynomial. β_{RL} is the angle between the magnetic field and the spinning axis. A, B, and C are coefficients.

This second-order quadrupolar frequency is proportional to $(C_Q)^2$ and inversely proportional to B_0. Unlike the first-order term, it affects both the CT and STs. Furthermore, the second-order quadrupolar interaction is only partially averaged by MAS since $P_4(cos\beta_{RL})$ is not averaged at magic angle. Hence, the CT under MAS is broadened by the remaining part of the second-order quadrupolar interaction. Such broadening can be seen by comparing the simulated ^{27}Al spectra shown in Figure III.1.

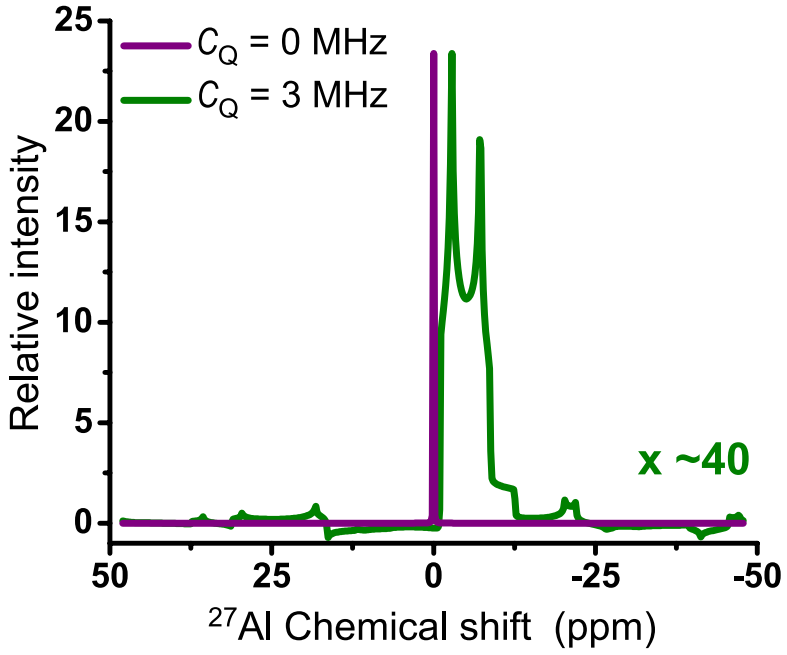

Figure III.1. Simulated ^{27}Al spectra of an isolated ^{27}Al nucleus. The quadrupolar parameters are C_Q = 0 MHz (violet) or 3 MHz (green) and η_Q = 0.25. The simulations were performed at B_0 = 9.4 T, $\omega_R/(2\pi)$ = 8 kHz. The powder averaging was accomplished using 100 orientations (100 $\{\alpha_{MR},\beta_{MR}\}\times 1\ \gamma_{MR}$). The $\{\alpha_{MR},\beta_{MR}\}$ pairs were selected according to the Alderman – Solum – Grant (ASG) algorithm[97]. The other spin interactions were disregarded. The simulations were performed using SPINEV software[87].

Figure III.1 compares ^{27}Al CT intensities in two cases: C_Q = 0 (violet) and 3 MHz (green). For C_Q = 0 MHz, a thin lineshape (violet) spectrum is obtained. For C_Q = 3 MHz, the CT is broadened by the second-order quadrupolar interaction and there is a corresponding 40-fold reduction of the signal peak height. Furthermore, such broadening will mask differences in isotropic chemical shifts.

As mentioned in Section III.1, alumina systems are mainly used as catalysts, catalyst supports, and adsorbents. For such applications, the chemical properties are controlled by the

surface structure since adsorption phenomena and catalytic reactions occur in this region. $^{1}H \rightarrow ^{27}Al$ coherence transfer can allow a selective observation of the surface since these isotopes are only close to one another in the surface region.

Such $^{1}H \rightarrow ^{27}Al$ coherence transfer can, for instance, be achieved by CP. Ellis and coworkers used $^{1}H \rightarrow ^{27}Al$ CP for the study of the surface of alumina[98]. Nevertheless, the set up of this experiment is often difficult owing to the intricate spin dynamics of quadrupolar nuclei under MAS combined with spin-locking. In the context of this work, a simulation was performed on a system consisting of a ^{27}Al nucleus with C_Q = 3 MHz, η_Q = 0.25, and $\omega_R/(2\pi)$ = 8 kHz. The powder averaging is similar as defined in Figure III.1 caption. The spin-locking power is set relative to $\omega_R/(2\pi)$. The simulation result is presented in Figure III.2.

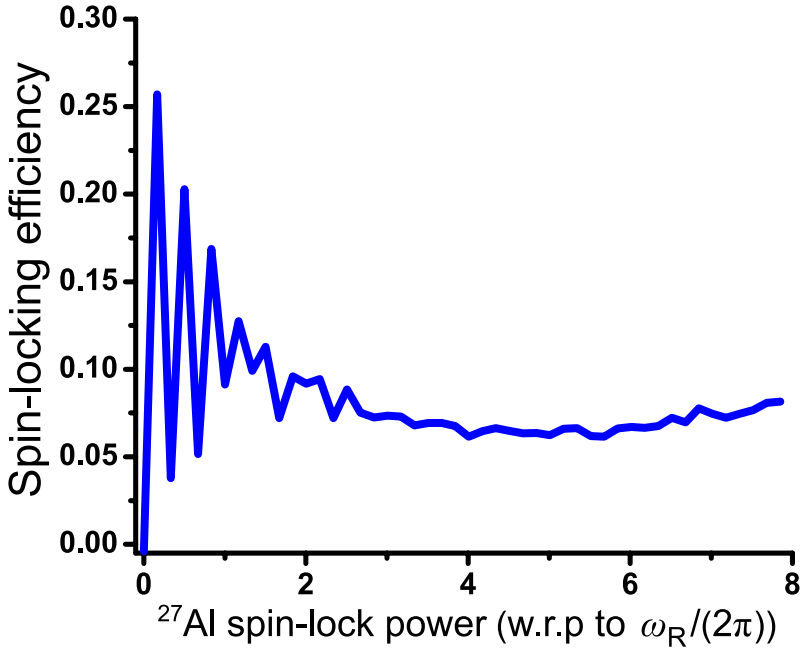

Figure III.2. Simulated ^{27}Al intensity as function of the ratio between the spin-locking rf field amplitude and the MAS frequency at B_0 = 9.4 T and $\omega_R/(2\pi)$ = 8 kHz. The simulation was performed for an isolated ^{27}Al nucleus subject to quadrupolar interaction with C_Q = 3 MHz and

η_Q = 0.25. The starting and detection operators are I_{1x} and the one corresponding to the CT (-1)-quantum coherence, respectively. The length of the spin lock was 6 ms and the intensity is given relative to a spin lock of 0 ms.

It is clearly observed from Figure III.2 that an efficient spin-locking of ^{27}Al transverse magnetization requires low-power rf field in order to manipulate selectively the CT. Figure III.2 also shows that the spin-locking efficiency drops around the rotary resonance conditions[99], namely when the nutation frequency of the ^{27}Al CT is equal to an integer number of $\omega_R/(2\pi)$. The rf nutation frequency, ν_1, of the CT is given by $(I+1/2)\nu_{rf}$. ^{27}Al transverse magnetization could also in principle be spin-locked by the use of an rf field much larger than the quadrupolar interaction but such rf fields are not accessible with current NMR probes for the nuclei studied here.

Overall, although ssNMR is a powerful technique to characterize the atomic-level structures of materials, pulse sequences irradiating quadrupolar nuclei, such as ^{27}Al, often exhibit low efficiency owing to the broadening produced by the quadrupolar interaction and the intricate spin dynamics of quadrupolar nuclei in the presence of rf field and MAS. We show below how this low efficiency can be circumvented by the use of DNP.

III.3. Experiments

Sample preparation

γ-Al_2O_3 nanopowder was purchased from Sigma-Aldrich and used as received without further treatment while m-Al_2O_3[57] was prepared according to the procedure reported in the literature.

MAS DNP-NMR at low temperature

The DNP-NMR experiments were performed at 9.4 T or 18.8 T[†] on Bruker BioSpin Avance III DNP-NMR spectrometers equipped with triple resonance ^{1}H/X/Y 3.2 mm low temperature MAS probes and a 263 or 527 GHz gyrotron (for 9.4 T and 18.8 T, respectively). The μw irradiation delivered by the gyrotrons was transmitted through corrugated waveguides. The μw power delivered to the sample was of the order of a few Watts. The NMR spectra were acquired at a temperature of ~ 100 K for experiments at 9.4 T and approximately 130 K for those at 18.8 T. The temperature was controlled by a Bruker BioSpin MAS cooling system. The sample was spun at $\omega_R/(2\pi)$ = 13.889 kHz for experiments at 9.4 T and 10 kHz for those at 18.8 T.

Aluminas were impregnated with a DNP matrix (polarizing agent dissolved in a suitable solvent or solvent mixture) to form "DNP-ready" samples. The wet powder was put into a 3.2 mm thin-walled zirconia rotor, which is devoid of ^{27}Al background signal, contrary to sapphire rotors.

MAS-DNP at 9.4 T

For a hydrophilic sample preparation, the DNP matrix was TOTAPOL[39] or AMUPol[43] as the polarizing agent, dissolved in [$^{2}H_6$]-DMSO/$^{2}H_2O$/H_2O (78/14/8 wt%). For a hydrophobic sample preparation, the DNP matrix was the bTbK[41] polarizing agent dissolved in 1,1,2,2-tetrabromoethane (TBE).

The ^{1}H→^{27}Al CPMAS spectra of "DNP ready" samples of γ-Al_2O_3 were acquired with and without μw irradiation using an optimized CP contact time and rf nutation frequency, ν_1,

[†] I would like to acknowledge TGIR-RMN organization for providing me an opportunity to work at the 18.8 T MAS-DNP system.

values of ~ 33 kHz and ~ 19.5 kHz for the spin lock pulses applied on ^{1}H and ^{27}Al channels, respectively.

The length of the soft and selective π/2- and π-pulses applied for ^{27}Al was 6 and 46 μs; respectively using ν_{rf} ~ 14 kHz.

2D ^{27}Al 3QMAS[100] spectra of γ-Al_2O_3 impregnated with 5 mM bTbK in TBE were acquired using a *z*-filtered sequence[101]. The length of excitation and conversion pulses was equal to 5.5 and 2.0 μs respectively, using ν_{rf} = 72 kHz. A soft π/2 "CT-selective" pulse was applied for detection. The 2D 3QMAS spectrum results from the averaging of 60 transients for each of 64 t_1 increments with a recycle delay of 6 s, i.e. a total experimental time of 6.5 hours.

The CP-3QMAS[102] spectrum was based on the 3QMAS experiment. The excitation pulse is replaced by a CP transfer step, in which the rf field amplitudes for ^{1}H and ^{27}Al irradiations are 56 and 84 kHz, respectively; and the CP contact time was 0.55 ms. The 2D CP-3QMAS spectrum results from the averaging of 192 transients for each of 64 t_1 increments with a recycle delay of 2.1 s, i.e. a total experimental time of ~ 7 hours.

The 3QMAS spectra of ^{27}Al nuclei residing in the bulk of the material were acquired using a *bulk-filtered* 3QMAS sequence. This sequence derives from the *z*-filtered 3QMAS but a bulk-filter block (*see* section III.6) is inserted between the CT-selective pulse and the acquisition period, t_2. The length of the spin echo in the bulk-filter was optimized through 1D experiment and was equal to 3 ms in 2D experiments.

The ^{27}Al homonuclear dipolar-mediated correlation experiment of γ-alumina starts with a CP step of 0.55 ms with similar parameters to those from the 1D ^{1}H→^{27}Al CPMAS experiments. The $BR2_2^1$ pulse sequence[58] was used with ν_{rf} = 2.3 kHz. The 2D spectrum results from the

averaging of 128 transients for each of 36 t_1 increments with a recycle delay of 5.5 s, which means a total experimental time of ~ 7 hours.

MAS-DNP at 18.8 T

For DNP-NMR experiments, m- and γ-Al_2O_3 powders were impregnated with 12 mM AMUPol in perdeuterated glycerol ([$^2H_8$]-glycerol), ^2H_2O, and H_2O (60, 30, 10 v%, respectively).

The $^1H \rightarrow ^{27}Al$ CPMAS spectra of the aluminas were acquired using an optimized CP contact time of 0.7 ms and ν_1 values of 25 and 15 kHz for the spin-lock pulses applied to ^1H and ^{27}Al nuclei, respectively.

III.4. Applicability and feasibility of MAS-DNP to the study of γ-alumina

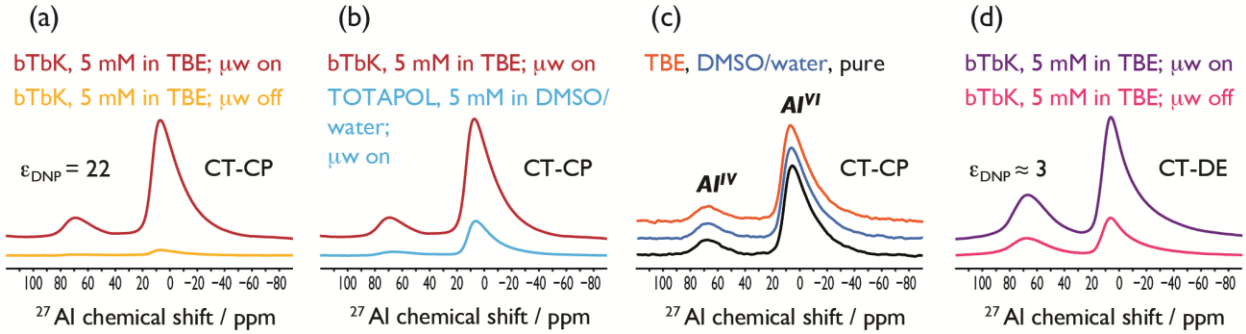

Figure III.3. ^{27}Al NMR spectra were acquired at B_0 = 9.4 T; $\omega_R/(2\pi)$ ~14 kHz and at a temperature of ~100 K. (a) ^{1}H→^{27}Al CT-CP spectra of γ-alumina impregnated with 5 mM bTbK in TBE with (red) and without (orange) μw irradiation; (b) ^{1}H→^{27}Al CT-CP spectra of γ-alumina impregnated with 5 mM bTbK in TBE (red) and 5 mM TOTAPOL in [$^{2}H_6$]-DMSO/$^{2}H_2O$/H_2O (blue) with μw irradiation. The intensities of the spectra in (b) are scaled according to their absolute sensitivity; (c) ^{1}H→^{27}Al CT-CP spectra of pure γ-alumina (top) and γ-alumina impregnated with TBE (middle) or [$^{2}H_6$]-DMSO/$^{2}H_2O$/H_2O mixture (bottom) without μw irradiation; (d) ^{27}Al CT-DE spectra of γ-alumina impregnated with 5 mM bTbK in TBE with (violet) and without (pink) μw irradiation. Adapted from Ref. 47.

Before attempting to study the structure of materials, the applicability of MAS-DNP is the first issue to be considered. Whether the addition of solvents for the DNP matrix changes the structure of the sample of interest was investigated by performing ^{1}H→^{27}Al Central-Transition Cross-Polarization (CT-CP) on pure γ-alumina (without solvent or radical), and γ-alumina impregnated with either a mixture of DMSO and water or TBE. The spectra obtained from the three cases exhibited two broadened peaks at around 5 ppm and 70 ppm, which are ascribed to tetra- (Al^{IV}) and hexa-coordinated (Al^{VI}) aluminium sites; respectively. Similar spectra resulted, as shown in Figure III.3c, which demonstrates that there is no significant change in the surface

structure of γ-alumina. This is an expected result since being used as received, the surface of this material is protected by layers of physisorbed and chemisorbed water molecules, which prevents any effect of the added solvents to the surface coordination. Although no modification in structure was observed, the addition of solvents is expected to change the NMR relaxation parameters. This is thoroughly analyzed in Section III.5.

Besides the applicability of MAS-DNP experiments to hydrated γ-alumina; the next question is the feasibility of this technique. Figure III.3a compares the signal intensities obtained from $^{1}H \rightarrow ^{27}Al$ CT-CP of γ-alumina impregnated with 5 mM bTbK in TBE with and without μw irradiation. For the MAS-DNP experiment, the sample was continuously irradiated with μw at the optimized frequency for the CE MAS-DNP mechanism to efficiently transfer the polarization from the unpaired electrons to the proton bath. Then the hyperpolarized protons transfer their polarization to coupled ^{27}Al nuclei via the CT-CP step. The signal enhancement $\varepsilon_{ON/OFF}$ ($^{1}H \rightarrow ^{27}Al$), defined as the ratio of the signal intensities with and without μw irradiation, is 22. This large enhancement gained by DNP would allow an almost 500-fold reduction in acquisition time.

$\varepsilon_{ON/OFF}$ allows the quick evaluation of the efficiency of the DNP process but does not assess the sensitivity gain produced by DNP-NMR with respect to conventional NMR experiments. The Absolute Sensitivity Ratio (ASR) was introduced for that assessment[51]. Besides $\varepsilon_{ON/OFF}$, the ASR accounts for other factors, such as signal losses (effective sample weight, paramagnetic bleaching, nuclear depolarization[36,37] etc.), the DNP build-up time, and spectral linewidths. The ASR is measured as the ratio of the signal-to-noise per unit square root of time between a MAS-DNP experiment and a conventional room temperature (RT) ssNMR experiment. Not only examining the worth of performing DNP experiments compared to

conventional ssNMR, the ASR also permits to assess different sample preparations. Figure III.3b compares the signal intensities of two DNP-enhanced $^{1}H \rightarrow ^{27}Al$ CT-CP spectra of γ-alumina recorded using different sample preparation methods. The signal intensities of the two spectra were scaled by the ASR and this shows that impregnation of γ-alumina with 5 mM bTbK in TBE results in higher NMR sensitivity than an impregnation with 5 mM TOTAPOL solution in [$^{2}H_6$]-DMSO/$^{2}H_2O$/H_2O.

While the experiments shown in Figure III.3a and Figure III.3b illustrate the indirect DNP enhancement, Figure III.3d displays the direct DNP enhancement of ^{27}Al signals. The CT direct excitation experiment performed on γ-alumina impregnated with 5 mM bTbK in TBE results in direct $\varepsilon_{ON/OFF}$ (^{27}Al) ~ 3, while for an impregnation of 5 mM TOTAPOL in [$^{2}H_6$]-DMSO/$^{2}H_2O$/H_2O, no enhancement was observed. There are several possible reasons for the significantly lower direct $\varepsilon_{ON/OFF}$ (^{27}Al):

(i) Nitroxide-based biradicals are designed for polarization transfer to ^{1}H nuclei, not ^{27}Al nuclei, so the proton bath will take most of the available hyperpolarization.

(ii) While protons are equally distributed in the solvents that are in direct contact with radical molecules, only ^{27}Al nuclei near the surface of nanoparticles could receive the hyperpolarization, not those in the bulk; therefore the average enhancement is smaller compared to $\varepsilon_{ON/OFF}$ (^{1}H).

The higher $\varepsilon_{ON/OFF}$ (^{27}Al) measured for the case with bTbK compared to TOTAPOL most likely stems from the fact that bTbK molecules are closer to the γ-alumina surface on average than TOTAPOL molecules. This point will be further verified in Section III.5.

Currently, the design of biradicals is mainly aimed at efficient polarization transfer to ^{1}H nuclei. However, the development of polarizing agents for direct hyperpolarization of target

nuclei, other than ^{1}H, is promising and required when studying systems that are devoid of protons.

III.5. Effects of experimental conditions on NMR relaxation parameters

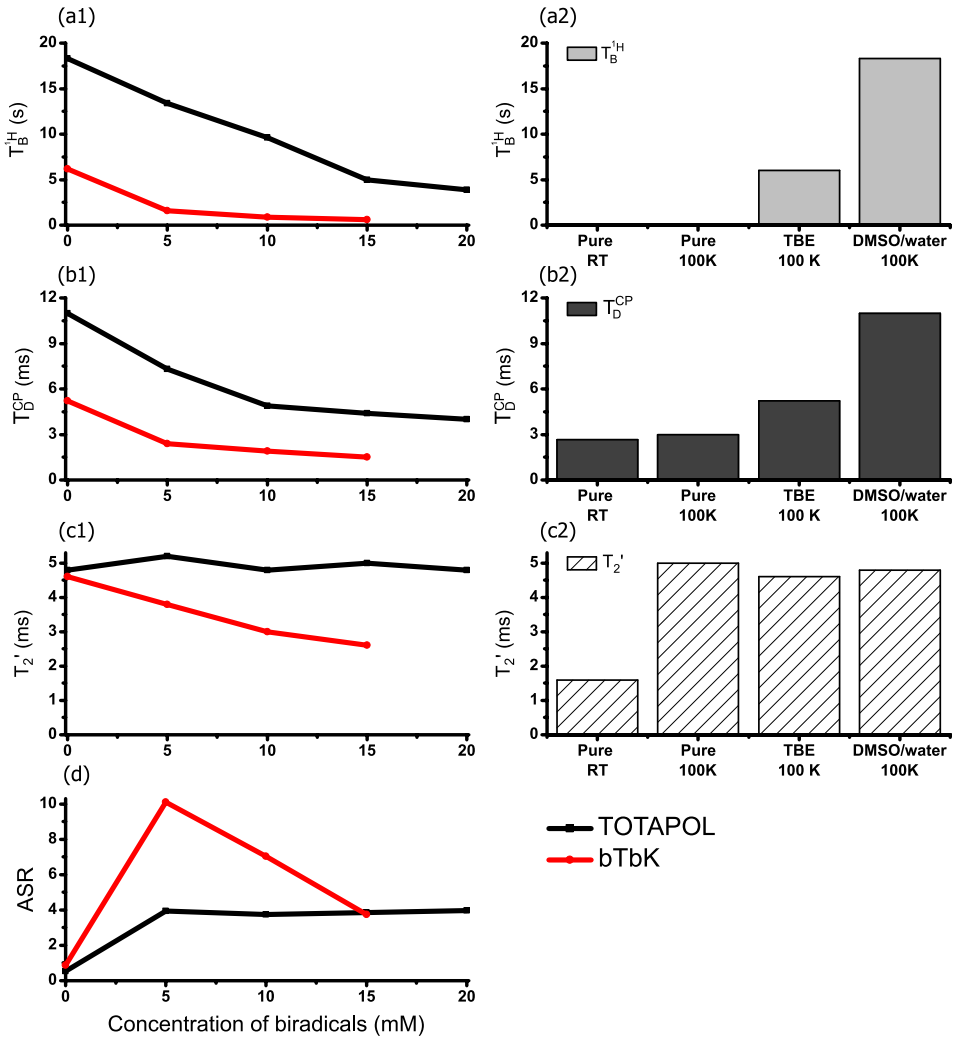

Figure III.4. Variation of (a1,a2) T_B^{1H}, (b1,b2) T_D^{CP}, (c1,c2) $T_2'(^{27}Al)$ and (d) ASR with the experimental conditions. All the data were recorded using an initial CT-CP step, with $\omega_R/(2\pi)$ ~ 14 kHz and at a sample temperature of ~100 K. Variation of (a1) T_B^{1H}, (b1) T_D^{CP}, and (c1) $T_2'(^{27}Al)$ with TOTAPOL concentration (black) in $[^2H_6]$-DMSO/^2H_2O/H_2O and bTbK concentration (red) in TBE. (a2) T_B^{1H}, (b2) T_D^{CP}, and (c2) $T_2'(^{27}Al)$ for pure γ-alumina at room

temperature and at 104 K as well as γ-alumina with a mixture of DMSO and water or with TBE at 104 K. (d) Variation of ASR with (black) TOTAPOL concentration in [$^2H_6$]-DMSO/^2H_2O/H_2O and with (red) bTbK concentration in TBE.

In this section it is discussed how in MAS-DNP experiments the NMR parameters for γ-alumina depend on the experimental conditions, including the type of nitroxide-based radicals (TOTAPOL or bTbK), their concentrations (from 0 to 20 mM), the solvents, and finally the temperature. Figure III.4 shows the variation of T_B^{1H}, T_D^{CP}, and $T_2'(^{27}Al)$ under different experimental conditions. T_B^{1H} is defined as the time constant for *z*-magnetization to return back to its thermal equilibrium value (not necessarily Boltzmann equilibrium[36,37]). This is an important parameter to take into account since most of the experiments are implemented with a recycle delay of ~1.3T_B^{1H} for optimum S/N per unit of square root of time (sensitivity). The measurement of T_B^{1H} was performed indirectly through a saturation recovery experiment using a CT-CP step before signal acquisition. The variation of T_B^{1H} as a function of the concentration of TOTAPOL and bTbK is shown in Figure III.4a1. The values of this parameter decrease as the concentration of the polarizing agents increase. The reduction of T_B^{1H} with increasing concentration of polarizing agent can be attributed to faster hyperpolarization build-up and increased paramagnet-induced relaxation. Furthermore, T_B^{1H} values for TOTAPOL in [$^2H_6$]-DMSO/^2H_2O/H_2O are significantly higher than those of bTbK in TBE. Such difference arises from the characteristics of the solvents rather than from those of the radicals since the T_B^{1H} value of γ-alumina impregnated with just [$^2H_6$]-DMSO/^2H_2O/H_2O is significantly longer than that of γ-alumina impregnated with only TBE.

The other experimental conditions considered are temperature and choice of solvents. As displayed in Figure III.4a2, pure γ-alumina at RT and 100 K provide similar results (T_B^{1H} ~0.3

ms), indicating that for the untreated γ-alumina system, the temperature has negligible effect on T_B^{1H}.

In contrast to temperature, in the absence of radicals, the use of solvent does affect T_B^{1H}, as clearly observed in Figure III.4a2, where γ-alumina was impregnated with either aqueous or organic solvents. The longer T_B^{1H} values for γ-alumina nanoparticles surrounded by frozen solvent may stem from the removal of paramagnetic oxygen in those samples, although thorough freeze-thawing of the samples was performed to limit this effect. T_B^{1H} is larger by a factor of ~3 for the sample impregnated with the mixture of DMSO/water compared to that with TBE.

T_D^{CP} is defined here as the signal decay time constant during a CT-CP step. It can be measured by varying the CP contact time, with the experimental data being analyzed to extract the CP build-up time and signal decay time constant (T_D^{CP}) based on a phenomenological expression[67]. The variation of this parameter as a consequence of experimental conditions is shown in Figure III.4b1 and Figure III.4b2. It is observed that T_D^{CP} presents a similar trend to T_B^{1H}. This similarity could be explained owing to the involvement of ^{1}Hs in both relaxation parameters.

T_2'(^{27}Al) is defined as the time constant for the signal decay during a spin-echo. It can be measured by varying the (rotor-synchronized) delays bracketing a CT-selective π-pulse in a ^{27}Al spin-echo experiment. T_2' is not affected by inhomogeneous interactions such as the chemical shift distribution but is affected by the heteronuclear coupling interaction ^{1}H–^{27}Al, and the hyperfine interaction between unpaired electrons and ^{27}Al nuclei. Since, for our system, sufficient SPINAL64[91] ^{1}H decoupling was used, the effect of ^{1}H–^{27}Al could be neglected.

The variation of T_2'(^{27}Al) as a function of concentration of polarizing agents is given in Figure III.4c1. It is observed that T_2'(^{27}Al) remains rather constant with increased concentration

of TOTAPOL in [$^2H_6$]-DMSO/^2H_2O/H_2O. The slight oscillation could be attributed to experimental uncertainties. Conversely, the T_2'(^{27}Al) value decreases for increasing concentration of bTbK in TBE. The discrepancy in tendency between the two radical solutions stems from the biradicals rather than from the solvents since in the absence of radicals, the aqueous and organic solvents provide a similar value of T_2'. As the hyperfine interaction can affect T_2', the difference in T_2' between TOTAPOL and bTbK solutions could be explained by the fact that bTbK radicals are closer to the surface of γ-alumina on average than TOTAPOL radicals. This conclusion is also verified by the comparison of $\varepsilon_{ON/OFF}$ (^{1}H→^{27}Al) and $\varepsilon_{ON/OFF}$ (^{1}H→^{13}C) for the two radical solutions. For the system doped with TOTAPOL, as $\varepsilon_{ON/OFF}$ (^{1}H→^{27}Al) = $\varepsilon_{ON/OFF}$ (^{1}H→^{13}C) = 14, it means that TOTAPOL molecules are equally distributed in the solvent. In the case of the system impregnated with bTbK, $\varepsilon_{ON/OFF}$ (^{1}H→^{27}Al) = 22 > $\varepsilon_{ON/OFF}$ (^{1}H→^{13}C) = 14 confirms an affinity of bTbK molecules for the surface of γ-alumina. Another interesting point could be derived from the equal enhancement of ^{1}H→^{13}C and ^{1}H→^{27}Al. This result shows that for the γ-alumina system, there are no ^{1}Hs in the bulk. If there were, buried ^{1}H nuclei would be less hyperpolarized since they are more distant from the polarizing agent than the solvent protons and the average enhancement (after CP) of ^{27}Al would be lower than that of ^{13}C. This latter scenario was indeed seen for silica NPs (*see* Section II.9), where it is known that bulk ^{1}Hs can exist.

In the recent work from Takahashi *et al*[103], it was shown that T_2'(^{13}C) of ^{13}C-urea in frozen TOTAPOL solution in [$^2H_6$]-DMSO/^2H_2O/H_2O (60/30/10 v%) decreases from 46 to 2.4 ms as the concentration rises from 0 to 60 mM. The significantly shorter T_2'(^{27}Al) seen for surface nuclei of γ-alumina suggests the involvement of another relaxation mechanism, which is here attributed to the fluctuation of the quadrupolar interaction. Besides the effect of

paramagnetic species, the solvents and temperature alone are also considered. The longer T_2'(^{27}Al) for pure γ-alumina at 100 K than at RT shows that temperature does have an effect onT_2' here. In addition, unlike T_B^{1H} and T_D^{CP}, the added solvents do not affect T_2' since the value remains constant compared to pure γ-alumina at 100 K. Further study on the effects of experimental conditions on the NMR relaxation parameters is discussed below.

Table III.1. Temperature or solvents affecting T_B^{1H}, T_D^{CP}, and T_2'(^{27}Al) of pure γ-alumina.

	Temperature	Solvents
T_B^{1H}; T_D^{CP}	✗	✓
T_2'(^{27}Al)	✓	✗

The dissimilarity between T_B^{1H}, T_D^{CP}, and T_2'(^{27}Al) arises from the involvement of ^{1}Hs for the former two parameters while the later involves ^{27}Al nuclei without the interference of ^{1}Hs.

For T_2'(^{27}Al), as mentioned above, the major relaxation mechanism is probably a fluctuation of the quadrupolar interaction, and at different temperatures the rate of modulation of this will differ, leading to a dependence of T_2'(^{27}Al) on temperature. Regarding the solvents, T_2'(^{27}Al) is not affected because the added solvents do not modify the surface structure or alter the modulation rate of the quadrupolar interaction owing to the protection of surface alumina by layers of physisorbed or chemisorbed water. This is not the situation for T_D^{CP} and T_B^{1H} where ^{1}H nuclei from the added solvents will homogeneously couple to hydroxyls and/or water layers to perturb the proton network. Furthermore, any paramagnetic oxygen will contribute more to the relaxation of protons than to that of ^{27}Al nuclei.

From the above detailed analysis of various experimental conditions on the relaxation parameters, it is obvious that the optimum conditions need to be carefully chosen. As the ASR

considers all the positive and negative effects, this is used as an effective assessment of the most favorable sample preparation. The ASR values of different sample preparations are shown in Figure III.4d.

The ASR values display different tendencies between hydrophilic and hydrophobic sample preparations. For the system doped with TOTAPOL in [$^2H_6$]-DMSO/^2H_2O/H_2O, the ASR increases with the use of polarizing agent (and thus DNP) and remains constant up to the limit of 20 mM tested. This is not the situation for the system impregnated with bTbK in TBE. The ASR is maximum at 5 mM bTbK, and then decreases with increasing concentration of bTbK. It is worth noting that with the use of radicals and DNP, the ASR values are all larger than 1, which means that it is useful to perform MAS-DNP at 100 K. Interestingly, a high ASR of 6.8 (not shown in Figure III.4d) is measured for pure γ-alumina at 100 K. This ASR is due to the low temperature alone and stems from (i) an increase in intrinsic Boltzmann polarization and a reduction in thermal noise as well as (ii) a more efficient CP transfer. Owing to the high ASR, it is more preferable to perform conventional ssNMR at 100 K than DNP-NMR for most of the attempted sample preparations. Nevertheless, the most favorable sample preparation, 5 mM bTbK in TBE, provides the highest ASR of 9.5, corresponding to ~90-fold reduction in acquisition time. Henceforth, further structural characterization experiments are performed on the system doped with 5 mM bTbK in TBE.

III.6. *Primostrato* and *bulk-filtered* techniques

It is known that CP can be a surface-selective technique, with the condition that there are no buried ^{1}Hs in the bulk[67,98]. In this section, the term ‘surface’ is analyzed; namely, for alumina systems, how deep the polarization from ^{1}Hs of hydroxyl groups or water layers could transfer into the bulk of the analyte. SPINEV simulations[87] were performed to help clarify this interest.

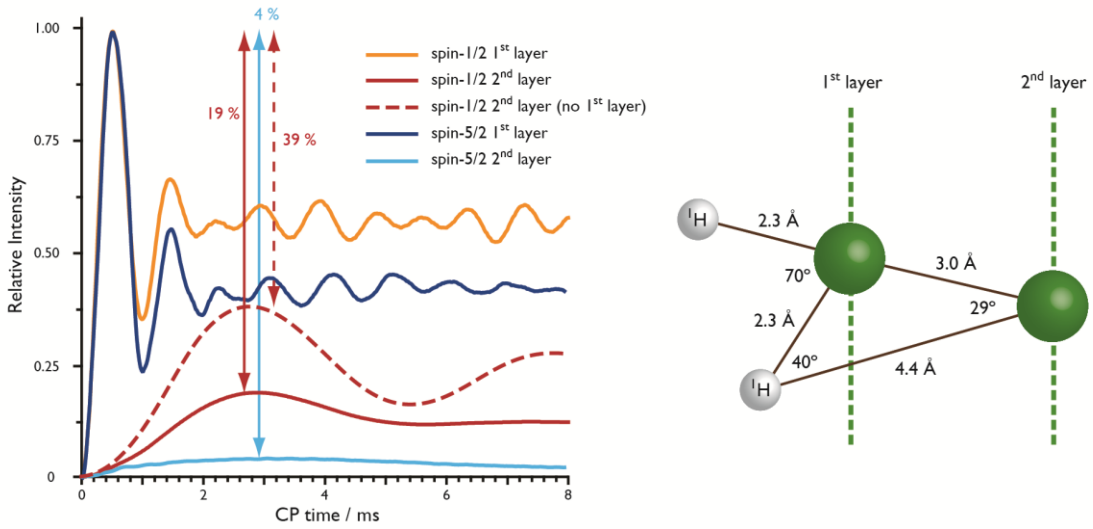

Figure III.5. Simulations of the $^{1}H \rightarrow X$ CP transfer depth profile as a function of CP contact time for the four-spin system, which is shown on the right. The X nuclei could be spin-1/2 or spin-5/2 with a Larmor frequency of 104 MHz at 9.4 T. Further information on the simulation conditions is presented in the main text. Adapted from Ref. 47.

A 4-spin model surface system is defined that consists of two protons and two identical nuclei (X) with spin I. For this system, two cases are taken into account. The first one is I = ½ while the second one is I = 5/2 (^{27}Al). The involvement of spin-1/2 in the simulations aims at examining whether there is difference in the CP transfer depth profile between spin-1/2 and half-integer quadrupolar nuclei. The detailed structure of the model system is depicted in Figure III.5 on the right.

The simulation conditions assume B_0 = 9.4 T, corresponding to a Larmor frequency of 104 MHz for X, and $\omega_R/(2\pi)$ = 8 kHz. For the case of X = 5/2, the quadrupolar interaction is defined by C_Q = 3 MHz, η_Q = 0.25. The set up of the CP matching condition for all simulations is $(I + 1/2).\gamma_X.B_{1X} + \omega_R = \gamma_H.B_{1H}$.

For the sake of clarity, the $^{1}H \rightarrow X$ CP efficiency of the first-layer for both spin-1/2 and spin-5/2 are normalized to 1 and the intensities for the second layer is calculated relative to this.

Simulations for the case of spin-1/2 CP

In the simulations, it is assumed that the spin-1/2 has an identical γ_X with a ^{27}Al nucleus. If the natural abundance of X is 100 %, the second-layer X nucleus will experience the existence of the first-layer nucleus between itself and protons. For this situation, as illustrated in Figure III.5, the optimum CP efficiency for the second-layer X nucleus is 19 % compared to the first-layer. In the other situation when the natural abundance of X is small, the second-layer does not "feel" the occurrence of the first-layer nucleus. Therefore, simulations could be performed as if the first-layer nucleus is NMR silent ($I = 0$). Without the interference of the first-layer nucleus, the CP efficiency increases up to 39 % compared to the first-layer nucleus.

In order to be more realistic with experiments, the T_D^{CP} relaxation parameter needs to be involved, which requires the choice of the real system. One of the systems that is extensively studied and was presented in Chapter II of this thesis is SiO_2.

For a better description of the surface of hydroxylated silica, two important points are considered: (i) the ^{29}Si Larmor frequency (~80 MHz at 9.4 T) and (ii) the natural abundance of ^{29}Si (~5 %). The simulation data (not shown in Figure III.5) demonstrate that the optimum CP efficiency for second-layer ^{29}Si is 28 % at a CP contact time of 3.2 ms, a non-negligible intensity compared to the first-layer. As T_D^{CP} of ^{29}Si nuclei could be of the order of tens of ms[104], such decay times do not significantly change the CP efficiency of the system. From the analysis, it is concluded that $^{1}H \rightarrow ^{29}Si$ CP could transfer to several atomic layers below the surface.

Simulations for the case of ^{27}Al CP

Since the natural abundance of ^{27}Al is 100 %, the second-layer ^{27}Al nucleus always experiences the first-layer ^{27}Al between itself and the protons. It is observed from Figure III.5 that the CP efficiency for the second-layer is more affected by the influence of a first-layer for ^{27}Al than for the spin-1/2 case. The optimum CP efficiency at 3 ms is only 4 %, a transfer efficiency 25-fold lower than that achieved for the first layer. Further analysis is implemented by the use of T_D^{CP} and applying this relaxation parameter into simulations. As mentioned in Section III.5, the best sample preparation is the use of 5 mM bTbK in TBE, and T_D^{CP} is 2.4 ms (Figure III.4b1). The optimum CP contact time given by the simulations when combined with this decay constant is 0.5 ms, consistent with the experimentally measured value of 0.55 ms. This shows the relevance of our model for the study of the real γ-alumina system. The CP efficiency for the second-layer is more severely affected when T_D^{CP} is taken into account, and the efficiency is only 2 % compared to the first layer. These results clearly show that for the γ-alumina system, CP is a first-layer selective or *primostrato* technique.

For studying catalytic materials, surface characterization is desired as the reactive sites reside at the surface and reactions occur in this region. However, the selective observation of the bulk of materials is also desired since this allows structural comparisons between the first-layer and the bulk, leading to a better understanding of the entire material. In the context of this work, a new "*bulk-filtered*" technique will then be detailed.

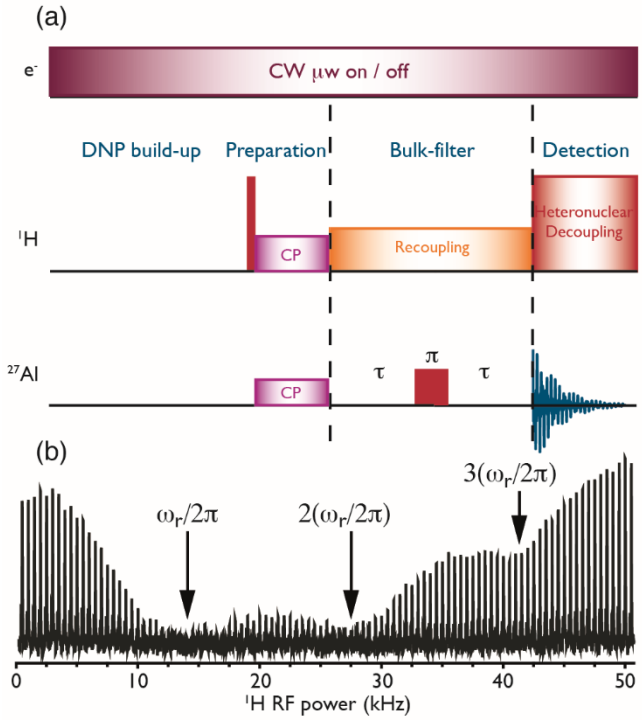

Figure III.6. (a) The pulse sequence used to calibrate the *bulk-filtered* block, which was inserted between the CP block and the detection. (b) The *bulk-filtered* technique was optimized by varying the continuous wave ^{1}H power for a total echo period of ~ 3 ms. Adapted from Ref. 47.

Principles of the bulk-filter

The ^{1}H–^{27}Al heteronuclear dipolar interaction, usually averaged by the MAS, can be reintroduced (recoupled) by applying suitable rf irradiation to ^{1}H nuclei. As ^{1}Hs only reside near the first surface layer ^{27}Al nuclei (*see* Section III. 5), these nuclei are then subject to the ^{1}H–^{27}Al heteronuclear interaction, whereas bulk ^{27}Al nuclei are not. In order to differentiate between the two types of ^{27}Al nuclei, a spin-echo is used during a recoupling period. Since the spin-echo only refocuses the inhomogeneous interactions such as the quadrupolar and chemical shit interaction but not the homogeneous, the transverse magnetization of bulk ^{27}Al nuclei will be mostly refocused while that of surface ^{27}Al nuclei is dephased owing to its heteronuclear dipolar coupling with ^{1}H nuclei. The experimental conditions, such as ^{1}H power and the duration of the

spin-echo, are chosen carefully so that the surface signal intensities are negligible compared to those of the bulk.

Calibration of the bulk-filter

The *bulk-filtered* block is optimized by using the sequence in Figure III.6a. As mentioned in Section III.6, the CT-CP experiment only results in signals from the first surface layer of γ-alumina. Hence, the optimum conditions for the *bulk-filtered* process are identified when the detected signal is minimum.

The ^{1}H recoupling power is optimized using an arbitrary time for the bulk-filtered block (~ 4 ms) so that the detected signal is noticeably reduced. As shown in Figure III.6b, the optimal conditions are found when a rotary resonance recoupling condition[99] is met, i.e. the ^{1}H rf amplitude is equal to $\omega_R/(2\pi)$ or $2.(\omega_R/(2\pi))$. Additional calibration was performed by using the optimum ^{1}H recoupling power but incrementing the *bulk-filtered* delay of $2n.\tau_R$, where n is a positive integer and $\tau_R = (2\pi)/\omega_R$. The *bulk-filter* duration was selected as when the signal intensity is < 10 % of that of the initial ($n = 0$) point.

After the calibration process, the optimized *bulk-filtered* block could be inserted between the last pulse and the detection of an experiment so that the acquired signal is from the bulk ^{27}Al nuclei.

III.7. 1D ^{1}H→^{27}Al CPMAS and *bulk-filtered* DEMAS spectra of γ- and m-alumina

The *primostrato* and the *bulk-filtered* selective techniques were implemented for the structural study of the alumina systems, in particular for the investigation of the differences between the

surface and the bulk of these materials. The 1D spectra acquired by *primostrato* CPMAS and *bulk-filtered* DEMAS of m- and γ-Al_2O_3 are shown in Figure III.7.

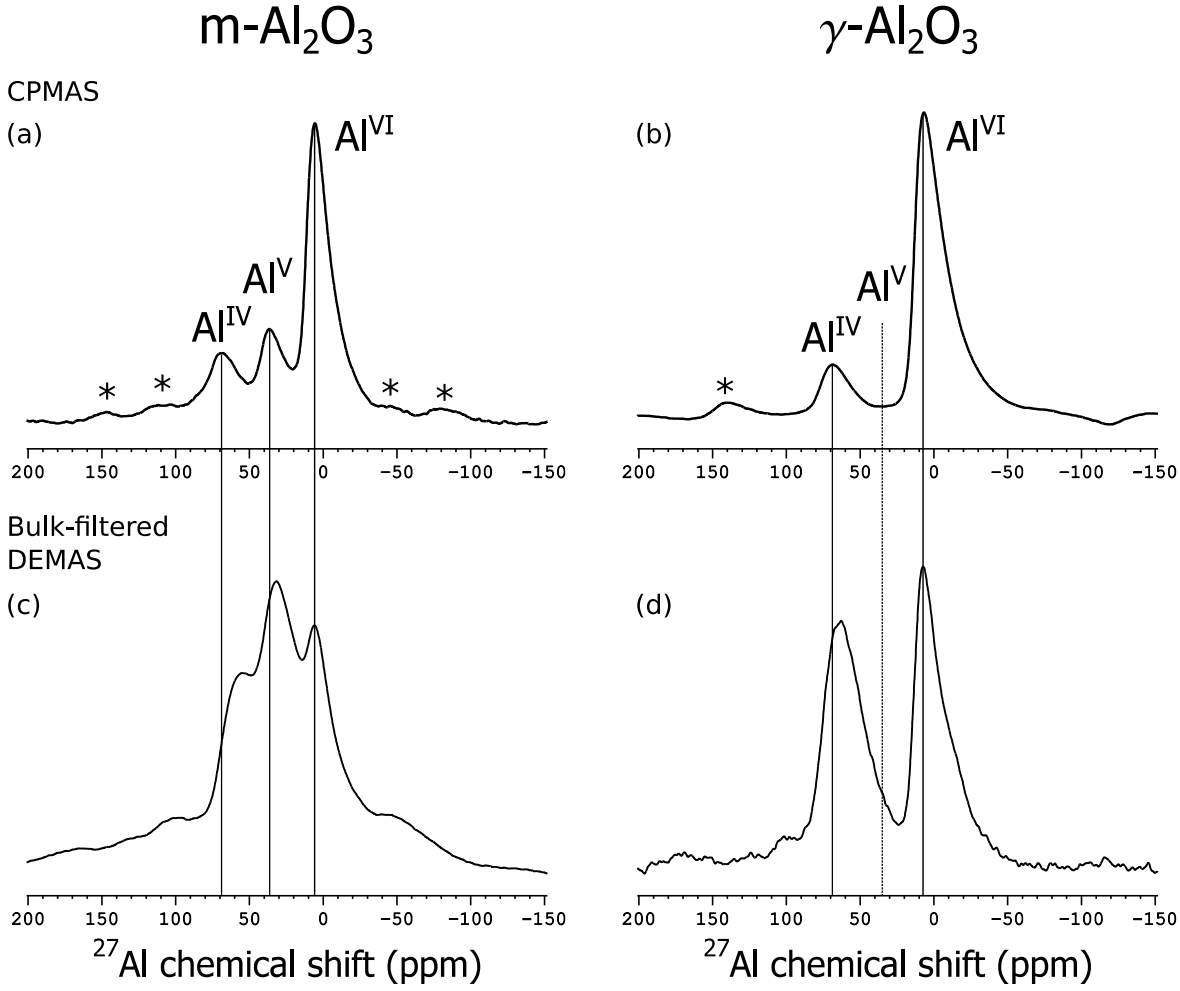

Figure III.7. (a,b) $^1H \rightarrow {}^{27}Al$ CPMAS and (c,d) ^{27}Al DEMAS 1D spectra of (a,c) m-Al_2O_3 impregnated with 20 mM TOTAPOL in [$^2H_6$]-DMSO/^2H_2O/H_2O (78/14/8 wt%) and (b,d) γ-Al_2O_3 impregnated with 10 mM AMUPol in [$^2H_6$]-DMSO/^2H_2O/H_2O (78/14/8 wt%). The spectra were acquired at B_0 = 9.4 T, a temperature of ~100 K, and at $\omega_R/(2\pi)$ = 8 kHz for m-Al_2O_3, and ~14 kHz for γ-Al_2O_3. The asterisks denote spinning sidebands.

For m-Al_2O_3, both the first-layer and the bulk features three peaks, namely four-coordinated Al sites (Al^{IV}) at ~ 70 ppm; penta-coordinated Al sites (Al^{V}) at ~ 35 ppm; and finally

hexa-coordinated Al sites (Al^{VI}) at ~ 10 ppm. What is interesting here is the occurrence of a large amount of Al^{V} sites, which are thought to be the catalytic sites, in the first-layer as well as the bulk. Unlike m-Al_2O_3, the 1D spectra of γ-Al_2O_3 present only the two peaks of Al^{IV} and Al^{VI} sites; no Al^{V} site is observed. It is worth noting that in both cases, while the positions of Al^{IV} sites in the bulk are more shifted to lower chemical shift values than those at the surface, the Al^{VI} sites' positions remains the same. The shift towards lower chemical shift infers a higher C_Q since the induced shift is proportional to the extent of quadrupolar coupling constant. However, it is insufficient to conclude that the bulk consists of sites subject to larger C_Q since the CP efficiency strongly depends on the size of C_Q, while the bulk-filtered spectra are obtained by the use of DEMAS and bulk-filtered block, schemes which are more robust to the strength of the quadrupolar interaction.

For the 1D spectra in Figure III.7, despite the large enhancement gained by DNP, the detection of sites subject to large C_Q is hard owing to the broadening effect. At B_0 = 9.4 T, the acquisition of 1D spectra is unable to answer whether Al^{V} sites exist for γ-alumina and if yes, where they reside. Higher resolution techniques are required for better analysis of the structure of this material.

III.8. High-resolution techniques for alumina systems

III.8.1 Higher external magnetic field

As stated in Section III.2, the second-order quadrupolar interaction is inversely proportional to the external magnetic field; therefore the higher the field, the more reduced this broadening effect. Hence, ^{27}Al spectra were recorded at higher field in order to try to detect Al^{V} sites in γ-alumina. The 1D $^{1}H \rightarrow {}^{27}Al$ CPMAS spectra acquired at 9.4 T and 18.8 T are shown in Figure III.8.

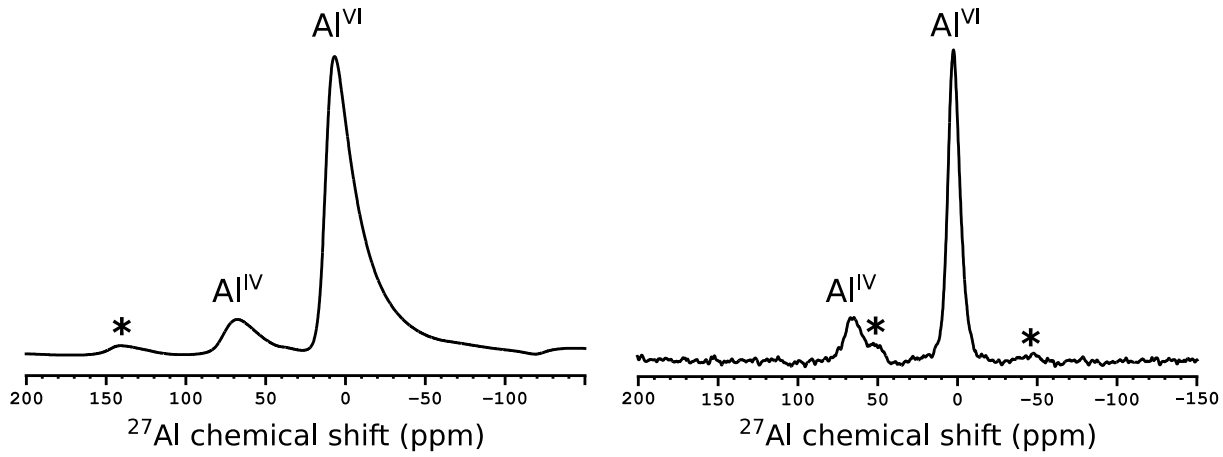

Figure III.8. 1D 1H→^{27}Al CPMAS spectra of γ-alumina impregnated with 10 mM AMUPol in [$^{2}H_6$]-DMSO/$^{2}H_2O$/H_2O (78/14/8 wt%) acquired at 9.4 T and 18.8 T and at low temperature. $\omega_R/(2\pi)$ is ~ 14 kHz and 10 kHz for B_0 = 9.4 T and 18.8 T, respectively. The asterisks denote spinning sidebands.

It is evidently observed that the high-field MAS-DNP experiment gives much better resolution than the corresponding spectrum acquired at lower field. Namely, the linewidths at half maximum of Al^{VI} sites are 2.5 and 2 kHz for 9.4 T and 18.8 T, respectively. However, despite more resolution gained, the 1D high-field CPMAS spectrum failed to prove the existence of Al^{V} at the surface of γ-alumina.

III.8.2 z-filtered 3QMAS experiment

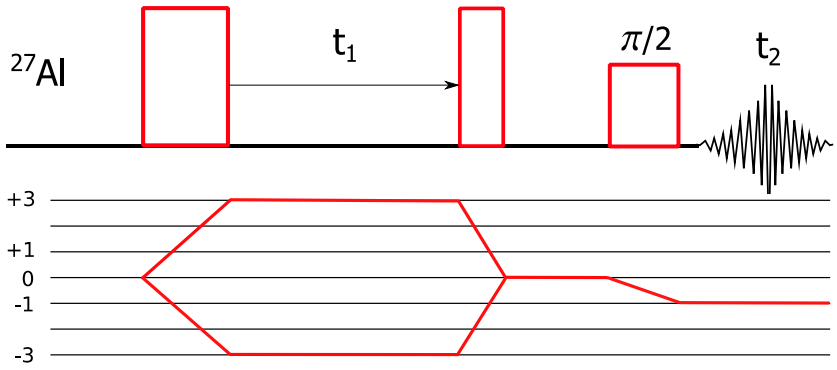

Figure III.9. Pulse sequence and the coherence transfer pathway for the *z*-filtered 3QMAS experiment[101] for half-integer quadrupolar nuclei.

Multiple Quantum Magic Angle Spinning (MQMAS)[100] is a two-dimensional method, which allows the acquisition of high-resolution spectra for half-integer quadrupolar nuclei owing to a refocusing of the second-order quadrupolar interaction. The acquired spectrum is a 2D spectrum in which the isotropic parts of interactions correlate with the conventional MAS-acquired signal. This correlation is achieved by the manipulation of both the spatial and spin parts.

In the context of this work, the focus is on the *z*-filtered Triple Quantum MAS (3QMAS)[101] experiment (*see* Fig III.9). The 3Q coherence is generated by the first (excitation) pulse and then evolves during the t_1 period before being rotated back to the *z*-direction (0Q) by the second (reconversion) pulse. The final pulse is a CT-selective π/2-pulse that converts the longitudinal magnetization into CT 1Q coherences, which are detected during the t_2 period. During t_1 and t_2, the evolution frequencies are proportional to the second-order quadrupolar interaction for 3Q and CT single quantum coherences, respectively. The fourth-rank term of the second-order quadrupolar interaction is refocused for a certain t_2 period, which depends on the t_1

period. For such a t_2 value, an echo occurs. After shearing, isotropic frequencies are observed along the spectral indirect dimension, F_1.

The *z*-filtered 3QMAS sequence is superior to conventional 3QMAS because of the similar efficiencies of both symmetrical pathways, leading to these advantages[101]:

(i) Better elimination of phase distortions produced by dispersive components;

(ii) Less sensitive to the mis-setting of the pulses.

3QMAS data on the first-layer of the alumina system could be obtained by the use of CP-3QMAS, in which the excitation pulse is replaced by a $^{1}H \rightarrow ^{27}Al$ CP block for the direct excitation of 3Q ^{27}Al coherences. The 3QMAS data on the bulk could be acquired by the use of a *bulk-filtered* 3QMAS sequence. This sequence derives from the *z*-filtered 3QMAS but is combined with the *bulk-filter* block, inserted between the CT-selective pulse and the acquisition.

By the use of 5 mM bTbK in TBE, with a resulting ASR ~10, *primostrato* 3QMAS spectra could be recorded in ~ 7 hours. The *bulk-filtered* 3QMAS was also obtained for comparisons between the first-layer and the bulk of γ-alumina. The two corresponding spectra are shown in Figure III.10.

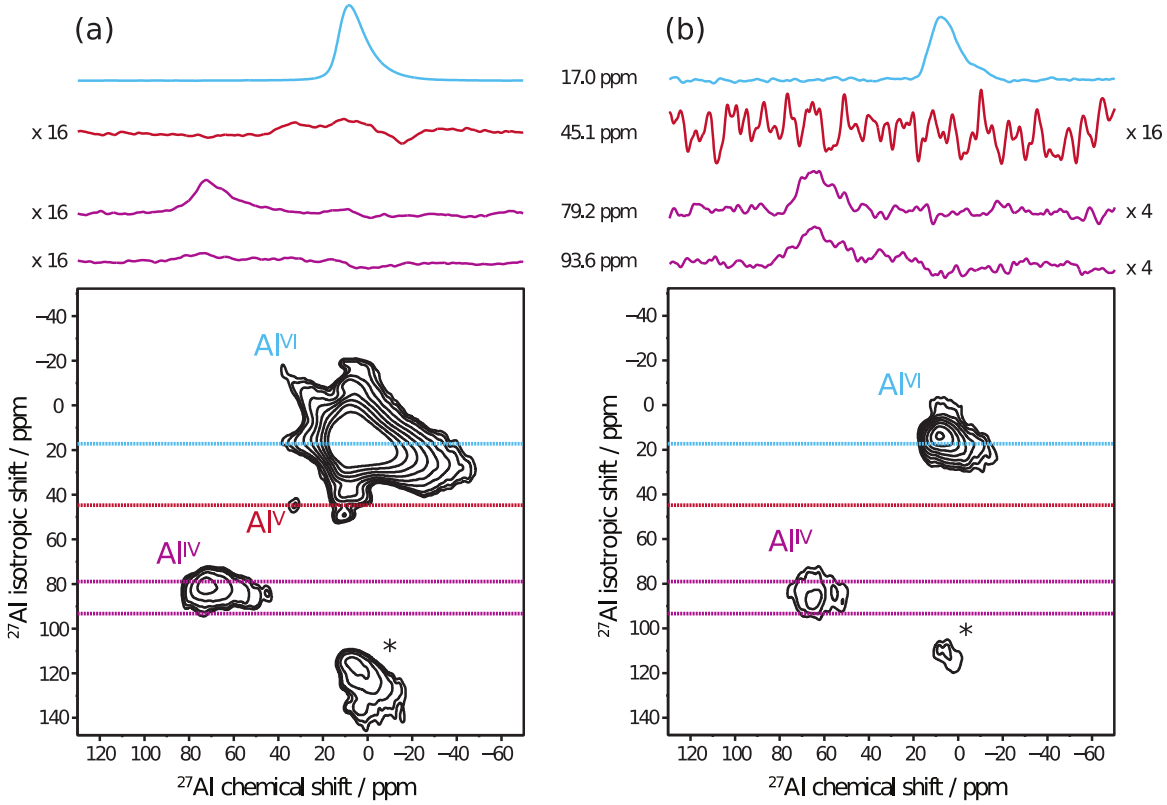

Figure III.10. Sheared (a) DNP-enhanced *primostrato* 3QMAS and *bulk-filtered* 3QMAS spectra of γ-alumina impregnated with 5 mM bTbK in TBE at B_0 = 9.4 T, $\omega_R/(2\pi)$ ~ 14 kHz, and at a temperature of ~100 K. The contour levels used in (a) and (b) are not the same. The 1D spectra shown atop the 2D spectra present extracted cross-sections taken at the given specific isotropic shifts in the F_1 dimension. Asterisks denote spinning sidebands. Adapted from Ref. 47.

Similar to the 1D spectra of γ-alumina shown in Figure III.7, the Al^{IV} and Al^{VI} sites are evident in the 3QMAS spectra of both regions. However, a comparison of the *primostrato* and *bulk-filtered* 3QMAS spectra shows that Al^{V} sites are present and predominantly reside in the first layer of γ-alumina and not in the bulk. This result is confirmed by the comparison of the cross-sections extracted at the isotropic shift of 45 ppm. Al^{V} sites are detected in the cross-

section corresponding to the first layer but was under the detectable limit for the cross-section of the *bulk-filtered* spectrum.

Not only used for the verification of the existence of Al^V sites, the cross-sections could be employed for estimating their quadrupolar parameters. Models were proposed to fit the experimental data[47]. The best fit parameters are C_Q = 7.0 ± 0.3 MHz and η_Q = 0.1 ± 0.1. Other cross-sections could also be extracted at different chemical shifts for Al^{IV} and Al^{VI} sites. It should be noted here that this approach of fitting only provides qualitative estimates of the quadrupolar parameters. For a more reliable extraction, the Czjzek model[105,106] should be used owing to the distribution of parameters $\{C_Q, \eta_Q\}$ for different sites.

III.8.3 $BR2_2^1$ recoupling sequence

Another method to obtain high-resolution information that allows probing the structure of this γ-alumina system is the use of a homonuclear dipolar-mediated recoupling sequence. However, this task is challenging since the target nucleus is ^{27}Al, a quadrupolar nucleus, whose interactions complicate the spin dynamics of recoupling sequences.

As shown in Section III.2, for efficient spin-locking, the nutation frequency of the ^{27}Al CT is required to be small, while avoiding certain resonant conditions. One can choose an efficient nutation frequency that is equal to half of $\omega_R/(2\pi)$, i.e. the HORROR condition[107], explaining the favorable use of HORROR-based homonuclear recoupling sequences for half-integer-spin quadrupolar nuclei. Hitherto, the most efficient recoupling sequence employed for quadrupolar nuclei is $BR2_2^1$[58], and this sequence was used to probe the spatial proximities among the ^{27}Al sites on the surface of γ-alumina. The pulse sequence for $BR2_2^1$ is displayed in Figure III.11. The detailed spin dynamics of this sequence will be analyzed in Chapter IV.

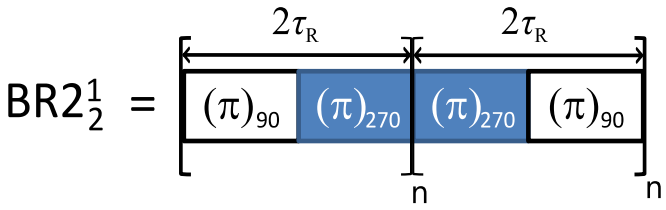

Figure III.11. The BR2$_2^1$ recoupling sequence. This sequence consists of two blocks, R2$_2^1$ and R2$_2^{-1}$, lasting for $2\tau_R$, and the basic pulse for each is π.

The pulse sequence and the coherence pathway for the homonuclear dipolar-mediated correlation experiments were detailed in Section II. 6. As a quadrupolar nucleus has spin $I > ½$, even a single nucleus could create DQ coherences, which could obscure DQ coherences between coupled quadrupolar nuclei. To overcome this, Mali et al.[108] inserted a selective π-pulse between the excitation and the reconversion blocks, and phase cycled to select $\pm$ DQ $\rightarrow \mp$ DQ. The approach permits the selection of only DQ_{CT} between the CTs of two coupled ^{27}Al nuclei while the single nucleus DQ coherences are eliminated.

Figure III.12 shows the homonuclear correlation experiment of γ-alumina impregnated with AMUPol in aqueous solvent. The radical AMUPol was chosen since it provides so far the highest DNP enhancements and overall sensitivity. Owing to the enhancement gained by DNP, the experiment could be recorded in ~7 hours. It is worth noting that the signals obtained from this experiment do not only represent the first-layer sites since the first-layer ^{27}Al nuclei are also coupled to ^{27}Al nuclei in deeper layers.

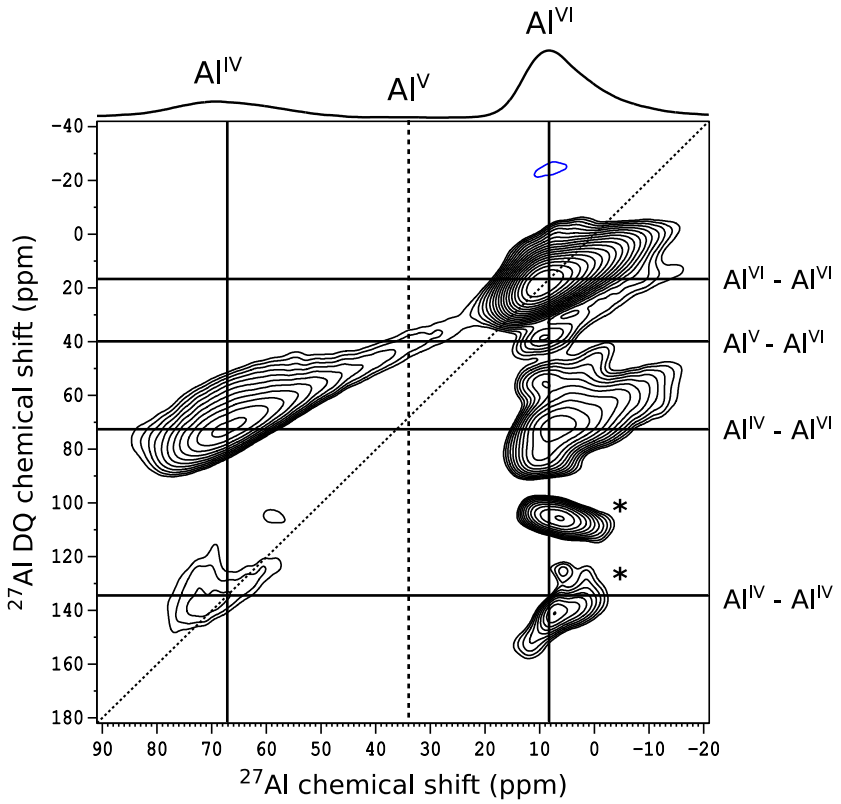

Figure III.12. 2D DQ-SQ homonuclear dipolar-mediated correlation spectrum of γ-alumina impregnated with 10 mM AMUPol in [$^2H_6$]-DMSO/^2H_2O/H_2O (78/14/8 wt%) at B_0 = 9.4 T, $\omega_R/(2\pi)$ ~ 14 kHz, and at a temperature of ~100 K. Atop is displayed the 1D $^1H \rightarrow ^{27}Al$ CPMAS spectrum. The vertical lines highlight the shift of different ^{27}Al sites while the horizontal lines highlight the sum of shifts of correlated ^{27}Al sites. The asterisks denote spinning sidebands or artifacts.

It is shown in Figure III.12 that the Al^V sites are not clearly resolved in the direct dimension (highlighted by the dashed vertical line). However, the horizontal line at ~40 ppm in the indirect dimension F_1, highlights the Al^V-Al^{VI} correlation. Based on this correlation, the shift of Al^V sites are identified at ~35 ppm, which is in full agreement with the shift of Al^V sites extracted from *primostrato*-3QMAS (*see* Figure III.10).

Other correlation peaks were evidently displayed, except Al^{V}–Al^{V} and Al^{IV}–Al^{V} correlations. The absence of these two correlations could be a result of two possibilities: (i) the signal intensities are below the detectable limit or (ii) they do not exist. This is still an open question that requires further investigation and experimental developments, such as pulse sequences, higher external magnetic field, better polarizing agents, or faster $\omega_R/(2\pi)$.

III.9. Conclusion

In this study, both hydrophilic and hydrophobic sample preparations were analyzed not only for the optimized sensitivity but also for the investigation of different experimental conditions on the sample as well as on the NMR relaxation parameters. It was shown that while $T_2'(^{27}Al)$ is independent of the increased concentrations of TOTAPOL, its value decreases for increasing concentrations of bTbK. The latter observation suggests closer proximities of bTbK molecules to the surface of γ-alumina, which results in the higher overall sensitivity observed. Considering all the beneficial as well as the detrimental effects on the NMR parameters, 5 mM bTbK in TBE offered the highest sensitivity. Simulations illustrated that $^{1}H \rightarrow ^{27}Al$ CP is selective to only the first surface layer of alumina systems, yielding *primostrato* NMR. Owing to the optimized MAS-DNP sample preparation, *primostrato* (through CP) MQMAS spectra could be acquired in ~7 hours. This experiment when compared to a *bulk-filtered* version showed that Al^{V} sites reside predominantly in the surface not in the bulk. Another high-resolution technique probing structural information is the 2D homonuclear correlation experiment. This experiment not only corroborated the existence of Al^{V} sites but also provided insights into the location of these sites on the surface of γ-alumina.

Chapter IV THEORY OF $BR2_2^1$

IV.1 Introduction

In the previous chapters, various recoupling sequences were used to probe the homonuclear spatial proximities of ^{29}Si or ^{27}Al local environments. For instance, pC7[82], SR26[83], S_3, and $[S_3]$[84] were used to study ^{29}Si – ^{29}Si correlations (*see* Section II.9) and $BR2_2^1$[58] for ^{27}Al – ^{27}Al correlations (*see* Section III.10). This chapter will focus more on analyzing the recoupling sequences employed for half-integer quadrupolar nuclei, namely $BR2_2^1$, S_3, and $[S_3]$ because:

(i) for efficient spin locking, the rf amplitude is required to be small (*see* section III.2), which well matches the employed rf power of the HORROR-based recoupling sequences;

(ii) S_3 and $[S_3]$ were well designed and are superior to $BR2_2^1$ in terms of robustness to difference of offsets and CSA for spin-1/2[84]. However, it is also desired to compare the transfer efficiency of these aforementioned recoupling sequences on a ^{27}Al – ^{27}Al system;

(iii) for further improvement in studying the spatial proximities (as stated in Section III.10), a thorough understanding of the spin dynamics of these sequences is required, which could potentially lead to the development of novel recoupling sequences.

IV.2 Pulse sequence and notation

IV.2.1 Pulse sequence scheme

The standard notation for rf pulses is used: ξ_θ. This indicates a rectangular, resonant rf pulse with flip angle ξ and phase θ. The angles are written in degrees. The $BR2_2^1$ sequence is shown in Figure IV.1a, which could be written as $(R2_2^1)_n(R2_2^{-1})_n$ in which $R2_2^1$[89] employs a simple $(\pi)_0$-pulse as a basic element and *n* is the number of loops. The rf amplitude equal half of the MAS frequency (= $(\omega_R/(2\pi))/2$) and the duration of one cycle of $BR2_2^1$ is equal to $4\tau_R$.

S_p (p = 3 and 4) sequences, which could be written as $R2_{2p}^{1}R2_{2p}^{-1}$, are displayed in Figure IV.1b, in which the basic composite pulses employed are given below:

$(2\pi)_{180}(3\pi/2)_0(\pi/2)_{180}$ for p = 3,

$(\pi/2)_{180}(2\pi)_0(3\pi/2)_{180}(5\pi/2)_0(3\pi/2)_{180}$ for p = 4,

Further information on these sequences is given in detail elsewhere[84].

These recoupling sequences can be bracketed by two π/2 pulses with ±180° phase shifts with respect to the phase of the sequence and are denoted as [S_p]. The aim of bracketing the S_p sequences is to convert the mixture of ZQ and DQ terms into a pure DQ term, leading to two times faster transfer build-up time[84]. These bracketed versions of the sequences are depicted in Figure IV.1c.

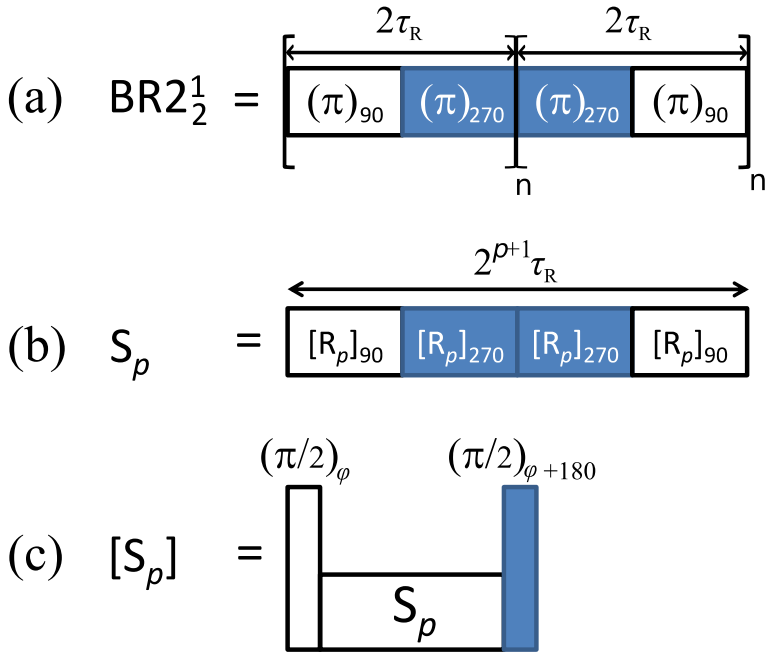

Figure IV.1. The pulse scheme of (a) $BR2_2^1$, (b) S_p (p = 3 or 4), and (c) bracketed versions of S_p

IV.2.2 Notation

For an easier description of the theory of $BR2_2^1$, new DQ and ZQ terms are introduced, based on the permutation rules for X, Y, and Z in the Cartesian frame:

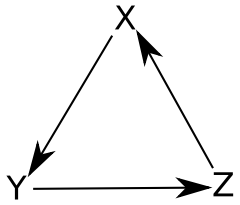

Owing to this rule, it is possible to derive DQ and ZQ terms on different axes instead of the longitudinal *z*-axis. The results are listed in Table IV.1.

Table IV.1. Spin operator definitions for DQ and ZQ terms on different axes

z-direction		*y*-direction		*x*-direction	
DQ_x	$2I_{1x}I_{2x} - 2I_{1y}I_{2y}$	DQ_z	$2I_{1z}I_{2z} - 2I_{1x}I_{2x}$	DQ_y	$2I_{1y}I_{2y} - 2I_{1z}I_{2z}$
DQ_y	$2I_{1x}I_{2y} + 2I_{1y}I_{2x}$	DQ_x	$2I_{1z}I_{2x} + 2I_{1x}I_{2z}$	DQ_z	$2I_{1y}I_{2z} + 2I_{1z}I_{2y}$
ZQ_x	$2I_{1x}I_{2x} + 2I_{1y}I_{2y}$	ZQ_z	$2I_{1z}I_{2z} + 2I_{1x}I_{2x}$	ZQ_y	$2I_{1y}I_{2y} + 2I_{1z}I_{2z}$
ZQ_y	$2I_{1y}I_{2x} - 2I_{1x}I_{2y}$	ZQ_x	$2I_{1x}I_{2z} - 2I_{1z}I_{2x}$	ZQ_z	$2I_{1z}I_{2y} - 2I_{1y}I_{2z}$

$DQ_x^{(z)}$ means DQ x-coherence with respect to using the the *z*-direction as the longitudinal axis. To verify this notation, the cyclic commutation and the evolution under chemical shift were proved (see the Appendix).

$$[\tfrac{I_{1x}+I_{2x}}{2}, DQ_y^{(x)}] = \mathrm{i}DQ_z^{(x)} \quad \text{(IV.1)}$$

$$[\tfrac{I_{1y}-I_{2y}}{2}, ZQ_z^{(y)}] = \mathrm{i}ZQ_x^{(y)} \quad \text{(IV.2)}$$

$$DQ_y^{(x)} \xrightarrow{\Omega_{I_1} I_{1x} + \Omega_{I_2} I_{2x}} DQ_y^{(x)}\cos(\Omega_{I_1} + \Omega_{I_2})\mathrm{t} + DQ_z^{(x)}\sin(\Omega_{I_1} + \Omega_{I_2})\mathrm{t} \quad \text{(IV.3)}$$

As the newly derived DQ and ZQ terms comply with the cyclic permutation and chemical shift evolution conditions, the proposed DQ and ZQ terms in different axes are valid.

IV.3 Theory and Simulations

IV.3.1 Theory

Initially, a spin system is considered as an isolated pair of spin-1/2 nuclei with negligible CSA. In that case, the spin Hamiltonian only contains terms relative to the homonuclear dipolar coupling, the offsets, and the rf pulses. The Hamiltonian in the usual rotating frame during the R2$_2^1$ sequence is:

$$\widehat{H} = \begin{cases} \sum_{n=\pm1,\pm2} \sqrt{6}.\omega_D^{(n)}.e^{in\omega_R t}.(3I_{1z}I_{2z} - I_1I_2) + \omega_{I_1}.I_{1z} + \omega_{I_2}.I_{2z} + \omega_1.(I_{1y} + I_{2y}) & if\ 0 < t < \tau_R \\ \sum_{n=\pm1,\pm2} \sqrt{6}.\omega_D^{(n)}.e^{in\omega_R t}.(3I_{1z}I_{2z} - I_1I_2) + \omega_{I_1}.I_{1z} + \omega_{I_2}.I_{2z} - \omega_1.(I_{1y} + I_{2y}) & if\ \tau_R < t < 2\tau_R \end{cases}, \quad \text{(IV.4)}$$

where:

$$\omega_D^{\pm1} = \frac{1}{2\sqrt{2}} b_{IS} sin2\beta_{PR} e^{\pm i\gamma_{PR}} \quad \text{(IV.5a)}$$

$$\omega_D^{\pm2} = -\frac{1}{4} b_{IS} sin^2\beta_{PR} e^{\pm 2i\gamma_{PR}} \quad \text{(IV.5b)}$$

In the above equations, ω_F and ω_1 denote the offset of nucleus F ($F = I_1$ or I_2) and the rf nutation frequency (in rad.s^{-1}), respectively. The Hamiltonian for the R2$_2^{-1}$ sequence can be written using a similar approach. In fact, the terms of the Hamiltonian for $\tau_R < t < 2\tau_R$ become the terms during $0 < t < \tau_R$ for the R2$_2^1$ sequence, and vice versa.

Average Hamiltonian theory (AHT)[109] is applicable if these two conditions are met:

- Cyclicity
- Periodicity

(i) The condition of cyclicity is met when:

$$U_{RF}(2\tau_R) = U_{RF}(\tau_R, 2\tau_R).U_{RF}(0, \tau_R) = 1, \quad \text{(IV.6)}$$

where $U_{RF}(\tau)$, the evolution operator induced by an rf field, is defined as:

$$U_{RF}(t_a, t_b) = e^{-i\int_{ta}^{tb} \hat{H}_{RF} dt} \quad \text{(IV.7a)}$$

From Figure IV.1a, it is known that:

$$U_{RF}(0, \tau_R) = exp(-i.\pi) \quad \text{(IV.7b)}$$

$$U_{RF}(\tau_R, 2\tau_R) = exp(+i.\pi) \quad \text{(IV.7c)}$$

Hence, $U_{RF}(2\tau_R) = 1$

(ii) The condition of periodicity is met when:

$$\widehat{H}(2\tau_R + t) = \widehat{H}(t) \quad \text{(IV.8)}$$

As shown in Eqn. IV.4, the coefficients of the isotropic terms and the rf terms are time-independent; hence their Hamiltonians are periodic. In contrast to these two terms, the homonuclear dipolar coupling term consists of a time-dependent coefficient, $e^{in\omega_R t}$. However, as $e^{in\omega_R(2\tau_R+t)} = e^{in\omega_R t}.\, e^{in.4\pi} = e^{in\omega_R t}$, the Hamiltonian for the homonuclear dipolar coupling is also periodic.

Therefore, AHT could be employed for studying $R2_2^1$ as well as $R2_2^{-1}$. To facilitate the calculations, the Hamiltonians in the rotating frame are transformed to the "rf frame" by these transforming operators

$$U_{RF}(t) = \begin{cases} e^{\left(-i.\omega_1 t.(I_{1y} + I_{2y})\right)} & 0 < t < \tau_R \\ e^{\left(-i.\pi + i.\omega_1 t.(I_{1y} + I_{2y})\right)} & \tau_R < t < 2\tau_R \end{cases} \quad \text{(IV.9)}$$

In the rf frame, the Hamiltonian becomes:

$$\widetilde{H}(t) = U_{RF}(t).\widehat{H}(t).U_{RF}^{-1}(t) \quad \text{(IV.10)}$$

Then the averaged Hamiltonian in the 'rf frame' could be calculated as:

$$\overline{H}^{(1)} = \frac{1}{2\tau_R}.\int_0^{2\tau_R} \widetilde{H}(t)\, dt \quad \text{(IV.11)}$$

III.3.1.a First-order homonuclear dipolar coupling terms

For both $R2_2^1$ and $R2_2^{-1}$, the results are:

$$\bar{H}_{12}^{(1)} = b_{12} f_{12}(\beta_{PR}^{12}, \gamma_{PR}^{12})\{4I_{1z}I_{2z} - (I_1^+ I_2^+ + I_1^- I_2^- + I_1^+ I_2^- + I_1^- I_2^+)\}, \quad \text{(IV.12)}$$

where:

$f_{12}(\beta_{PR}^{12}, \gamma_{PR}^{12}) = \frac{3}{16\sqrt{2}} \sin(2\beta_{PR}^{12}) \cos(\gamma_{PR}^{12})$ and b_{12} is the dipolar coupling constant. β_{PR}^{12} and γ_{PR}^{12} are the Euler angles relating the Principal Axis Frame and the MAS frame.

Eqn. IV.12 shows that the $\bar{H}_{12}^{(1)}$ Hamiltonian contains both the DQ term ($I_1^+ I_2^+ + I_1^- I_2^-$), ZQ term ($I_1^+ I_2^- + I_1^- I_2^+$) with similar coefficients, and the $I_{1z}I_{2z}$ term. The Hamiltonian of Eqn. IV.12 could also be expressed as:

$$\bar{H}_{12}^{(1)} = 2b_{12} f_{12}(\beta_{PR}^{12}, \gamma_{PR}^{12})\{2I_{1z}I_{2z} - 2I_{1x}I_{2x}\} \quad \text{(IV.13)}$$

III.3.1.b First-order isotropic chemical shift terms

For $R2_2^1$ $$\bar{H}_{\omega_F}^{(1)} = \frac{2}{\pi}\omega_F F_x \quad \text{(IV.14a)}$$

and $R2_2^{-1}$ $$\bar{H}_{\omega_F}^{(1)} = -\frac{2}{\pi}\omega_F F_x \quad \text{(IV.14b)}$$

where $F = I_1$ or I_2.

It is noted that the isotropic chemical shift Hamiltonians for $R2_2^1$ and $R2_2^{-1}$ have the opposite sign.

III.3.1.c First-order terms for $BR2_2^1$

As the sequence of $BR2_2^1$ consists of $R2_2^1$ lasting for $2n\tau_R$ then $R2_2^{-1}$ lasting for $2n\tau_R$, the first-order terms of $BR2_2^1$ is the mean average of the corresponding terms of $R2_2^1$ and $R2_2^{-1}$:

$$\bar{H}_{12}^{(1)}(BR2_2^1) = 2b_{12} f_{12}(\beta_{PR}^{12}, \gamma_{PR}^{12})\{2I_{1z}I_{2z} - 2I_{1x}I_{2x}\} \quad \text{(from Eqn. IV.13)} \quad \text{(IV.15)}$$

$$\bar{H}_{\omega_F}^{(1)}(BR2_2^1) = 0 \quad \text{(from Eqn. IV.14a, IV.14b)} \quad \text{(IV.16)}$$

If $BR2_2^1$ only contains the first-order terms, namely the term expressed in Eqn. IV.15, the spin dynamics of this sequence will be identical with that of S_3 or $[S_3]$[84]. However, this is not the case for spin-1/2[84], which suggests the involvement of other terms.

III.3.1.d First-order terms for $BR2_2^1$ in the "offset frame"

For further understanding, the "rf frame" is converted to the "offset frame", where the effect of the offset is considered to remain intact. The propagator for transformation is presented below.

$$U_{offset}(t) = \begin{cases} e^{\left(-i\Delta t.(I_{1x} - I_{2x})\right)}.e^{(-i\Sigma t.(I_{1x} + I_{2x}))} & 0 < t < 2n\tau_R \\ e^{\left(-i\Delta(2n\tau_R - t).(I_{1x} - I_{2x})\right)}.e^{(-i\Sigma(2n\tau_R - t).(I_{1x} + I_{2x}))} & 2n\tau_R < t < 4n\tau_R \end{cases} \quad \text{(IV.17)}$$

where:

$\Delta = (2/\pi).(\omega_{I_1} - \omega_{I_2})$, and $\Sigma = (2/\pi).(\omega_{I_1} + \omega_{I_2})$,

and n is the number of loops of the $BR2_2^1$ sequence (as shown in Figure IV.1a).

Due to $U_{offset} = U_{offset}(2n\tau_R, 4n\tau_R).U_{offset}(0,2n\tau_R) = 1$, the Magnus expansion[110] is applicable. Under these operators, the first-order homonuclear dipolar coupling in the offset frame is given as:

$$\widetilde{H}_{12}^{(1)}(t) = U_{offset}(t).\bar{H}_{12}^{(1)}.U_{offset}^{-1}(t) \quad \text{(IV.18)}$$

and then the average Hamiltonian in the offset frame is calculated based on:

$$\bar{H}_{12}^{(1)}(\text{offset frame}) = \frac{1}{2n\tau_R}\int_0^{2n\tau_R} \widetilde{H}_{12}^{(1)}(t)dt \quad \text{(IV.19)}$$

From Eqn. IV.19, the final result is obtained:

$$\bar{H}_{offset\ frame} =$$
$$b_{12}f_{12}(\beta_{PR}^{12}, \gamma_{PR}^{12}).[ZQ_y^{(x)}.\text{sinc}(\Delta.2n\tau_R) - DQ_y^{(x)}.\text{sinc}(\Sigma.2n\tau_R) - 4I_{1x}I_{2x}] \quad \text{(IV.20)}$$

The Hamiltonian in Eqn. IV.20 could also be expressed as:

$$\bar{H}_{offset\ frame} = b_{12} f_{12}(\beta_{PR}^{12}, \gamma_{PR}^{12}).DQ_x^{(z)}.[1 + 1/2[\mathrm{sinc}(\Delta.2n\tau_R) - \mathrm{sinc}(\Sigma.2n\tau_R)]] \quad \text{(IV.21)}$$

IV.3.2 Simulations

Simulations were performed using SPINEV software[87]. The aim of these simulations was to verify the validity of the analytical expression for the effective Hamiltonian of $BR2_2^1$.

The simulations were performed using B_0 = 9.4 T. The transfer efficiency is defined as the ratio of the detected magnetization of I_{2i} (i = x, y, z) to the initial magnetization of I_{1i}. DQ coherence alone is selected in between the excitation and reconversion blocks. The powder averaging was performed as described in Section II.8. If a single crystal is used, the angles $\{\alpha_{PR}; \beta_{PR}; \gamma_{PR}\}$ are set equal to $\{90^o; 60^o; 30^o\}$, respectively.

For spin-1/2 isotopes, the model system consists of two ^{13}C nuclei, whose internuclear distance is 1.54 Å, corresponding to a dipolar coupling constant of –2 kHz. For simplicity, the CSA values are set to 0 kHz. The isotropic chemical shift values are varied. The MAS frequency is 66 kHz. The recoupling sequence used is $BR2_2^1$, with an rf amplitude of 33 kHz.

MATLAB calculations for this spin-1/2 system were performed using the Hamiltonians derived in the "rf frame" and the "offset frame". The obtained "offset profile", the transfer efficiency with respect to a given offset, is then be compared to SPINEV results in order to check whether the first-order terms are sufficient to describe the spin dynamics during the $BR2_2^1$ recoupling.

For quadrupolar nuclei, the system consists of two ^{27}Al nuclei, whose internuclear distance is 3 Å, corresponding to a dipolar coupling constant of –0.3 kHz. Besides the homonuclear dipolar coupling, ^{27}Al nuclei are also subject to the quadrupolar coupling, characterized by C_Q = 3 MHz and η_Q = 0.25. CSA values are 0 kHz while the isotropic chemical

shift values are varied. The MAS frequency is 20 kHz. Different recoupling sequences such as $BR2_2^1$, S_3, and $[S_3]$ were simulated.

IV.3.2.a Verifications of the first-order AHT term of $BR2_2^1$

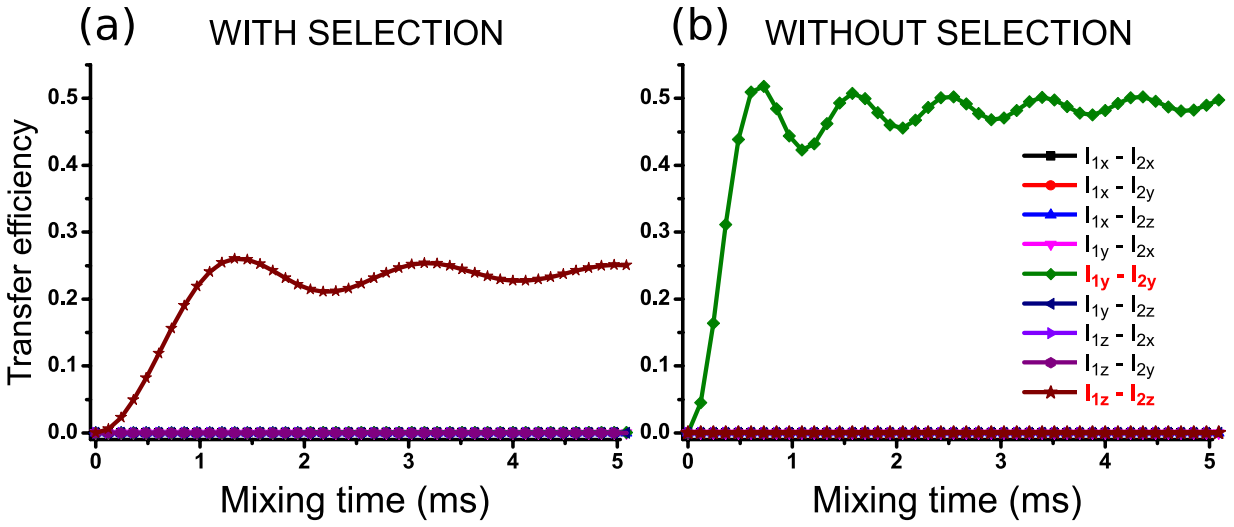

Figure IV.2. Simulated homonuclear polarization transfer using $BR2_2^1$ recoupling for an isolated pair of ^{13}C nuclei with (a) and without (b) DQ selection (filtering). The starting operator is I_{1i} (i = x, y, z) and the detecting operator is I_{2i} (i = x, y, z).

In these simulations, the isotropic chemical shifts and offset are set to 0. Hence the only existing Hamiltonian term is the homonuclear dipolar coupling. To validate Eqn. IV.13, simulations were performed using different starting and detecting operators.

Figure IV.2a shows the situation when DQ filtering (this means +/-2 coherences are selected while other coherences are removed) is performed. It is observed that only by starting with I_{1z} and detecting at I_{2z}, is polarization transferred. The maximum DQ efficiency is approximately 25% and the optimum mixing time is 1.3 ms.

Figure IV.2b shows the situation when DQ filtering is not performed, which means all the coherences are allowed to evolve, and the result obtained is very different. Only starting at I_{1y}

and detecting at I_{2y}, is polarization transferred. It is worth noting that the transfer is two times larger in magnitude and two times faster in build-up rate. It is explained below how these simulations confirm the validity of Eqn. IV.13.

The first-order Hamiltonian term of the homonuclear dipolar coupling is proportional to:

- $2I_{1z}I_{2z} - 2I_{1x}I_{2x} = \boldsymbol{DQ_z^{(y)}}$; or (IV.22a)
- $2I_{1z}I_{2z} - [(2I_{1x}I_{2x} - 2I_{1y}I_{2y}) + (2I_{1x}I_{2x} + 2I_{1y}I_{2y})]/2 = 2I_{1z}I_{2z} - \boldsymbol{DQ_x^{(z)}/2} - ZQ_x^{(z)}/2.$ (IV.22b)

If only the DQ coherences are retained in between the excitation and reconversion blocks (experimentally performed through specific phase cycling), it is shown below that (i) the only relevant term in Eqn. IV.22b is $DQ_x^{(z)}$ and (ii) this term converts the I_{1z} operator into I_{2z}. The starting operator I_{1z} can be written as: $I_{1z} = \frac{I_{1z}+I_{2z}}{2} + \frac{I_{1z}-I_{2z}}{2}$. Both the sum and the difference of I_{1z} and I_{2z} commute with $I_{1z}I_{2z}$. Furthermore, according to the commutation rules in Table IV.1, $I_{1z} + I_{2z}$ does not commute with the $DQ_x^{(z)}$ term but does with $ZQ_x^{(z)}$. The opposite holds for $I_{1z} - I_{2z}$. Therefore, during the $BR2_2^1$ excitation block, the $(I_{1z}+I_{2z})/2$ operator evolves as

$$\left(\frac{I_{1z}+I_{2z}}{2}\right) \xrightarrow{b_{12}f_{12}(\beta_{PR}^{12},\gamma_{PR}^{12})DQ_x^{(z)}} \left(\frac{I_{1z}+I_{2z}}{2}\right)\cos\left(b_{12}f_{12}(\beta_{PR}^{12},\gamma_{PR}^{12})\right) - \left(DQ_y^{(z)}\right)\sin\left(b_{12}f_{12}(\beta_{PR}^{12},\gamma_{PR}^{12})\right), \quad \text{(IV.23a)}$$

whereas the $(I_{1z}-I_{2z})/2$ operator evolves as

$$\left(\frac{I_{1z}-I_{2z}}{2}\right) \xrightarrow{b_{12}f_{12}(\beta_{PR}^{12},\gamma_{PR}^{12})ZQ_x^{(z)}} \left(\frac{I_{1z}-I_{2z}}{2}\right)\cos\left(b_{12}f_{12}(\beta_{PR}^{12},\gamma_{PR}^{12})\right) - \left(ZQ_y^{(z)}\right)\sin\left(b_{12}f_{12}(\beta_{PR}^{12},\gamma_{PR}^{12})\right), \quad \text{(IV.23b)}$$

The selection of DQ coherences will only retain the term proportional to $DQ_y^{(z)}$. This term evolves during the $BR2_2^1$ reconversion block as

$$-\left(DQ_y^{(z)}\right) \xrightarrow{b_{12}f_{12}(\beta_{PR}^{12},\gamma_{PR}^{12})DQ_x^{(z)}} -\left(DQ_y^{(z)}\right)\cos\left(b_{12}f_{12}(\beta_{PR}^{12},\gamma_{PR}^{12})\right) - \left(\frac{I_{1z}+I_{2z}}{2}\right)\sin\left(b_{12}f_{12}(\beta_{PR}^{12},\gamma_{PR}^{12})\right) \quad \text{(IV.23c)}$$

The above equation shows that I_{1z} is partly converted into I_{2z} by two successive $BR2_2^1$ recoupling schemes with a DQ selection during the infinitesimal period separating these

schemes. Therefore, the analytical calculation of Eqn. IV.23 agrees with the simulations displayed in Figure IV.2a. In a real experiment, a final π/2 pulse converts $(I_{1z} + I_{2z})/2$ into $(I_{1x} + I_{2x})/2$, which can be detected. Hence, the NMR signal is proportional to $\sin^2\left(b_{12} f_{12}(\beta_{PR}^{12}, \gamma_{PR}^{12})\right)$.

If no DQ selection is performed it is more convenient to use Eqn. IV.22a to calculate the evolution of the density matrix during the pulse sequence. As $DQ_z^{(y)} = R_x(\pi/2)\left[-DQ_x^{(z)}\right] R_x(-\pi/2)$ where $R_x(\pm\pi/2)$ are the rotation operators performing a rotation through ±π/2 about the *x*-axis, the evolution of the density matrix during $BR2_2^1$ recoupling without DQ selection is similar to that calculated above but the frame is tilted by π/2 about the *x*-axis. Hence, it is the I_{1y} operator that is converted into I_{2y} by $BR2_2^1$ when there is no DQ selection. Furthermore, the scaling factor of $DQ_z^{(y)}$ is two times larger than that of $DQ_x^{(z)}$, which results in two times faster in transfer build-up. Additionally, the DQ selection leads to the reduction of the intensity of the observable signal by a factor of two since the terms produced by the evolution under $ZQ_x^{(z)}$ are eliminated.

IV.3.2.b Verification of the homonuclear dipolar coupling in the "offset frame"

If the derived Hamiltonian in the offset frame is correct, the predicted results obtained from this should be in agreement with simulations. It is worth noting that:

$$sinc(x) = \frac{\sin(x)}{x} = \begin{cases} 1 \; if \; x = 0 \\ \sim 0 \; if \; |x| \gg 0 \end{cases} \quad \text{(IV.24)}$$

Three cases with different chemical shifts are proposed, namely:

When $\Omega_{I_1} = \Omega_{I_2}$ = 10 kHz, this means that Δ = 0 kHz, while Σ = 20 kHz. Applying these values to Eqn. IV.21, it corresponds to $\overline{H}_{offset\ frame} = b_{12} f_{12}(\beta_{PR}^{12}, \gamma_{PR}^{12}).\, 1.5 DQ_x^{(z)}$.

When $\Omega_{I_1} = -\Omega_{I_2} = 10$ kHz, this means that $\Delta = 20$ kHz, while $\Sigma = 0$ kHz. Applying these values to Eqn. IV.21, it corresponds to $\bar{H}_{offset\ frame} = b_{12} f_{12}(\beta_{PR}^{12}, \gamma_{PR}^{12}).0.5 D Q_x^{(z)}$

When $\Omega_{I_1} = 0$ kHz and $\Omega_{I_2} = 10$ kHz, this means that $\Delta = \Sigma = 10$ kHz. Applying these values to Eqn. IV.21, it corresponds to $\bar{H}_{offset\ frame} = b_{12} f_{12}(\beta_{PR}^{12}, \gamma_{PR}^{12}).D Q_x^{(z)}$

Based on the aforementioned Hamiltonians in the offset frame, the transfer build-up from the first case is the fastest, 3 times faster than the second case and 1.5 times faster than the third. Simulations were performed to verify these results.

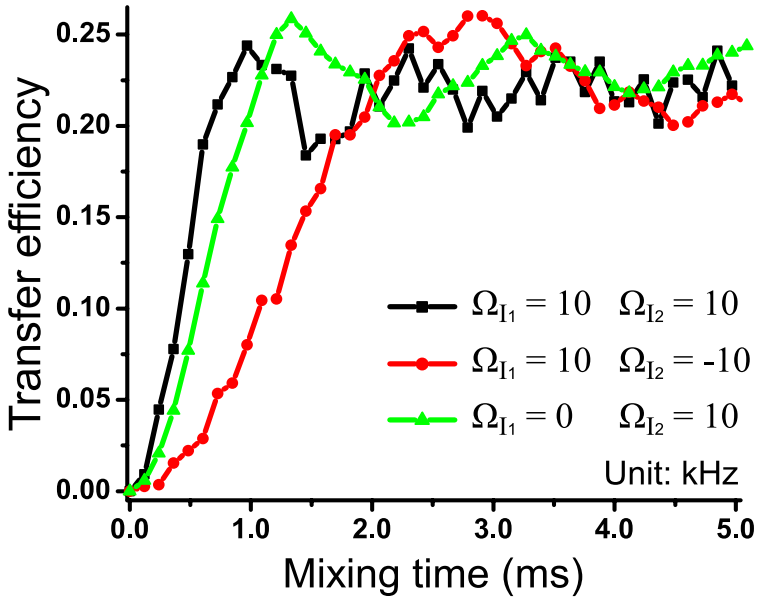

Figure IV.3. Simulated homonuclear polarization transfer using $BR2_2^1$ recoupling for a ^{13}C-^{13}C system with different values of isotropic chemical shifts.

The optimum mixing time for the three cases mentioned are 1.0; 2.9; and 1.3 ms for the first, second, and third assumption, respectively, which is in good agreement with our analysis. This further claims the correctness of the derived Hamiltonians.

Additionally, Eqn. IV.21 and Figure IV.3 enable the explanation for the dip in efficiency observed when irradiating in the center of two resonances from spin-1/2 nuclei with differing

chemical shifts[84]. If the carrier frequency is set in the middle of two distinct chemical shifts ($\Delta \neq 0$), then $\Sigma = 0$, and hence sinc(Σ.2nτ_R) = 1 and $\bar{H} \sim 0.5DQ_x^{(z)}$. The transfer takes longer to build up to maximum efficiency. When the chemical shifts are varied, giving offsets (ν_{offset}), which makes the carrier frequency be shifted away from the middle position, then $\Sigma \neq 0$, and hence the coefficient sinc(Σ.2nτ_R) ~ 0, so $\bar{H} \sim DQ_x^{(z)}$, resulting in faster transfer. The same fast rate of transfer is observed for on-resonance (zero offset) irradiation of an autocorrelation cross-peak (i.e., Σ = 0 kHz and Δ = 0 kHz). For the fastest transfer, Δ = 0 kHz, while $\Sigma \neq 0$ kHz, which represents the case of off-resonance irradiation of an auto-correlation cross-peak. Although the transfer efficiencies for the three scenarios given above will be equal at long mixing times, in the absence of relaxation, if a short mixing time is chosen then the transfer efficiencies can be different, with a minimum efficiency when irradiating in the middle of two resonances that have a chemical shift difference.

IV.3.2.c Comparison and interpretation of analytical and numerical results

In this section, it is investigated whether the sole first-order Hamiltonian terms are sufficient to describe the spin dynamics during $BR2_2^1$ recoupling. For that purpose, the evolution of the density matrix during such a sequence was calculated using MATLAB software by considering only the first-order Hamiltonian of the dipolar coupling in the "offset frame" (see Eqn. IV.20) or that of the dipolar coupling and offset of $R2_2^1$ and $R2_2^{-1}$ in the "rf frame" (see Eqns. IV.13, IV.14a and IV.14b). These evolutions calculated from the first-order Hamiltonian were compared to those simulated using SPINEV software, which considers the full spin Hamiltonian.

Since the profile for $BR2_2^1$ depends on both the offset and the difference in isotropic chemical shifts between the coupled nuclei, four cases were considered.

(i) $\Omega_{I_1} = \Omega_{I_2} = \nu_{offset}$
(ii) $\Omega_{I_1} = -\Omega_{I_2} = \nu_{offset}$ (IV.25)
(iii) Ω_{I_1} = -2.5 kHz - ν_{offset} and Ω_{I_2} = 2.5 kHz - ν_{offset}
(iv) Ω_{I_1} = -10 kHz - ν_{offset} and Ω_{I_2} = 10 kHz - ν_{offset}

In case (i) the isotropic chemical shifts of the two nuclei are equal, corresponding to an auto-correlation diagonal peak in a DQ-SQ 2D spectrum. For (ii), the isotropic chemical shifts of the two nuclei are set opposite to each other, corresponding to off-diagonal cross peaks in a DQ-SQ 2D spectrum. For (iii) and (iv), the difference in isotropic chemical shifts is equal to 5 and 20 kHz, respectively, and these also correspond to off-diagonal cross peaks in a DQ-SQ 2D spectrum. For each case, the build-up curve, i.e. the transfer efficiency as function of the recoupling time, was simulated at different ν_{offset} (not shown) to obtain the optimum mixing time. Then this value was used to investigate the robustness to offset by varying ν_{offset} from – 15 kHz to + 15 kHz.

Single crystal

Initially the simulations were performed for a single crystal with the Euler angles given in Section IV.3.2. The offset profiles, i.e. the transfer efficiency versus ν_{offset} frequency, are shown in Figure IV.4.

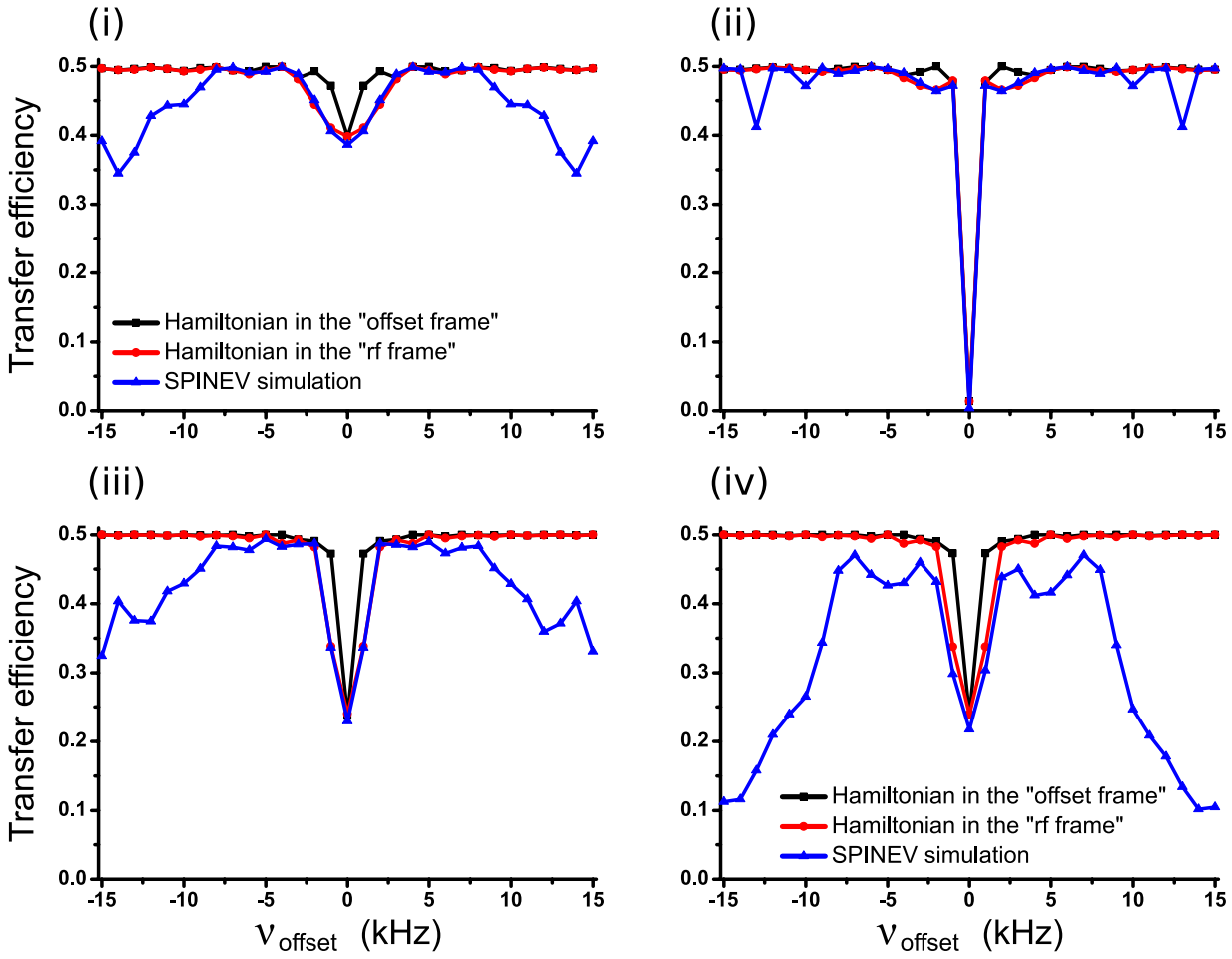

Figure IV.4. Comparison of the dependence of the transfer efficiency using $BR2_2^1$ recoupling on ν_{offset} for a single crystal containing an isolated ^{13}C spin pair. The subfigures (i) to (iv) correspond to the resonance conditions given in Eqn. IV.25. The transfer efficiency was simulated using the first-order Hamiltonian in the "offset frame" and in the "rf frame" as well as using the full Hamiltonian through SPINEV software.

As seen in Figure IV.4ii, for case (ii), where the isotropic chemical shifts are opposite and the rf irradiation is applied in the middle of the two peaks, there is a good agreement between SPINEV simulations and those obtained using the first-order Hamiltonian. The result demonstrates that the effective Hamiltonian can be restricted to its first-order terms in this case. For cases (i) and (iii), the SPINEV simulations agree with those obtained from the first-order average Hamiltonian in the "rf frame" but are in poor agreement with those derived from its expression in the "offset frame" since the offset approximation is no longer valid when the offset values of nuclei are as large as the dipolar couplings. Hence, for these cases, the first-order average Hamiltonian in the "rf frame" is still sufficient to describe the spin dynamics. It is also noticed that for large ν_{offset} frequency, the simulated efficiency decreases for SPINEV simulations while it remains constant according to the first-order Hamiltonian approximations. Such discrepancy indicates that the spin dynamics during $BR2_2^1$ recoupling is affected by higher-order terms of the average Hamiltonian involving offset for large ν_{offset} frequency. According to Figure IV.4ii, these terms do not influence the dynamics when the rf irradiation is applied in the middle of the resonance frequencies of the two ^{13}C nuclei. Finally, for the case (iv), there is a poorer agreement between SPINEV simulations and those derived from the first-order average Hamiltonian. In such a case, the difference in resonance frequencies between the correlated nuclei is 20 kHz. Hence, even at ν_{offset} = 0 kHz, higher-order terms of the average Hamiltonian influence the spin dynamics. In conclusion, the first-order average Hamiltonian terms could describe the spin dynamics resulting from $BR2_2^1$, except for the cases of large ν_{offset} and large difference in isotropic chemical shifts. The next step is to check the validity of the previous claim in the case of a powder.

Powder

The simulations were also carried out for a powder using the parameters given in Section IV.3.2.

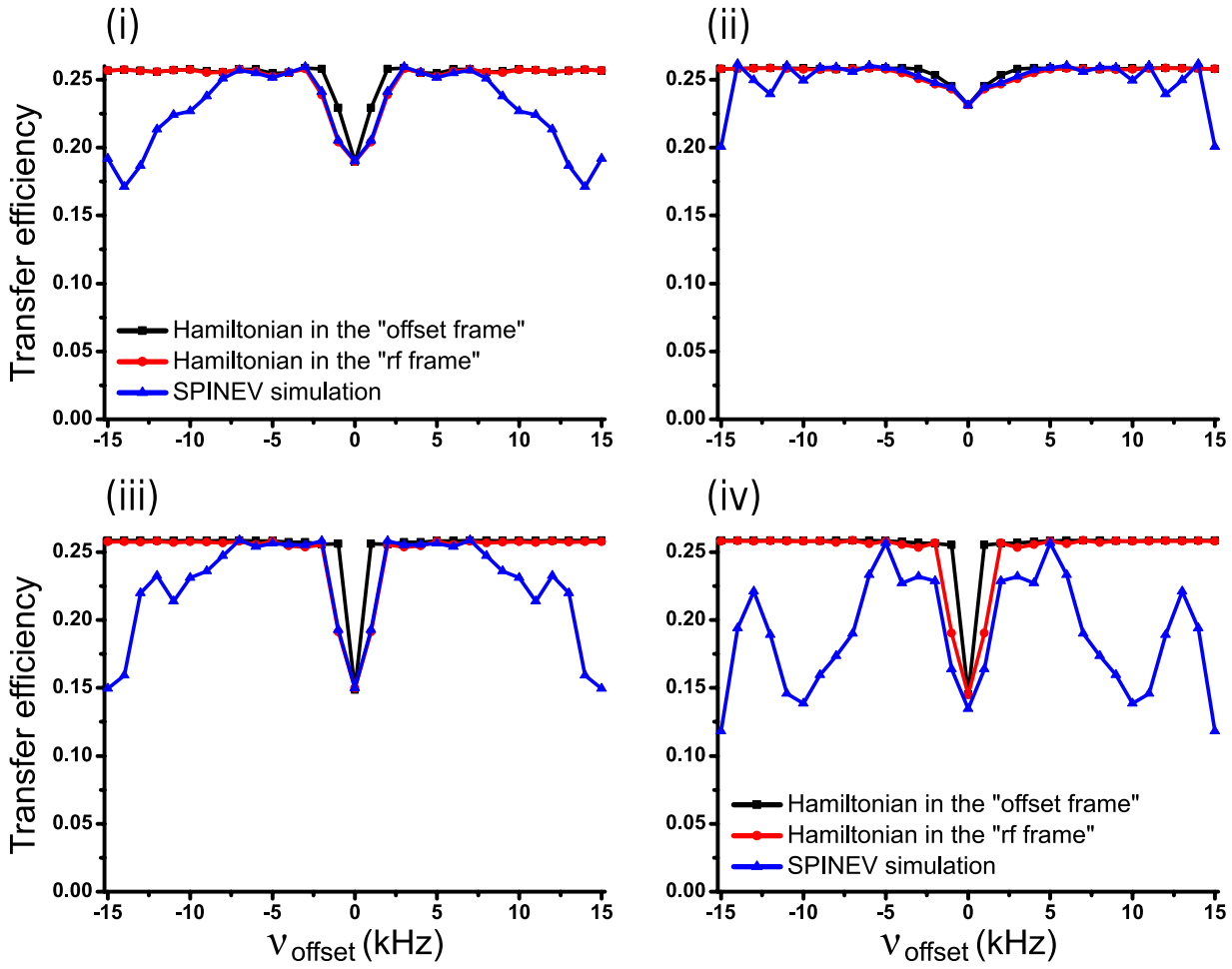

Figure IV.5. Comparison of the dependence of the transfer efficiency using $BR2_2^1$ recoupling on ν_{offset} for a powder. Each crystallite contains an isolated ^{13}C spin pair. The subfigures (i) to (iv) correspond to the conditions given in Eqn. IV.25. The transfer efficiency was simulated using the first-order Hamiltonian in the "offset frame" and in the "rf frame" as well as using the full Hamiltonian through SPINEV software.

The comparison of Figure IV.4 and Figure IV.5 shows that there is no significant difference between the single crystal and powder models.

IV.3.2.d Simulations for quadrupolar nuclei

Simulations were also used to compare the efficiency and the robustness to offset of different recoupling schemes for quadrupolar nuclei.

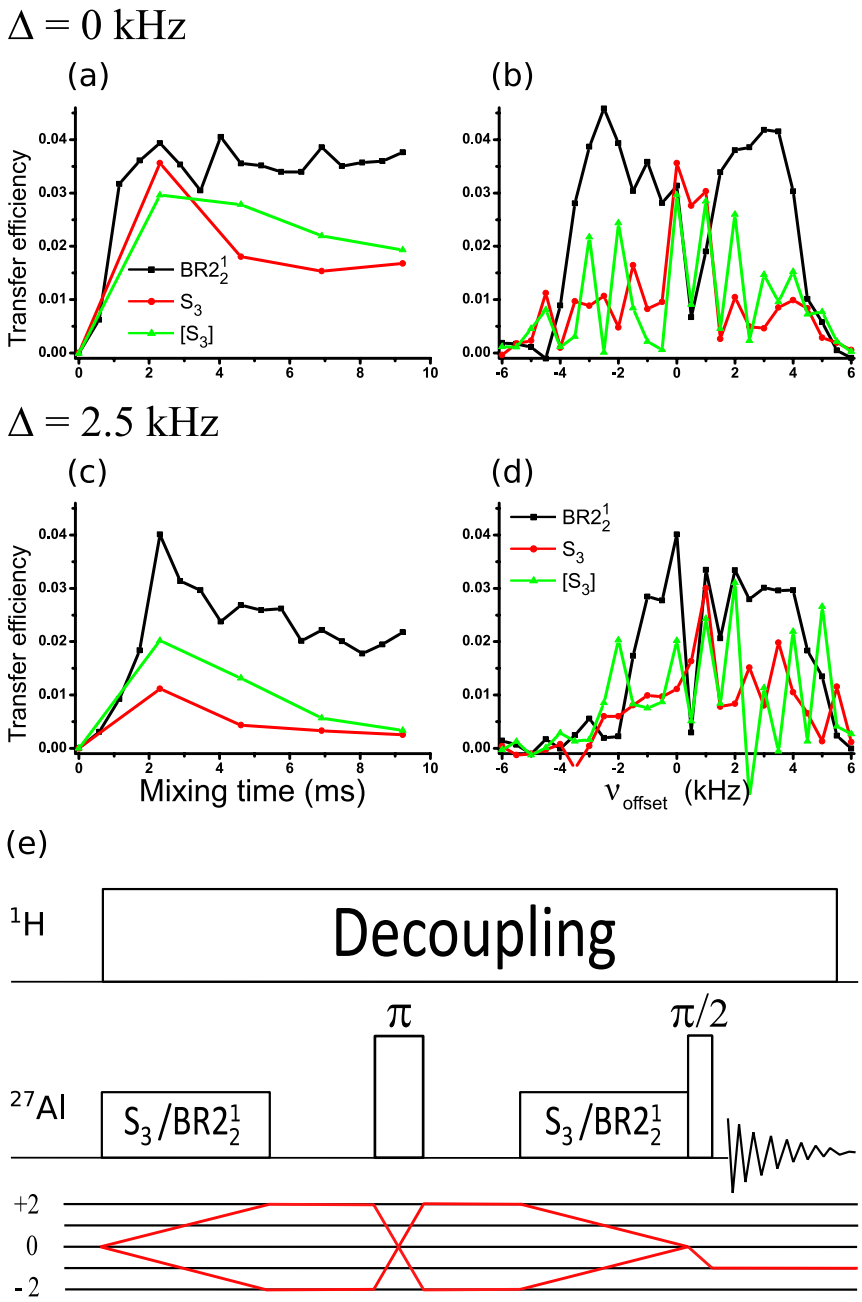

Figure IV.6. Simulated ^{27}Al homonuclear transfer build-ups (a,c) and offset profiles (b,d) for a powder. Each crystallite contains an isolated ^{27}Al spin pair. The difference in isotropic resonance

frequencies between the spins is equal to Δ= 0 kHz for (a,b) and 2.5 kHz for (c,d). A typical ^{27}Al homonuclear correlation sequence is displayed in subfigure e.$BR2_2^1$, S_3 and [S_3] homonuclear dipolar recoupling schemes were employed. The optimum mixing time for all recoupling sequences is 2.3 ms. For (a) ν_{offset} = -2 kHz for $BR2_2^1$, and ν_{offset} = 0 kHz for S_3 and [S_3]. For (c) ν_{offset} = 0 kHz for $BR2_2^1$, S_3, and [S_3]. The offset profiles were simulated by varying ν_{offset} from -6 to + 6 kHz, the mixing time being set to 2.3 ms.

Simulations were performed for a powder of isolated pairs of ^{27}Al nuclei. At the employed conditions, the quadrupolar induced shift was -0.53 kHz. For ^{27}Al nuclei with identical resonance frequencies (Δ = 0 kHz), it is shown that all the recoupling sequences give a similar optimum build-up of 2.3 ms. However, the maximum transfer efficiency is slightly higher (4 %) for $BR2_2^1$ (at ν_{offset} = -2 kHz) than for the other recoupling sequences (3 % for [S_3] (at ν_{offset} = 0 kHz)). The difference in transfer efficiencies among $BR2_2^1$, [S_3], and S_3 recoupling schemes must stem from the presence of isotropic chemical shift terms in the first-order average Hamiltonian for $BR2_2^1$ recoupling. This claim is further confirmed by the offset profile. It is first observed that $BR2_2^1$ is the most robust sequence to offset, being efficient between – 4 to + 4 kHz despite the low amplitude of rf field, about 2.5 kHz (one-sixth of $\omega_R/(2\pi)$). Furthermore, the offset profile of $BR2_2^1$ exhibits a “trough” centered at ν_{offset} = 0.5 kHz, i.e. the resonance frequency of the ^{27}Al signals (since the quadrupolar induced shift is ~ -0.5 kHz). Conversely, S_3 and [S_3] are only efficient over the offset range from -0.5 kHz to 1.5 kHz, which corresponds to an excitation bandwidth of 2.5 kHz. For the S_3 and [S_3] sequences, the offset does not contribute to the polarization transfer from I_{1z} to I_{2z}. Paradoxically, the presence of offset terms in the first-order Hamiltonian of $BR2_2^1$ recoupling broadens the excitation bandwidth.

The simulations were performed not only for auto-correlation peaks (Δ = 0) but also for off-diagonal cross peaks (Δ = 2.5 kHz). The difference in chemical shift between the two nuclei is chosen since it is similar to the rf amplitude. Although the optimum mixing time is still at 2.3 ms, the transfer efficiency for different recoupling sequences differs significantly. As shown in Figure IV.6c, where all build-up curves were simulated at ν_{offset} = 0 kHz, for $BR2_2^1$ the maximum transfer efficiency remains at 4% while the efficiency for S_3 and $[S_3]$ drops to 1% and 2%, respectively. In Figure IV.6d, $BR2_2^1$ is still the most robust sequence with respect to offset but the offset profile is shifted to the right, compared to Figure IV.6b. This could be explained owing to the change of the chemical shift center between the two nuclei, which is around 1.2 kHz while this value is 0 kHz for auto-correlation peaks. For S_3 recoupling, the highest transfer efficiency is achieved at ν_{offset} ~ 1 kHz as expected since this frequency is in the middle of the two chemical shifts. For $[S_3]$, the spin dynamics is complex and still under investigation for the explanation of the large oscillations.

In short, for different chemical shift regimes and at $\omega_R/(2\pi)$ = 13.889 kHz, $BR2_2^1$ is the most favorable choice since it provides the highest transfer efficiency and is the most robust to offset. Simulations will be confirmed by experiments below.

IV.4 Experimental results

Experiments were performed on m-alumina[57] using the sequence given in Figure IV.6e to verify the simulated results. The experimental conditions were $\omega_R/(2\pi)$ ~14 kHz, the length of CT-selective $\pi/2$- and π- pulses were 8 and 46 μs, respectively, using ν_{rf} = 10.4 kHz. For the proposed model system used in the simulations, the dipolar coupling interaction between two ^{27}Al nuclei is large enough for both S_3 and $[S_3]$ to reach the optimum mixing time after one loop. However, for the real experiment, the dipolar coupling interactions could be smaller owing to the

longer internuclear distances and/or interference from other interactions. Hence, [S_3] is a more favorable choice than S_3 since the transfer should build up faster, hence reducing possible losses due to DQ coherence decay during the excitation and reconversion blocks. The results are illustrated in Figure IV.7.

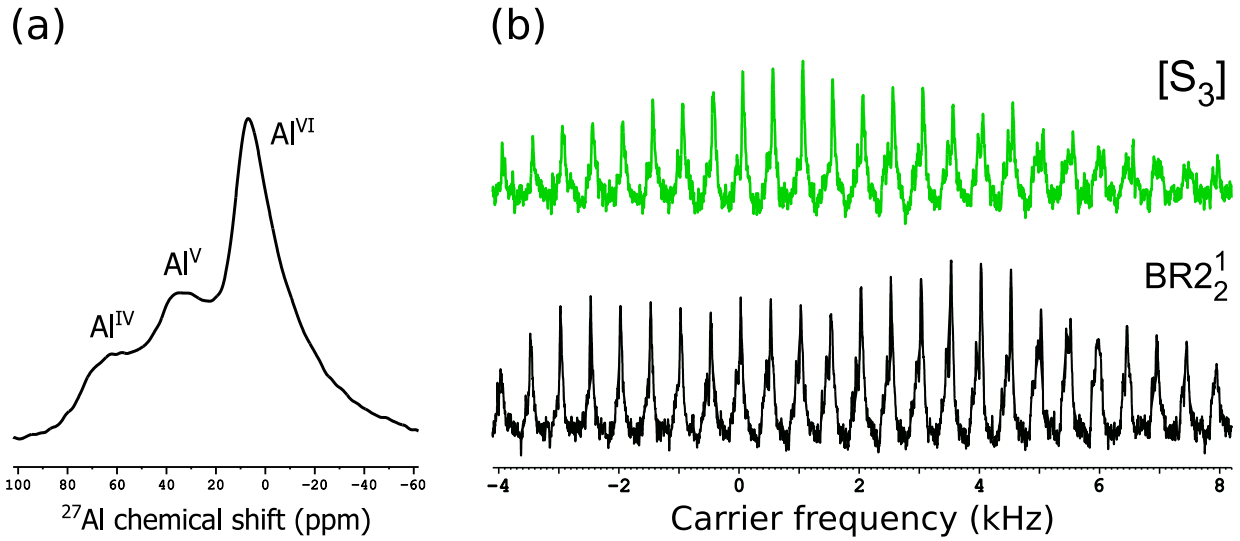

Figure IV.7. (a) The conventional 1D ^{27}Al spectrum of m-alumina at room temperature. (b) The offset profile of ^{27}Al homonuclear polarization transfer using $BR2_2^1$ (bottom) and [S_3] (top) recoupling. The pulse sequence used to record the experiments in (b) is displayed in Figure IV.6c. Experiments were performed at B_0 = 9.4 T and $\omega_R/(2\pi)$ = 13.889 kHz.

The 1D ^{27}Al spectrum of m-alumina is shown in Figure IV.7a. This spectrum was acquired after a CT-selective π/2 pulse. The spectrum features three peaks (see Section III.7 for more details) and the ^{27}Al chemical shift ranges from +80 to –20 ppm (+8 to -2 kHz).

To test the robustness of the two recoupling sequences, the carrier frequency was varied from +8 to –4 kHz, ensuring to cover the whole spectrum. The experimental offset profiles of $BR2_2^1$ and [S_3] are presented in Figure IV.7b. It is clearly confirmed that $BR2_2^1$ is better than [S_3]

regarding the robustness to offsets and transfer efficiency, in agreement with the simulations of Figure IV.6.

The experimental offset profiles of Figure IV.7b agree well with those of Figure IV.6. The experimental offset profile of [S_3] exhibits a maximum for on-resonance irradiation, while $BR2_2^1$ features a "trough" on-resonance.

Although simulations and experiments present numerous similarities, it can be noticed that there are some differences between them. These discrepancies could arise from:

(i) C_Q = 3 MHz was used for simulations but in real experiments, a distribution of C_Qs are present in m-alumina;

(ii) Not only the auto-correlation peaks but also the cross peaks contribute to the signal intensities in the 1D offset profile;

(iii) The excitation efficiency by rf pulses differs between sites subjected to different quadrupolar interactions.

In summary, experiments performed at $\omega_R/(2\pi)$ = 13.889 kHz showed that for studies of the spatial proximities between ^{27}Al nuclei, $BR2_2^1$ is the most favorable choice of recoupling sequence.

IV.5 Conclusion

In this chapter, the spin dynamics of $BR2_2^1$ for spin-1/2 nuclei was analyzed using AHT. The analytical expression of the first-order average Hamiltonian terms were verified by simulations, and these terms allow the profile of the robustness to offset of $BR2_2^1$ recoupling for spin-1/2 nuclei to be explained. Further treatment showed that $BR2_2^1$ is mainly governed by first-order Hamiltonian terms. For quadrupolar nuclei, simulations were performed and showed that $BR2_2^1$ is the most favorable choice for probing ^{27}Al-^{27}Al spatial proximities, which was verified

by experiments carried out on m-alumina. For the next step, experiments at higher $\omega_R/(2\pi)$ are to be implemented since the higher the MAS rate, the higher the rf amplitude, allowing the excitation of a larger bandwidth. Also, further analysis on the spin dynamics of $BR2_2^1$ for quadrupolar nuclei is required.

Chapter V CONCLUSIONS AND PERSPECTIVES

V.1. Conclusions

This PhD work focused on the use of MAS-DNP to investigate the structures of two classes of inorganic and hybrid nanostructured materials: (i) silica NPs functionalized with siloxane chains and (ii) γ- and m-alumina.

Siloxanes grafted onto silica NPs can be used as sacrificial molecules, aiming at protecting proton exchange membranes from degradation species formed during the operation of a fuel cell. Thus, these NPs are promising systems to lengthen the working lifetime of fuel cells. Owing to the substantial enhancement in NMR sensitivity gained through MAS-DNP, 2D ^{29}Si homonuclear correlation experiments could be acquired so that the condensation network of the siloxanes on the surface of the silica NPs could be elucidated. These DNP-enhanced NMR 2D spectra showed that the functionalizing groups are grafted via the favored lateral condensation; but ideal monolayer coverage was not achieved. Further structural information, namely the ^{29}Si-^{29}Si internuclear distance and the *J*-coupling, were also extracted as a result of the sensitivity achieved through MAS-DNP. These parameters can be used as restraints for structural models of the functionalized silica NPs. A better understanding of the structures of these nanocomposites will facilitate the rational improvement of their properties and hence the lifetime of fuel cells. Such a hyperpolarization technique is not only useful for functionalized silica NPs, but opens new avenues for the characterization of complex silica-containing materials.

γ- and m-alumina are important owing to their wide range of applications in industry, playing the role of a catalyst, a catalyst support, and an adsorbent. ^{27}Al NMR can provide precious insights into the structure of these materials. However, ^{27}Al nuclei at the surface are subject to large quadrupolar interactions, which reduces the sensitivity, notably for experiments

involving coherence transfer. MAS-DNP was employed to enhance the NMR sensitivity. It was shown that for such systems, a careful optimization of the sample preparation was required. Hydrophobic and hydrophilic sample preparations were performed to investigate the effects of different experimental conditions on the distributions of polarization agents and NMR relaxation parameters, which have a direct influence on the sensitivity. It was found that the bTbK polarizing agent in the organic solvent TBE is on average closer to the surface of alumina than TOTAPOL in an aqueous solvent. This observed surface affinity is likely one of the reasons explaining the highest sensitivity achieved with the use of 5 mM bTbK in TBE for MAS-DNP. Owing to the optimized sensitivity, the low efficiency of the $^{1}H \rightarrow ^{27}Al$ CP experiment was circumvented, allowing the observation of the surface of the alumina materials. Simulations were carried out to study the transfer of polarization depth of CP and it was demonstrated that this CP technique only affects the first layer of the surface of the material. The surface of m- and γ-alumina were characterized and it was found that Al^{V} sites are clearly observed in the case of m-alumina but not γ-alumina. The existence of these sites in the first layer of γ-alumina was examined by a *primostrato* MQMAS experiment using $^{1}H \rightarrow ^{27}Al$ CP. This experiment demonstrated that the first atomic layer contains Al^{V} sites. Whether the bulk of γ-alumina also contains Al^{V} sites like that of m-alumina was studied by a combination of MQMAS and a new *bulk-filtered* technique. The absence of Al^{V} sites in the resulting spectrum led to the conclusion that Al^{V} sites only reside in the first layer, not in the bulk for γ-alumina.

Further information on the locations and spatial proximities of these Al^{V} sites was explored by the use of the HORROR-based recoupling sequence, $BR2_2^1$. It was shown that Al^{V} sites neighbor to Al^{VI} sites. There is no significant evidence for Al^{V}-Al^{V} and Al^{IV}-Al^{V} proximities, which could be explained either by their long distances from each other or just that

the intensities of correlations are under the detectable limit. Additional investigations require improvements in B_0, $\omega_R/(2\pi)$, polarizing agents, and/or recoupling sequences.

To improve on the recoupling sequences, the spin dynamics of the current sequence ($BR2_2^1$) was analyzed, firstly for spin-1/2 nuclei. Numerical simulations were performed to verify the analytical approach. The derived Hamiltonian terms allow the explanation of many major features of the response of $BR2_2^1$ to a change of rf offset. The next step was to move to the case of quadrupolar nuclei. Through numerical simulations, $BR2_2^1$ was compared to other HORROR-based recoupling sequences, namely S_3 and $[S_3]$, and it was shown that $BR2_2^1$ is superior in terms of transfer efficiency and robustness to offsets. These results were also confirmed by experiments performed on m-alumina.

In summary, MAS-DNP has been shown to be both feasible and effective in providing new insights into the structures of complex materials containing low natural abundance ^{29}Si nuclei or quadrupolar ^{27}Al nuclei. The experiments used to obtain these insights were ascribed to be impracticable by conventional ssNMR. This hyperpolarization technique could potentially become a powerful routine characterization tool for material science.

V.2. Perspectives

There are many prospects resulting from the present study. For the structural characterization of the aluminas, only qualitative information was achieved. Additional steps will involve a quantitative analysis; for instance, the relative ratio for different Al sites on the surface and in the bulk. In order to do this, accurate C_Q determination is required since the response of different ^{27}Al sites to rf irradiation depends on this parameter. Furthermore, in spite of the successful results obtained at 9.4 T, the detection of sites subject to high C_Q is still difficult owing to the detrimental broadening effects of the second-order quadrupolar interaction. Since this effect is

inversely proportional to B_0, efficiently implementing experiments at higher fields could reduce this broadening effect; hence leading to more precise data.

In the current work, the aluminas were used as received and the surfaces of these materials are covered by physisorbed and chemisorbed water layers. However, some industrial applications utilize high temperatures where hydroxyl groups are removed and the materials become "activated". Whether MAS-DNP could be applicable for the study these activated materials is a future direction for this research.

The work on pulse sequence methodology is also a fascinating future research axis. As the spin dynamics of $BR2_2^1$ were well explored for spin-1/2 nuclei, the next step is to successfully derive a complete theory for the case of quadrupolar nuclei. From the thorough understanding of the spin dynamics, the potential development of a new family of recoupling sequences is foreseen, which will work well for nuclei experiencing large anisotropic interactions, such as quadrupolar nuclei.

REFERENCES

1. Ramamoorthy, A. *NMR spectroscopy of Biological Solids*. (CRC Press, 2005).
2. Kiihne, S. R. & de Groot, H. J. M. *Perspectives on Solid State NMR in Biology*. **1,** (Springer Netherlands, 2001).
3. Chan, J. C. C. Solid-state NMR techniques for the structural determination of amyloid fibrils. *Topics in Current Chemistry* **306,** 47–88 (2012).
4. Müller, H., Etzkorn, M., & Heise, H. Solid-State NMR Spectroscopy of Proteins. *Topics in Current Chemistry*. **335**, 121–156 (2013).
5. Separovic, F., Naito, A. *Advances in Biological Solid-State NMR*. (Royal Society of Chemistry, 2014).
6. Fitzgerald, J. J., & Depaul, S. M. Solid-State NMR Spectroscopy of Inorganic Materials. *ACS Symp.* **717,** 1–132 (1999).
7. Bakhmutov, V. I. Strategies for solid-state NMR studies of materials: From diamagnetic to paramagnetic porous solids. *Chem. Rev.* **111,** 530–562 (2011).
8. Edén, M. NMR studies of oxide-based glasses. *Annu. Reports Sect. 'C' (Physical Chem.* **108,** 177–221 (2012).
9. Massiot, D., Messinger, R. J., Cadars, S., Deschamps, M., Montouillout, V., Pellerin, N., Veron, E., Allix, M., Florian, P., & Fayon, F. Topological, geometric, and chemical order in materials: Insights from solid-state NMR. *Acc. Chem. Res.* **46,** 1975–1984 (2013).
10. Ashbrook, S. E., Dawson, D. M., & Seymour, V. R. Recent developments in solid-state NMR spectroscopy of crystalline microporous materials. *Phys. Chem. Chem. Phys. Phys. Chem. Chem. Phys* **16,** 8223–8242 (2014).
11. Wenckebach, W. T. The solid effect. *Appl. Magn. Reson.* **34,** 227–235 (2008).
12. Andrew, E. R. R., Bradbury, A., & Eades, R. G. G. Nuclear Magnetic Resonance Spectra from a Crystal rotated at High Speed. *Nature* **182,** 1659–1659 (1958).
13. Hartmann, S. R., & Hahn, E. L. Nuclear Double Resonance in the Rotating Frame. *Phys. Rev.* **128,** 2042–2053 (1962).
14. Bloom, A. L., & Shoolery, J. N. Effects of Perturbing Radiofrequency Fields on Nuclear Spin Coupling. *Phys. Rev.* **97,** 1261–1265 (1955).
15. Ye, Y. Q., Malon, M., Martineau, C., Taulelle, F., & Nishiyama, Y. Rapid measurement of multidimensional 1H solid-state NMR spectra at ultra-fast MAS frequencies. *J. Magn. Reson.* **239,** 75–80 (2014).
16. Carver, T. R., & Slichter, C. P. Polarization of Nuclear Spins in Metals. *Phys. Rev.* **92,** 212–213 (1953).
17. Ward, H. R., & Lawler, R. G. Nuclear Magnetic Resonance Emission and Enhanced Absorption in Rapid Organometallic Reactions. *J. Am. Chem. Soc.* **89,** 5518–5519 (1967).
18. Kaptein, R. Introduction to Chemically Induced Magnetic Polarization. *Chemically Induced Magnetic Polarization* **34,** 1–16 (Springer Netherlands, 1977).
19. Bowers, C. R., & Weitekamp, D. P. Transformation of Symmetrization Order to Nuclear-Spin Magnetization by Chemical Reaction and Nuclear Magnetic Resonance. *Phys. Rev. Lett.* **57,** 2645–2648 (1986).
20. Natterer, J., & Bargon, J. Parahydrogen induced polarization. *Prog. Nucl. Magn. Reson. Spectrosc.* **31,** 293–315 (1997).

21. Appelt, S., Baranga, A. B.-A., Erickson, C. J., Romalis, M. V., Young, A. R., & Happer, W. Theory of spin-exchange optical pumping of ^{3}He and ^{129}Xe. *Phys. Rev. A* **58,** 1412–1439 (1998).
22. Overhauser, A. W. Polarization of nuclei in metals. *Phys. Rev.* **92,** 411–415 (1953).
23. Carver, T. R., & Slichter, C. P. Experimental Verification of the Overhauser Nuclear Polarization Effect. *Phys. Rev.* **102,** 975–980 (1956).
24. Leifson, O., & Jeffries, C. D. Dynamic Polarization of Nuclei by Electron-Nuclear Dipolar Coupling in Crystals. *Phys. Rev.* **122,** 1781–1795 (1961).
25. Schmugge, T. J., & Jeffries, C. D. High Dynamic Polarization of Protons. *Phys. Rev.* **138,** A1785–A1801 (1965).
26. Wind, R. A., Duijvestijn, M. J., van der Lugt, C., Manenschijn, A., & Vriend, J. Applications of dynamic nuclear polarization in ^{13}C NMR in solids. *Prog. Nuc. Mag. Res. Sp.* **17,** 33–67 (1985).
27. Afeworki, M., & Schaefer, J. Mechanism of DNP-enhanced polarization transfer across the interface of polycarbonate/polystyrene heterogeneous blends. *Macromolecules* **25,** 4092–4096 (1992).
28. Becerra, L., Gerfen, G., Temkin, R. J., Singel, D., & Griffin, R. G. Dynamic nuclear polarization with a cyclotron resonance maser at 5 T. *Physical Review Letters* **71,** 3561–3564 (1993).
29. Gerfen, G. J., Becerra, L. R., Hall, D. a., Griffin, R. G., Temkin, R. J., & Singel, D. J. High frequency (140 GHz) dynamic nuclear polarization: Polarization transfer to a solute in frozen aqueous solution. *J. Chem. Phys.* **102,** 9494–9497 (1995).
30. Hall, D. a. Polarization-Enhanced NMR Spectroscopy of Biomolecules in Frozen Solution. *Science* **276,** 930–932 (1997).
31. Rosay, M., Lansing, J. C., Haddad, K. C., Bachovchin, W. W., Herzfeld, J., Temkin, R. J., & Griffin, R. G. High-frequency dynamic nuclear polarization in MAS spectra of membrane and soluble proteins. *J. Am. Chem. Soc.* **125,** 13626–13627 (2003).
32. Van der Wel, P. C. A., Hu, K.-N., Lewandowski, J., & Griffin, R. G. Dynamic Nuclear Polarization of Amyloidogenic Peptide Nanocrystals: GNNQQNY, a Core Segment of the Yeast Prion Protein Sup35p. *J. Am. Chem. Soc.* **128,** 10840–10846 (2006).
33. Bajaj, V. S., Hornstein, M. K., Kreischer, K. E., Sirigiri, J. R., Woskov, P. P., Mak-Jurkauskas, M. L., Herzfeld, J., Temkin, R. J., & Griffin, R. G. 250GHz CW gyrotron oscillator for dynamic nuclear polarization in biological solid state NMR. *J. Magn. Reson.* **189,** 251–279 (2007).
34. Can, T. V., Caporini, M. a., Mentink-Vigier, F., Corzilius, B., Walish, J. J., Rosay, M., Maas, W. E., Baldus, M., Vega, S., Swager, T. M., & Griffin, R. G. Overhauser effects in insulating solids. *J. Chem. Phys.* **141,** 064202-1–064202-8 (2014).
35. Barnes, a. B., De Paëpe, G., Van Der Wel, P. C. a, Hu, K. N., Joo, C. G., Bajaj, V. S., Mak-Jurkauskas, M. L., Sirigiri, J. R., Herzfeld, J., Temkin, R. J., & Griffin, R. G. High-field dynamic nuclear polarization for solid and solution biological NMR. *Appl. Magn. Reson.* **34,** 237–263 (2008).
36. Mentink-Vigier, F., Akbey, U., Hovav, Y., Vega, S., Oschkinat, H., & Feintuch, A. Fast passage dynamic nuclear polarization on rotating solids. *J. Magn. Reson.* **224,** 13–21 (2012).
37. Thurber, K. R., & Tycko, R. Theory for cross effect dynamic nuclear polarization under magic-angle spinning in solid state nuclear magnetic resonance: The importance of level crossings. *J. Chem. Phys.* **137,** 084508-1–084508-14 (2012).

38. Hu, K.-N., Yu, H., Swager, T. M., & Griffin, R. G. Dynamic nuclear polarization with biradicals. *J. Am. Chem. Soc.* **126,** 10844–10845 (2004).
39. Song, C., Hu, K. N., Joo, C. G., Swager, T. M., & Griffin, R. G. TOTAPOL: A biradical polarizing agent for dynamic nuclear polarization experiments in aqueous media. *J. Am. Chem. Soc.* **128,** 11385–11390 (2006).
40. Rosay, M., Tometich, L., Pawsey, S., & Bader, R. Solid-state dynamic nuclear polarization at 263 GHz: spectrometer design and experimental results. *Phys. Chem. Chem. Phys.* **12,** 5850–5860 (2010).
41. Matsuki, Y., Maly, T., Ouari, O., Karoui, H., Le Moigne, F., Rizzato, E., Lyubenova, S., Herzfeld, J., Prisner, T. F., Tordo, P., & Griffin, R. G. Dynamic nuclear polarization with a rigid biradical. *Angew. Chem. Int. Ed. Engl.* **48,** 4996–5000 (2009).
42. Salnikov, E., Rosay, M., Pawsey, S., Ouari, O., Tordo, P., & Bechinger, B. Solid-state NMR spectroscopy of oriented membrane polypeptides at 100 K with signal enhancement by dynamic nuclear polarization. *J. Am. Chem. Soc.* **132,** 5940–5941 (2010).
43. Sauvée, C., Rosay, M., Casano, G., Aussenac, F., Weber, R. T., Ouari, O., & Tordo, P. Highly efficient, water-soluble polarizing agents for dynamic nuclear polarization at high frequency. *Angew. Chem. Int. Ed. Engl.* **52,** 10858–10861 (2013).
44. Mance, D., Gast, P., Huber, M., Baldus, M., & Ivanov, K. L. The magnetic field dependence of cross-effect dynamic nuclear polarization under magic angle spinning. *J. Chem. Phys.* **142,** 234201-1–23420-10 (2015).
45. Lafon, O., Rosay, M., Aussenac, F., Lu, X., Trébosc, J., Cristini, O., Kinowski, C., Touati, N., Vezin, H., & Amoureux, J. P. Beyond the silica surface by direct silicon-29 dynamic nuclear polarization. *Angew. Chemie - Int. Ed.* **50,** 8367–8370 (2011).
46. Vitzthum, V., Miéville, P., Carnevale, D., Caporini, M. a., Gajan, D., Copéret, C., Lelli, M., Zagdoun, A., Rossini, A. J., Lesage, A., Emsley, L., & Bodenhausen, G. Dynamic nuclear polarization of quadrupolar nuclei using cross polarization from protons: surface-enhanced aluminium-27 NMR. *Chem. Commun.* **48,** 1988–1990 (2012).
47. Lee, D., Duong, N. T., Lafon, O., & De Paëpe, G. Primostrato Solid-State NMR Enhanced by Dynamic Nuclear Polarization: Pentacoordinated Al^{3+} Ions Are Only Located at the Surface of Hydrated γ-Alumina. *J. Phys. Chem. C* **118,** 25065–25076 (2014).
48. Lesage, A., Lelli, M., Gajan, D., Caporini, M. a., Vitzthum, V., Miéville, P., Alauzun, J., Roussey, A., Thieuleux, C., Mehdi, A., Bodenhausen, G., Copéret, C., & Emsley, L. Surface enhanced NMR spectroscopy by dynamic nuclear polarization. *J. Am. Chem. Soc.* **132,** 15459–15461 (2010).
49. Lelli, M., Gajan, D., Lesage, A., Caporini, M. A., Vitzthum, V., Miéville, P., Héroguel, F., Rascón, F., Roussey, A., Thieuleux, C., Boualleg, M., Veyre, L., Bodenhausen, G., Copéret, C., & Emsley, L. Fast characterization of functionalized silica materials by silicon-29 surface-enhanced NMR spectroscopy using dynamic nuclear polarization. *J. Am. Chem. Soc.* **133,** 2104–2107 (2011).
50. Lee, D., Takahashi, H., Thankamony, A. S. L., Dacquin, J.-P., Bardet, M., Lafon, O., & Paëpe, G. De. Enhanced solid-state NMR correlation spectroscopy of quadrupolar nuclei using dynamic nuclear polarization. *J. Am. Chem. Soc.* **134,** 18491–18494 (2012).
51. Takahashi, H., Lee, D., Dubois, L., Bardet, M., Hediger, S., & Depaëpe, G. Rapid natural-abundance 2D ^{13}C-^{13}C correlation spectroscopy using dynamic nuclear polarization enhanced solid-state NMR and matrix-free sample preparation. *Angew. Chemie - Int. Ed.* **51,** 11766–11769 (2012).

52. Takahashi, H., Hediger, S., & De Paëpe, G. Matrix-free dynamic nuclear polarization enables solid-state NMR ^{13}C-^{13}C correlation spectroscopy of proteins at natural isotopic abundance. *Chem. Commun.* **49,** 9479–9481 (2013).
53. Maly, T., Debelouchina, G. T., Bajaj, V. S., Hu, K.-N. N., Joo, C.-G. C.-G., Mak-Jurkauskas, M. L., Sirigiri, J. R., van der Wel, P. C. a, Herzfeld, J., Temkin, R. J., & Griffin, R. G. Dynamic nuclear polarization at high magnetic fields. *J. Chem. Phys.* **128,** 052211-1–052211-19 (2008).
54. Rossini, A. J., Zagdoun, A., Lelli, M., Lesage, A., Copéret, C., & Emsley, L. Dynamic nuclear polarization surface enhanced NMR spectroscopy. *Acc. Chem. Res.* **46,** 1942–1951 (2013).
55. Lee, D., Hediger, S., & De Paëpe, G. Is solid-state NMR enhanced by dynamic nuclear polarization? *Solid State Nucl. Magn. Reson.* **66,** 6–20 (2015).
56. Can, T. V., Ni, Q. Z., & Griffin, R. G. Mechanisms of dynamic nuclear polarization in insulating solids. *J. Magn. Reson.* **253,** 23–35 (2015).
57. Dacquin, J. P., Dhainaut, J., Duprez, D., Royer, S., Lee, A. F., & Wilson, K. An efficient route to highly organized, tunable macroporous-mesoporous alumina. *J. Am. Chem. Soc.* **131,** 12896–12897 (2009).
58. Wang, Q., Hu, B., Lafon, O., Trébosc, J., Deng, F., & Amoureux, J. P. Double-quantum homonuclear NMR correlation spectroscopy of quadrupolar nuclei subjected to magic-angle spinning and high magnetic field. *J. Magn. Reson.* **200,** 251–260 (2009).
59. Hohwy, M., Rienstra, C. M., Jaroniec, C. P., & Griffin, R. G. Fivefold symmetric homonuclear dipolar recoupling in rotating solids: Application to double quantum spectroscopy. *J. Chem. Phys.* **110,** 7983–7992 (1999).
60. Kim, H., Son, Y., Park, C., Lee, M.-J., Hong, M., Kim, J., Lee, M., Cho, J., & Choi, H. C. Germanium Silicon Alloy Anode Material Capable of Tunable Overpotential by Nanoscale Si Segregation. *Nano Lett.* **15,** 4135–4142 (2015).
61. Maciel, G. E. Silica Surfaces: Characterization. *Encyclopedia of Magnetic Resonance* (John Wiley & Sons, Ltd, 2007).
62. Wu, S.-H., Mou, C.-Y., & Lin, H.-P. Synthesis of mesoporous silica nanoparticles. *Chem. Soc. Rev* **42,** 3862–3875 (2013).
63. Lafon, O., Thankamony, A. S. L., Kobayashi, T., Carnevale, D., Vitzthum, V., Slowing, I. I., Kandel, K., Vezin, H., Amoureux, J.-P., Bodenhausen, G., & Pruski, M. Mesoporous Silica Nanoparticles Loaded with Surfactant: Low Temperature Magic Angle Spinning 13 C and 29 Si NMR Enhanced by Dynamic Nuclear Polarization. *J. Phys. Chem. C* **117,** 1375–1382 (2013).
64. Marsmann, H. C. Silica Surfaces: Characterization. *Encyclopedia of Magnetic Resonance* (John Wiley & Sons, Ltd, 2011).
65. Engelhardt, G. Silicon-29 NMR of Solid Silicates. *Encyclopedia of Magnetic Resonance* (John Wiley & Sons, Ltd, 2007).
66. Harris, R. K., Becker, E. D., Cabral De Menezes, S. M., Granger, P., Hoffman, R. E., & Zilm, K. W. Further conventions for NMR shielding and chemical shifts IUPAC recommendations 2008. *Solid State Nucl. Magn. Reson.* **33,** 41–56 (2008).
67. Maciel, G. E., & Sindorf, D. W. Silicon-29 NMR study of the surface of silica gel by cross polarization and magic-angle spinning. *J. Am. Chem. Soc.* **102,** 7606–7607 (1980).
68. Chuang, I.-S., & Maciel, G. A detailed model of local structure and silanol hydrogen bonding of silica gel surfaces. *J. Phys. Chem. B* **101,** 3052–3064 (1997).

69. Stephen Caravajal, G., Leyden, D. E., Quinting, G. R., & Maciel, G. E. Structural characterization of (3-aminopropyl)triethoxysilane-modified silicas by silicon-29 and carbon-13 nuclear magnetic resonance. *Anal. Chem.* **60,** 1776–1786 (1988).
70. Pinkas, J. Chemistry of silicates and aluminosilicates. *Ceramics - Silikaty* **49,** 287–298 (2005).
71. Angeli, F., Gaillard, M., Jollivet, P., & Charpentier, T. Influence of glass composition and alteration solution on leached silicate glass structure: A solid-state NMR investigation. *Geochim. Cosmochim. Acta* **70,** 2577–2590 (2006).
72. Mafra, L., Vidal-Moya, J. A., & Blasco, T. Structural Characterization of Zeolites by Advanced Solid State NMR Spectroscopic Methods. *Annual Reports on NMR Spectroscopy* **77,** 259–351 (2012).
73. Li, S., & Deng, F. Recent Advances of Solid-State NMR Studies on Zeolites. *Annual Reports on NMR Spectroscopy* **78,** 1–54 (2013).
74. Hartman, J. S., Narayanan, A., & Wang, Y. Spin-Lattice Relaxation in the 6H Polytype of Silicon Carbide. *J. Am. Chem. Soc.* **116,** 4019–4027 (1994).
75. Larsen, F. H., & Farnan, I. ^{29}Si and ^{17}O (Q)CPMG-MAS solid-state NMR experiments as an optimum approach for half-integer nuclei having long T1 relaxation times. *Chem. Phys. Lett.* **357,** 403–408 (2002).
76. Rossini, A. J., Zagdoun, A., Lelli, M., Gajan, D., Rascón, F., Rosay, M., Maas, W. E., Copéret, C., Lesage, A., & Emsley, L. One hundred fold overall sensitivity enhancements for Silicon-29 NMR spectroscopy of surfaces by dynamic nuclear polarization with CPMG acquisition. *Chem. Sci.* **3,** 108–115 (2012).
77. Kobayashi, T., Lafon, O., Thankamony, A. S. L., Slowing, I. I., Kandel, K., Carnevale, D., Vitzthum, V., Vezin, H., Amoureux, J.-P., Bodenhausen Ce, G., & Pruski, M. Analysis of sensitivity enhancement by dynamic nuclear polarization in solid-state NMR: a case study of functionalized mesoporous materials. *Phys. Chem. Chem. Phys. Phys. Chem. Chem. Phys* **15,** 5553–5562 (2013).
78. Bax, A., Freeman, R., & Kempsell, S. P. Natural abundance carbon-13-carbon-13 coupling observed via double-quantum coherence. *J. Am. Chem. Soc.* **102,** 4849–4851 (1980).
79. Nakai, T., & Mcdowell, C. A. One- and Two-Dimensional Refocused INADEQUATE NMR Experiments. *J. Magn. Reson. Ser. A* **104,** 146–153 (1993).
80. Lesage, A., Bardet, M., & Emsley, L. Through-bond carbon-carbon connectivities in disordered solids by NMR. *J. Am. Chem. Soc.* **121,** 10987–10993 (1999).
81. Sorensen, O. W., Eich, G. W., Levitt, M. H., Ernst, R., & Bodenhausen, G. Product Operator Formalism For the Description of NMR Pulse Experiments. *Prog. Nucl. Magn. Reson. Spectrosc.* **16,** 163–192 (1983).
82. Hohwy, M., Jakobsen, H. J., Hohwy, M., Jakobsen, H. J., Edén, M., Levitt, M. H., Levitt, M. H., Ede, M., Nielsen, N. C., Nielsen, N. C., & Introduction, I. Broadband dipolar recoupling in the nuclear magnetic resonance of rotating solids: A compensated C7 pulse sequence. *J. Chem. Phys.* **108,** 2686–2694 (1998).
83. Kristiansen, P. E., Carravetta, M., Van Beek, J. D., Lai, W. C., & Levitt, M. H. Theory and applications of supercycled symmetry-based recoupling sequences in solid-state nuclear magnetic resonance. *J. Chem. Phys.* **124,** 234510-1–234510-19 (2006).

84. Teymoori, G., Pahari, B., Stevensson, B., & Edén, M. Low-power broadband homonuclear dipolar recoupling without decoupling: Double-quantum ^{13}C NMR correlations at very fast magic-angle spinning. *Chem. Phys. Lett.* **547,** 103–109 (2012).
85. Peighambardoust, S. J., Rowshanzamir, S., & Amjadi, M. Review of the proton exchange membranes for fuel cell applications. *International Journal of Hydrogen Energy* **35,** 9349–9384 (2010).
86. Lee, D., Monin, G., Duong, N. T., Lopez, I. Z., Bardet, M., Mareau, V., Gonon, L., & De Paëpe, G. Untangling the Condensation Network of Organosiloxanes on Nanoparticles using 2D ^{29}Si– ^{29}Si Solid-State NMR Enhanced by Dynamic Nuclear Polarization. *J. Am. Chem. Soc.* **136,** 13781–13788 (2014).
87. Veshtort, M., & Griffin, R. G. SPINEVOLUTION: A powerful tool for the simulation of solid and liquid state NMR experiments. *J. Magn. Reson.* **178,** 248–282 (2006).
88. Zaremba, S. K. Good lattice points, discrepancy, and numerical integration. *Ann. di Mat. Pura ed Appl. Ser. 4* **73,** 293–317 (1966).
89. Levitt, M. H. Symmetry-Based Pulse Sequences in Magic-Angle Spinning Solid-State NMR. *eMagRes* **9,** 165–196 (2007).
90. Lee, M., & Goldburg, W. I. Nuclear-magnetic-resonance line narrowing by a rotating rf field. *Phys. Rev.* **140,** A1261–A1271 (1965).
91. Fung, B. M., Khitrin, a. K., & Ermolaev, K. An Improved Broadband Decoupling Sequence for Liquid Crystals and Solids. *J. Magn. Reson.* **142,** 97–101 (2000).
92. Foerster, H., Struppe, J., Steuernagel, S., Aussenac, F., Benevelli, F., Gierth, P., & Wegner, S. *Solid State NMR AVANCE Solids User Manual*. (Stanley J. Niles, 2009).
93. Davydov, V. Y., Kiselev, a. V., & Zhuravlev, L. T. Study of the surface and bulk hydroxyl groups of silica by infra-red spectra and D_2O-exchange. *Trans. Faraday Soc.* **60,** 2254 (1964).
94. Florian, P., Fayon, F., & Massiot, D. $^{2}J^{Si-O-Si}$ Scalar Spin−Spin Coupling in the Solid State: Crystalline and Glassy Wollastonite $CaSiO_3$. *J. Phys. Chem. C* **113,** 2562–2572 (2009).
95. Samain, L., Jaworski, A., Edén, M., Ladd, D. M., Seo, D. K., Javier Garcia-Garcia, F., & Häussermann, U. Structural analysis of highly porous γ-Al_2O_3. *J. Solid State Chem.* **217,** 1–8 (2014).
96. Yuan, Q., Yin, A.-X., Luo, C., Sun, L.-D., Zhang, Y.-W., Duan, W.-T., Liu, H.-C., & Yan, C.-H. Facile synthesis for ordered mesoporous gamma-aluminas with high thermal stability. *J. Am. Chem. Soc.* **130,** 3465–3472 (2008).
97. Alderman, D. W., Solum, M. S., & Grant, D. M. Methods for analyzing spectroscopic line shapes. NMR solid powder patterns. *J. Chem. Phys.* **84,** 3717–3725 (1986).
98. Morris, H. D., & Ellis, P. D. Aluminum-27 cross polarization of aluminas. The NMR spectroscopy of surface aluminum atoms. *J. Am. Chem. Soc.* **111,** 6045–6049 (1989).
99. Oas, T. G., Griffin, R. G., & Levitt, M. H. Rotary resonance recoupling of dipolar interactions in solid-state nuclear magnetic resonance spectroscopy. *J. Chem. Phys.* **89,** 692–695 (1988).
100. Frydman, L., & Harwood, J. S. Isotropic Spectra of Half-Integer Quadrupolar Spins from Bidimensional Magic-Angle Spinning NMR. *J. Am. Chem. Soc.* **117,** 5367–5368 (1995).
101. Amoureux, J.-P., Fernandez, C., & Steuernagel, S. ZFiltering in MQMAS NMR. *J. Magn. Reson. Ser. A* **123,** 116–118 (1996).
102. Ashbrook, S. E., Brown, S. P., & Wimperis, S. Multiple-quantum cross-polarization in MAS NMR of quadrupolar nuclei. *Chem. Phys. Lett.* **288,** 509–517 (1998).

103. Takahashi, H., Fernández-De-Alba, C., Lee, D., Maurel, V., Gambarelli, S., Bardet, M., Hediger, S., Barra, A. L., & De Paëpe, G. Optimization of an absolute sensitivity in a glassy matrix during DNP-enhanced multidimensional solid-state NMR experiments. *J. Magn. Reson.* **239,** 91–99 (2014).
104. Lee, D., Balmer, J. A., Schmid, A., Tonnar, J., Armes, S. P., & Titman, J. J. Solid-state nuclear magnetic resonance studies of vinyl polymer/silica colloidal nanocomposite particles. *Langmuir* **26,** 15592–15598 (2010).
105. Massiot, D., Fayon, F., Capron, M., King, I., Le Calve, S., Alonso, B., Durand, J.-O., Bujoli, B., Gan, Z., & Hoatson, G. Modelling one- and two-dimensional solid-state NMR spectra. *Magn. Reson. Chem.* **40,** 70–76 (2002).
106. d'Espinose de Lacaillerie, J.-B., Fretigny, C., & Massiot, D. MAS NMR spectra of quadrupolar nuclei in disordered solids: the Czjzek model. *J. Magn. Reson.* **192,** 244–251 (2008).
107. Nielsen, N. C., Bildsoe, H., Jakobsen, H. J., & Levitt, M. H. Double-quantum homonuclear rotary resonance: Efficient dipolar recovery in magic-angle spinning nuclear magnetic resonance. *J. Chem. Phys.* **101,** 1805–1812 (1994).
108. Mali, G., Fink, G., & Taulelle, F. Double-quantum homonuclear correlation magic angle sample spinning nuclear magnetic resonance spectroscopy of dipolar-coupled quadrupolar nuclei. *J. Chem. Phys.* **120,** 2835–2845 (2004).
109. Haeberlen, U., & Waugh, J. S. Coherent Averaging Effects in Magnetic Resonance. *Phys. Rev.* **175,** 453–467 (1968).
110. Magnus, W. On the Exponential Solution of Differential Equations for a Linear Operator. *Commun. Pure Appl. Math.* **7,** 649–673 (1954).

APPENDIX

A. The proof for the cyclic permutation of new derived DQ and ZQ terms as well as the evolution under chemical shifts

$$
\begin{aligned}
[\tfrac{I_{1x}+I_{2x}}{2}, DQ_y^{(x)}] &= \tfrac{1}{2}[I_{1x}+I_{2x}, 2I_{1y}I_{2y} - 2I_{1z}I_{2z}] = \tfrac{1}{2}([I_{1x}+I_{2x}, 2I_{1y}I_{2y}] - [I_{1x}+I_{2x}, 2I_{1z}I_{2z}]) \\
&= [I_{1x}, I_{1y}]I_{2y} + I_{1y}[I_{2x}, I_{2y}] - [I_{1x}, I_{1z}]I_{2z} - I_{1z}[I_{2x}, I_{2z}] \\
&= \mathrm{i}I_{1z}I_{2y} + \mathrm{i}I_{1y}I_{2z} + \mathrm{i}I_{1y}I_{2z} + \mathrm{i}I_{1z}I_{2y} \\
&= \mathrm{i}(2I_{1z}I_{2y} + 2I_{1y}I_{2z}) \\
&= \mathrm{i}DQ_z^{(x)} \qquad \text{(A.1)}
\end{aligned}
$$

$$
\begin{aligned}
[\tfrac{I_{1y}-I_{2y}}{2}, DQ_z^{(y)}] &= \tfrac{1}{2}[I_{1y}-I_{2y}, 2I_{1z}I_{2z} + 2I_{1x}I_{2x}] = \tfrac{1}{2}([I_{1y}-I_{2y},\ 2I_{1z}I_{2z}] + [I_{1y}-I_{2y},\ 2I_{1x}I_{2x}]) \\
&= [I_{1y}, I_{1z}]I_{2z} - I_{1z}[I_{2y}, I_{2z}] + [I_{1y}, I_{1x}]I_{2x} - I_{1x}[I_{2y}, I_{2x}] \\
&= \mathrm{i}I_{1x}I_{2z} - \mathrm{i}I_{1z}I_{2x} - \mathrm{i}I_{1z}I_{2x} + \mathrm{i}I_{1x}I_{2z} \\
&= \mathrm{i}(2I_{1x}I_{2z} - 2I_{1z}I_{2x}) \\
&= \mathrm{i}ZQ_x^{(y)} \qquad \text{(A.2)}
\end{aligned}
$$

$$
DQ_y^{(x)} \xrightarrow{\Omega_{I_1} I_{1x}} 2I_{1y}I_{2y}cos\Omega_{I_1}t + 2I_{1z}I_{2y}sin\Omega_{I_1}t - 2I_{1z}I_{2z}cos\Omega_{I_1}t + 2I_{1y}I_{2z}sin\Omega_{I_1}t
$$

$$
\begin{aligned}
2I_{1y}I_{2y}cos\Omega_{I_1}t &\xrightarrow{\Omega_{I_2} I_{2x}} 2I_{1y}I_{2y}cos\Omega_{I_1}t.cos\Omega_{I_2}t + 2I_{1y}I_{2z}cos\Omega_{I_1}t.sin\Omega_{I_2}t \\
2I_{1z}I_{2y}sin\Omega_{I_1}t &\xrightarrow{\Omega_{I_2} I_{2x}} 2I_{1z}I_{2y}sin\Omega_{I_1}t.cos\Omega_{I_2}t + 2I_{1z}I_{2z}sin\Omega_{I_1}t.sin\Omega_{I_2}t \\
-2I_{1z}I_{2z}cos\Omega_{I_1}t &\xrightarrow{\Omega_{I_2} I_{2x}} -2I_{1z}I_{2z}cos\Omega_{I_1}t.cos\Omega_{I_2}t + 2I_{1z}I_{2y}cos\Omega_{I_1}t.sin\Omega_{I_2}t \\
2I_{1y}I_{2z}sin\Omega_{I_1}t &\xrightarrow{\Omega_{I_2} I_{2x}} 2I_{1y}I_{2z}sin\Omega_{I_1}t.cos\Omega_{I_2}t - 2I_{1y}I_{2y}sin\Omega_{I_1}t.sin\Omega_{I_2}t
\end{aligned}
$$

$$
\begin{aligned}
&= 2I_{1y}I_{2y}cos(\Omega_{I_1} + \Omega_{I_2})t + 2I_{1y}I_{2z}sin(\Omega_{I_1} + \Omega_{I_2})t - 2I_{1z}I_{2z}cos(\Omega_{I_1} + \Omega_{I_2})t + 2I_{1z}I_{2y}sin(\Omega_{I_1} + \Omega_{I_2})t \\
&= (2I_{1y}I_{2y} - 2I_{1z}I_{2z})cos(\Omega_{I_1} + \Omega_{I_2})t + (2I_{1y}I_{2z} + 2I_{1z}I_{2y})\ sin(\Omega_{I_1} + \Omega_{I_2})t \\
&= DQ_y^{(x)}\ cos(\Omega_{I_1} + \Omega_{I_2})t + DQ_z^{(x)}\ sin(\Omega_{I_1} + \Omega_{I_2})t \qquad \text{(A.3)}
\end{aligned}
$$